NUMERICAL MODELLING OF RIVER PROCESSES: FLOW AND RIVER BED DEFORMATION

The research presented in this thesis was carried out at the group of Numerical Analysis and Computational Mechanics (NACM), University of Twente, PO Box 217, 7500 AE Enschede, The Netherlands and at the Water Resources and Engineering Department (Facultad de Ingeniería y Ciencias Hídricas), Universidad Nacional del Litoral, Santa Fe, Argentina.

The research was mainly supported by the European Union High Level Scholarship Programme for Latin America (Programme Alβan), the Institute of Mechanics, Processes and Control Twente (IMPACT), the Federal Agency for Promoting Science and Technology (ANPCyT, Argentina), and the National Scientific and Technical Research Council of Argentina (Consejo Nacional de Investigaciones Científicas y Técnicas, CONICET).

Cover: Landsat 5 TM satellite image of the Paraná alluvial system, Argentina.
Printed by PrintPartners Ipskamp, The Netherlands.

ISBN 978-90-365-2539-8

NUMERICAL MODELLING OF RIVER PROCESSES: FLOW AND RIVER BED DEFORMATION

DISSERTATION

to obtain
the doctor's degree at the University of Twente,
on the authority of the rector magnificus,
prof. dr. W.H.M. Zijm,
on account of the decision of the graduation committee,
to be publicly defended
on Thursday 13th September 2007 at 13:15

by

Pablo Tassi
born in Santa Fe, Argentina

Dit proefschrift is goedgekeurd door de promotor,
prof. dr. ir. J. J. W. van der Vegt

en de assistent-promotor,
dr. ir. O. Bokhove

Samenstelling promotiecommissie:

prof.dr.ir. A. J. Mouthaan	University of Twente, voorzitter/secretaris
prof.dr.ir. J. J. W. van der Vegt	University of Twente, promotor
dr.ir. O. Bokhove	University of Twente, assistent-promotor
prof.dr. C. A. Vionnet	Universidad Nacional del Litoral, Argentina
prof.dr.ir. S. J. M. H. Hulscher	University of Twente
prof.dr.ir. A. W. Heemink	Delft University of Technology
prof.dr.ir. J. A. M. Kuipers	University of Twente
prof.dr.ir. H. J. H. Clercx	Eindhoven University of Technology & University of Twente

A mi amada Antonella

Contents

Chapter 1

Introduction

1.1 Background to the research

The morphology of alluvial river channels[1] is a consequence of complex interaction between a number of constituent physical processes, such as flow, sediment transport and bed deformation [89]. The major driving forces governing the behavior of alluvial river channels are: sediment supply, flow regime (from upstream), channel topography, and the nature and volume of sediment being locally eroded and transported by the stream (from the bed and the riverbanks, and eventually deposited further downstream) [85]. It turns out that all alluvial river channels are subject from time to time to disturbances in their immediate environment caused by natural or artificial effects, namely variable inflow, sediment supply, and various human activities, such as reservoir construction, channel regulation, and water diversion [118].

Floods are primary impetuses for all alluvial river morphology. An increase in discharge may initiate bed surface movement and bank erosion, once the force exerted by the flood event (the impetus) has passed some threshold for movement or erosion. This threshold may require a specific flow magnitude and duration before producing a significant morphological response. The timing and frequency of the flood may also have profound effects on a population; a flood may cause damage to civil infrastructure located on or nearby the river [147]. For example, nearby the cities of Santa Fe and Paraná, Argentina, the Paraná river runs through a broad, very low-gradient alluvial valley, whose main channel is bounded by a steep, stable bank on the Paraná side, and by a 20 km wide floodplain on the Santa Fe side, see Figure 1.1. During the last century, and particularly in the past decades, floods of catastrophic magnitudes have severely hit the region, causing considerable damage. Recently, during the first quarter of 2003, large areas of the Central and Northern part of the state of Santa Fe itself, have been affected by an exceptional flood of the Salado River, as the result of extreme precipitation in the region [19]. The river overtopped its narrow and wandering channel and spread over the floodplain, destroying bridges and roads, and isolating some small towns in its run

---

[1] An *alluvial river channel* is one formed from its own sediment.

toward its outlet near Santa Fe city. In only one night, the failure of a 150m reach of a protecting levee resulted in the rapid flooding of lowland neighborhoods, which happened practically without warning. People in this area were used to dealing with floods causing water levels to rise steadily, but in this case, they faced a sudden increase of up to 2m in a few hours. In the chaos of the first 24 to 48 hours of the flood, an estimated 120,000 people were displaced. We reproduced numerically this catastrophic event in Chapter 3.

The wish to improve the safety situation and to foresee the impact of the ever growing human interference with the environment, has created a need for reliable predictions of complex situations found in nature. The socio-economical and political importance of alluvial systems has also increased this need. In recent years, the improved understanding of physical processes involved in the study of river hydraulics has led to the development of physical-mathematical formulations to explain the natural phenomena and to forecast changes due to, for example, human interference. There remain important knowledge gaps, however, which concern not only the complex nature of water and sediment movements, changes in bed configuration and their dynamic interactions, but also the utilization of reasonably accurate results by water managers, policy makers and engineers in real-life situations.

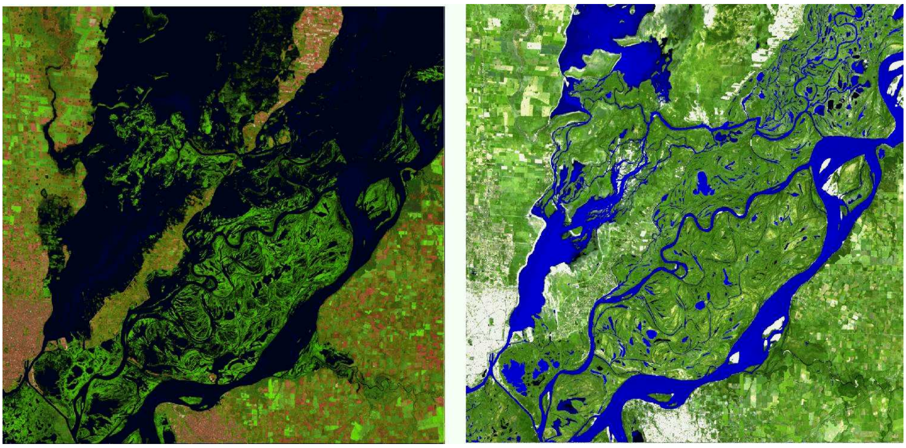

Figure 1.1: Landsat 5 TM satellite image of a sector of the Paraná alluvial system, Argentina. Left: high water level (19-01-98). Right: low water level (25-01-00). Source: http://www.conae.gov.ar/.

1.2 Research problem and modelling

In early time, research methodologies of river processes were primarily based on field observation and laboratory scale modelling. Laboratory scale models have been and are still essential for the understanding of complex river processes and as design and verification tools, despite their high cost of construction, maintenance and operation. Field measurements are also costly and difficult to realize especially for large–scale systems.

An alternative that has been growing in popularity and acceptance is river modelling. River modelling is the analysis and simulation of flow conditions based on the formulation and solution of mathematical relationships expressing hydraulic principles. Although the technique finds its origin in the 19th century work of Saint Venant and Boussinesq, the initial attempts of significance in application of mathematical models to the investigation of river processes can be found in the late 1940's [146, 69]. The branch of research, known as *river mechanics*, was intensified and broadened since the 1970's, whereafter river modelling has advanced from simplified models to complex ones with high levels of sophistication. Nowadays, with the rapid development of mathematical methodologies and the advances of computational facilities, the trend in the hydraulics community is to adopt Computational Fluid Dynamics (CFD) techniques developed by engineers and scientists to study a variety of river flow problems.

1.2.1 Morphological modelling

Prediction of morphological changes of the bed in a natural channel can be analysed by integrating in a mathematical model several modules, which are initially segregated in different physical mechanisms acting within the system according to their time response (i.e., it is a multi-scale problem). In summary, the relevant mechanisms that drives morphological changes of alluvial rivers are: (i) hydrodynamics, with conservation laws of mass and momentum; (ii) bed evolution, with a conservation law for sediment mass; and (iii) sediment transport, with predictors for the river sediment carrying capacity for sediment transport. Such a modelling system is often referred to as a *morphodynamic model* and is the one adopted in this thesis. Morphological models can be fully coupled [149], semi–coupled [3] and decoupled [34]. In a fully coupled model, sediment transport and flow occur simultaneously, and thus, their respective equations are coupled and should be solved simultaneously. Erosional dam–break flows, rapid morphological evolution processes due to hyper-concentrated sediment–laden floods, and debris flow are typical examples were the fully coupled approach must be employed [50]. In contrast, semi-coupled or decoupled models are applicable when the typical time scale for river bed adjustment is much longer than the typical time scale for water flow. The model presented in this thesis adapts the treatment of a semi-coupled approach, i.e., to alternate between the simulation of flow and bed evolution.

1.2.2 Model equations

The choice of appropriate model equations for flow and sediment transport will depend upon the scales of interest. The river bed is rarely flat, it is usually covered with both small– and large–scale sediment features. Depending on the sediment and the flow parameters, the flow–bottom interaction in channels with non-cohesive bottom gives rise to an extraordinary variety of forms, which may occur on a microscale (of the order of sediment size) leading to 'rippled' beds, or on a macroscale (of the order of flow depth) leading to the developments of 'bars'. These features are known as *bedforms* and a classification may be attempted based on the range of spatial and temporal scales typically observed in nature [53]. In turn, these modes of interaction not only represents different modes of sediment transport, but also different mechanisms of bed resistance. Sediments in transport customarily are classified on the basis of the mechanism by which they are moved: as *bedload*, where sediment particles are carried along the bed by sliding, rolling, and saltation and as *suspended load*, where sediment particles are carried in suspension by the flow. Additionally, *wash load* is defined as the transport of material finer than the bed material whose origin can be traced back to the river catchment. The dominance of one form of transport over the other depends on the flow intensity and the sediment characteristics. Sliding and rolling are prevalent in slower flows, while saltation and suspension dominate in faster flows.

At the scale of ripples, the mechanics of sediment transport could be coupled with the Reynolds–averaged Navier Stokes equations (NS) to describe the phenomenon. At large scales, however, the shallow water equations (SWE) are known to capture quite accurately the salient features –in an average sense– of open channel flows. The SWE are derived by simplifying the hydrodynamics in the vertical direction instead of using the full three–dimensional NS or Euler equations. As such, the SWE are obtained by assuming a hydrostatic pressure distribution and a uniform velocity profile across the water layer, resulting in a two–dimensional problem where the primary variables are the vertical averages of the horizontal fluid velocities and the fluid depth. This simplification enhances the speed of computations and facilitates further analytical approaches. In brief, the SWE are often used to model advection–dominated open channel flows, river and lake hydrodynamics, floodplain flows, estuarine and coastal circulation as well as long wave run-up and hydraulic bores, among other problems of interest within the engineering community [25].

In this thesis, the morphodynamic model emerges as a mixed hyperbolic–parabolic system of partial differential equations (PDE). It is based on the depth–average over the water column conservation laws of shallow water theory augmented by a flow resistance term, together with a depth–averaged conservation law expressing continuity of bed load sediment. A phenomenological sediment transport function relates the rate of bed load sediment transport to the local mean fluid velocity.

1.3 Numerical solution of the model equations

Over the past several decades, a variety of analytical and numerical methods were proposed to describe channel morphology and morphological adjustments for river engineering purposes [29]. There are particular difficulties associated with solving hyperbolic partial differential equations, including shock formation, rarefaction waves and contact discontinuities, which must be overcome by a good numerical scheme. Several numerical algorithms have been developed over the years to solve the system of conservation laws of water and sediment transport approximately, with finite difference, finite volume and finite element methods. For the numerical solution of the morphological model, we have chosen the discontinuous Galerkin method (DGFEM). These methods merged ideas from high-resolution finite difference and finite volume schemes for solving nonlinear hyperbolic systems within a finite element framework [11]. We refer the reader to [11, 10] and references therein for a historical overview of the method. In the DGFEM formulation, locally continuous basis and trial functions are introduced, which are globally discontinuous, within each element. Therefore, we are solving a system of PDEs by a numerical method in which the approximations to all state variables are discontinuous and double valued on each element interface. This property provides more flexibility in representing steep gradients and discontinuities. Monotone numerical fluxes are used to resolve the discontinuity, providing the means of communication between adjacent elements and specification of the boundary conditions. The numerical flux is obtained as a (exact or approximate) solution of a local one–dimensional Riemann problem.

The motivations for chosing DGFEM methods are that it is relatively easy [7]: (i) to improve the order of accuracy locally, thus allowing efficient p-adaptivity; (ii) to refine the grid locally, without taking into account the continuity restrictions typical of conforming finite element methods, thus allowing efficient h-adaptivity; and, (iii) to perform parallel computations [73], since the method is extremely local in data communication. Furthermore, its flexibility for using advanced time stepping schemes for multiscale problems; its ability to handle advection dominated flows including problems with hydraulic and sediment jumps or bores; its inherent mass and momentum conservation properties, which make them ideal for coupling flow and transport; and its stability and accuracy under highly varying flow regimes make it suitable for morphological problems [45, 108, 110].

1.4 Contributions of the thesis

It is only recently that DGFEM methods have been applied in the context of hydraulics applications [31, 32]. In this thesis, we extend and refine existing DGFEM methods applied to the solution of morphological models, e.g. [46]; and we developed an entirely new solver based upon the DGFEM method. In particular, (i) we use numerical fluxes in combination with a dissipation operator, applied only locally around discontinuities to limit spurious numerical oscillations; (ii) we derived and applied a kinetic numerical flux as an alternative to existing numerical fluxes; (iii) we study the generation of potential vorticity anomalies due to bore-vortex interactions in shallow water flows; (iv) we validated the numerical model against laboratory data of oblique hydraulic jumps for flow in a flume with a contraction; (v) we applied and refined the discontinuous Galerkin finite element discretization to systems with nonconservative products [126] to solve the hydrodynamic and bed evolution model; (vi) we implemented a numerical formulation to deal with the downhill rolling sediment term present in the sediment transport formula, as an alternative to the so-called local discontinuous Galerkin (LDG) framework [9], which employs a mixed formulation; (vii) we verified the results of our DGFEM model with a survey of original (semi–)analytical solutions; and, (viii) we validated these computed results against field data measurements of a trench excavated in the main channel of the Paraná river near Paraná, Argentina.

1.5 Outline of thesis content

An outline of thesis content is given as follows. Chapters 2 and 3 can be seen as an extension of Chapter 1, in which we motivated our research by studying the effects of flow resistance and eddy viscosity for vegetated floodplains and we numerically reconstructed the catastrophic flooding of Santa Fe city, Argentina, using the shallow water model. In Chapters 2 and 3, numerical difficulties associated with wave propagation and advection processes are solved by using the so-called grid enriched velocity solutions [67] and fractional step methods [72], respectively. Although these techniques have made progress towards solving the fully nonlinear form of the SWE, accuracy, robustness and artificial damping problem remains, especially when coupling flow and transport. These difficulties motivated the development and implementation of numerical schemes based on the discontinuous Galerkin formulation.

In Chapter 4, a second order space discontinuous Galerkin method is presented for the numerical solution of inviscid shallow water flows over varying bottom topography. We successfully validate the numerical model against exact solutions and laboratory measurements. Additionally, bore-vortex interactions were studied analytically and numerically to validate the model. In Chapter 5, the derivation, design, and implementation of a discontinuous Galerkin finite element method for the morphodynamic model is presented, based on an extended approach for systems of partial differential equations with non-conservative products, in combination with two intertwined Runge-Kutta time stepping schemes for the fast hydrodynamic and slow morphodynamic components. The resulting numerical scheme is verified by comparing simulations against (semi–)analytical solutions, and the applicability of our numerical schemes is probed in two test cases: the evolution of a trench in a natural channel, and the hydraulic and sediment transport through a contraction. Finally, conclusions and recommendations for future research are drawn in Chapter 6.

The collected chapters are independent papers that appeared previously in *Hydrological Processes* [21], *International Journal of River Basin Management* [22], and *Advances in Water Resources* [108], with exception of Chapter 5 that was recently submitted to *Computer Methods in Applied Mechanics and Engineering* [110].

Chapter 2

Estimates of flow resistance and eddy viscosity coefficients for 2D modelling on vegetated floodplains

The problem of quantifying the effects of flexible plants on flow resistance and eddy viscosity by vegetated floodplains is first addressed with a 1D approximation based upon the so-called Lateral Distribution Method. The estimates so obtained are then tested with 2D numerical simulations based on the full Shallow Water Equations through the use of the computational code TELEMAC-2D. Data obtained on a physical model of the Besòs river (Spain), whose floodplains were covered with plastic ornamental plants to mimic the effect of flexible vegetation, is used for the validation of the numerical results. Additionally, the values of flow resistance estimated numerically with the 1D and 2D simulations are compared with values obtained in a rectangular flume under flow conditions (slope, water depth and artificial lining) similar to those used on the reduced model. It is then established that as more physical mechanisms are included in the mathematical model used to study the problem, the ratio between the floodplain and the main-channel flow resistance coefficient increases. The approach demonstrates that whenever enough flow data are available, the Lateral Distribution Method delivers values of flow resistance and eddy viscosity which are highly consistent with 2D numerical modelling. This finding could mean considerable saving in the burdensome task of specifying flow resistance and turbulence dissipation values for 2D modelling of large compound channel systems[1].

---

[1] This chapter has been published in *Hydrological Processes*, **18**(15), 2004.

2.1 Introduction

A main-channel flanked with one or two shallow floodplains is usually referred to as a compound channel system (Figure 2.1). In periods of high flow, such systems are characterized by fast-moving flow in the main-channel relative to the slow-moving floodplain flow. Floodplains provide extra storage capacity to attenuate flood peak levels, and allow for the conveyance of excess water, depending on topographical and vegetative characteristics [33]. The topic of compound channel flow has been the subject of intensive research, because of both the unique features of the flow in the vicinity of the main channel-floodplain interface [41, 55], and the impacts of flood wave spreading on occupied floodplains [112, 66]. The problem is characterized by a sudden change in slope of the stage-discharge curve when over-bank flows occurs. Typical theoretical approaches to the problem are either empirically-based [104, 121], or physically-based on turbulence models [80]. Inherent difficulties in analyzing this problem arise from the existence of differential boundary resistance between the main-channel and the floodplains [92]. The determination of flow resistance and turbulence dissipation is particularly relevant in two-dimensional (2D) numerical modelling of large compound channel systems. These systems may have fixed or movable bed topography, in which case the need to solve a broad range of temporal and spatial scales makes the approach highly data demanding. However, though many researchers have demonstrated the complex nature of flow resistance in compound channels, there is still some uncertainty as to how the resistance coefficient might need to be adjusted for floodplain environments, in contrast with the more exhaustively studied case of in-channel flows. More precisely, while in-channel resistance is effectively bounded by known physical ranges [143], the net loss of over-bank flow momentum due to floodplain vegetation has proved hard to estimate [129]. Similarly, the turbulent energy being dissipated by the floodplains, either vegetated or not, represents another important mechanism in the complex flow structure of such compound systems [81]. In this case, the Boussinesq concept of eddy viscosity has proved to be successful in many engineering applications [111, 23] by invoking the hypothesis of turbulence in local equilibrium (i.e., turbulence is dissipated at the same rate at which it is generated [58]). There has been significant progress to compute flow resistance due to vegetation, from the early method based on Manning's n coefficient (see e.g. the review of Sellin *et al.* [123]), the more mechanistic approach of Kouwen [96], to some recent multidimensional numerical calculations [131, 83, 132]. A salient feature of the work of Erduran and Kutija [83] is the use of beam theory to compute the bending of flexible vegetation [96, 137]. Fischer-Antze *et al.* [131] used a 3D turbulent model suitable for rigid, emergent vegetation, while Stoesser *et al.* [132] used the same turbulent model based on the drag-force concept acting on rigid vegetation, either submerged or emergent, to simulate a flood event of the lower River Rhine in South-West Germany. On the experimental side, Sellin *et al.* [123] introduced a method based on expanded aluminium mesh units to simulate flow resistance by floodplain vegetation in large scale hydraulic models.

Nevertheless, the specification of the spatial distribution of flow resistance and turbulence dissipation on the floodplains is still one of the most burdensome tasks in multidimensional modelling, particularly in large alluvial systems with floodplains up to 70 km wide [107], where small scale effects can be ignored in order to compute water level elevations and flow velocities during floods. Thus, there is a need to find a quick way to aid the mathematical modeler to estimate average values of flow resistance and eddy viscosity for 2D modelling.

In this study, the problem of quantifying the effects of flexible plants on the flow resistance coefficient C_F and on the turbulence dissipation coefficient ν_t by vegetated floodplains is based upon experimental data obtained from a physical model of the Besòs River (Spain). The physical model of the Besòs River used plastic plants to mimic the covering of flexible floodplain vegetation, which did not exist on the prototype at the time of construction of the model. The determination of C_F and ν_t is first addressed with the 1D approximation known as the Lateral Distribution Method (LDM) following the work of Darby [129]. In this case, the estimated values of C_F and ν_t are computed by matching the observed lateral distribution of the unit discharge on a selected cross-section of the physical model. The range of values of C_F and ν_t so obtained are then tested with the shallow-water computational code Telemac-2D. The main objective of this work is therefore to demonstrate that spatially-averaged values of the flow resistance and turbulence dissipation coefficients obtained with the 1D LDM model are consistent with 2D numerical results, which in turn are supposed to be bounded by observed experimental data obtained in a 20m long rectangular flume. The proposed approach does not necessarily involve a two step process. Rather, it is aimed at saving computational time when adjusting flow resistance and turbulence dissipation data in any 2D numerical simulation of compound channel flows.

In the next section, a brief description of the experiments performed on a 20m long rectangular flume and on the reduced model of the Besòs River is given first. The 2D Shallow Water Equations (SWE) and the underlying hypotheses that give rise to the LDM are then summarized. This is followed by a description of the 1D and 2D numerical experiments, where the Telemac-2D's results are compared with the unit discharge distribution observed on the reduced model. Finally, the values of flow resistance estimated numerically with the 1D and 2D simulations are compared with values obtained in the rectangular flume under flow conditions (slope, water depth and artificial lining) similar to those used on the scaled experiments.

2.2 Physical model of the Besòs River

The Besòs River runs through an urban part of Barcelona (Spain). In 1975 it was constricted to a 130m wide section, or floodway. Then, in the mid 1990s, the local administration launched an ambitious program called *The Environmental Recovery* of the Besòs River. The main purpose of the restoration project was to use the floodplains of the floodway to construct a wetland system for wastewater treatment. A flexible plant called *Phragmites Australis* that grows naturally along the riverbanks of most Mediterranean rivers was selected for the restoration plan (Figure 2.2). The restoration programme was particularly concerned with the potential increase in flow resistance caused by the future presence of flexible vegetation on the floodplains, and the risks of flooding associated with it. Scaled models were built to assess this effect at the outdoor experimental facility available at the Technical University of Catalonia in 1997-98 [79]. The experimental study required the construction of three different physical models representing 1400 m of the prototype. This paper focuses on the results obtained

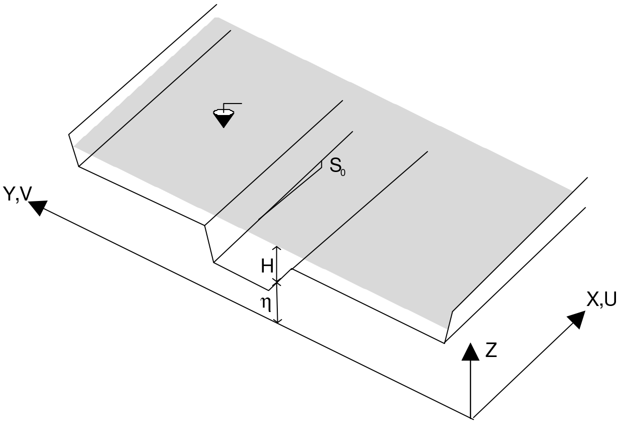

Figure 2.1: Variables definition in a compound channel system (symbols are defined in the text)

for a fixed-bed model (Figure 2.3(a)), built with a dimensions scale of 75:30 (horizontal : vertical). For the main-channel, the bed was covered with fine, loose gravel of 20 mm mean diameter, heavy enough not to be entrained by the flow. For the floodplains, patches of flexible vegetation were modelled with plastic ornamental plants. To this end, and given the established similarities between flows over natural vegetation and flow over channels lined with flexible plastic strips [97], a set of experiments was conducted first in a flume under flow conditions (slope and water depth) similar to those later used on the physical model. The purpose of these flume experiments was to establish the resistance to flow of the plastic strips. Thus, a channel bottom lined with gravel as well as with plastic ornamental plants of different heights, densities and stiffness were tested under uniform flow conditions with a bed slope of 6.5×10^{-3} in a 20-m long, 1-m wide flume (Figure 2.4). Table 2.1 shows the outcome of a series of 10 runs, in which the boundary resistance was assessed with the Manning's formula

$$n = \frac{R^{2/3} H \sqrt{S_o}}{Q}, \tag{2.2.1}$$

where n is the Manning's roughness coefficient ($\mathrm{m}^{-1/3}\mathrm{s}$), R is the hydraulic radius (m), H is the local water-depth (m), S_o is the bed slope, and Q is regarded here for later convenience as the unit discharge ($\mathrm{m}^2\mathrm{s}^{-1}$). While the flow resistance (n value) for the gravel bed maintained a constant value of approximately 0.025, the roughness coefficient for the artificial lining diminished with increasing discharges. This behaviour reflects the fact that flexible plastic plants progressively bend when exposed to stronger shearing flows (Figures 2.3(b,c)). The results shown in Table 2.1 were obtained with a vegetation density of 100 plants/m^2, the same plant density as used on the scaled experiments (Figure 2.3(a)). Then, aside from the flume experiments, a set of curves of flow resistance *vs.* unit discharge as outlined by Kouwen [96] were obtained theoretically for the plants

Figure 2.2: Photograph of the Besòs River with a patch of *Phragmites Australis* on its floodplain, non–existent at the time of construction of the physical model

in the prototype. That required some field work to collect data on plant density and stiffness. The two extreme plant seasons in terms of flow resistance, namely growing and dormant, formed an envelope fringe for the curves. After scaling down this flow resistance to the model, the resultant fringe of Manning coefficients ranged from 0.064 in winter under the lowest unit discharge of 0.045 m^2/s to 0.046 in summer under the highest unit discharge of 0.112 m^2/s. The plastic plant that best mimicked the limit of the reference curves was selected. Full details of this work can be found in [79]. Finally, the model wetlands were constructed with an even distribution alongside the sinuous plan-form of the main-channel (Figure 2.5). Five different flow rates were tested on the physical model and only the higher condition for which the plants were totally submerged, corresponding to a Froude number $F_o \simeq 0.74$, was used in this work. Water depth and flow velocity were measured along seventeen different cross-sections with the aid of point gauges and electromagnetic 2D velocity probes (only twelve of these cross sections are shown on Figure 2.5). No significant changes in the velocity profile were found below and above the tip of the submerged vegetation for the sparse plant density considered in this work (Figure 2.3(a)). This was established in some preliminary runs made with different plant densities (Figures 2.3(b,c)). Thus, one point measurement was deemed appropriate to characterize the mean flow velocity. Then, the velocity measurements were taken at eleven points across each section at 0.4 of the local water depth, as a means of estimating the local mean flow velocity.

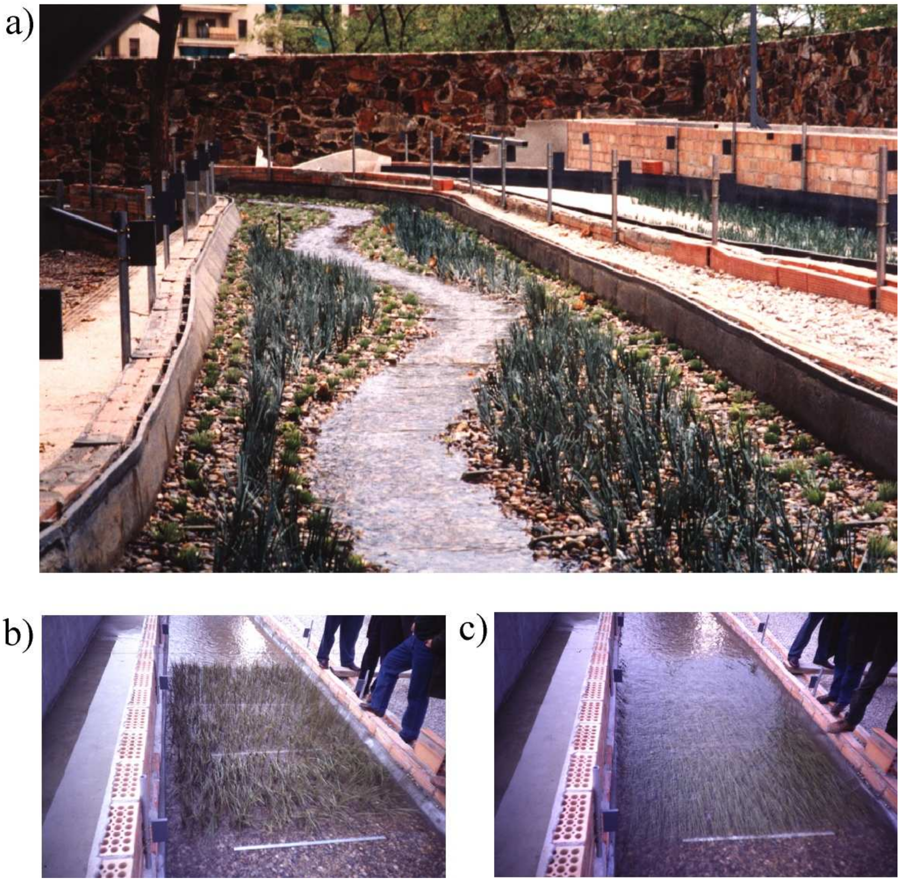

Figure 2.3: (a) View of the physical model of the Besòs River with plastic ornamental plants on the floodplain (Technical University of Catalonia). Preliminary experiments performed on the scale model lined with plastic ornamental plants: (b) low flow conditions, (c) high flow conditions

Figure 2.4: Experiments in a 20 m long rectangular flume and detail of the plastic ornamental plant used for the experiments (see incept).

2.3 The Shallow-Water Model

2.3.1 Equations

If H represents the vertical extent of a flowing water layer, and L represents the horizontal extent over which the flow experiences significant changes, the long-wave approximation states that whenever $H/L \ll 1$, the motion can be analyzed by a horizontal two-dimensional flow formulation [74]. Thus, the conservative form of the depth-integrated Navier-Stokes equations of motion, previously averaged over turbulence, known as the SWE, is

$$\begin{aligned} 0 &= \frac{\partial H}{\partial T} + \frac{\partial (HU_j)}{\partial X_j} \qquad (2.3.1) \\ 0 &= \frac{\partial (HU_i)}{\partial T} + \frac{\partial (HU_iU_j)}{\partial X_j} + gH\frac{\partial H}{\partial X_i} + gH\frac{\partial \eta}{\partial X_i} - |\nabla F|\,\frac{\tau_{W_i}}{\rho} + \\ &\quad + |\nabla G|\,\frac{\tau_{B_i}}{\rho} - \frac{\partial (HT_{ij})}{\partial X_j} \qquad (2.3.2) \end{aligned}$$

The usual convention of vector and tensor analysis has been used here, where terms with a repeated suffix are to be regarded as summed over all their possible values $(i, j = 1, 2)$. In the above equations, and with reference to Figure 2.1, Z is the vertical coordinate, positive upward, $(U_1, U_2) \equiv (U, V)$ are the depth-averaged velocity components along the streamwise and lateral horizontal directions $(X_1, X_2) \equiv (X, Y)$, respectively, T is the time, H is the total water depth (as previously defined), η is the elevation of the stream bed above datum, g is the acceleration due to gravity, ρ is the fluid density, τ_{Wi} is the i-component of the wind stress acting on the free surface, τ_{Bi} is the i-component of the shear stress acting on the stream bed, F is the implicit function denoting the free surface position, G is the implicit function denoting the bed surface position, and T_{ij} is the lateral stresses tensor that includes the viscous friction, the so-called Reynolds stresses, and the differential dispersion terms originating from the lack of vertical uniformity of the horizontal velocity field [25]. In the absence of wind effects, two additional relationships must be specified to close the problem: (i) the bed resistance, $\vec{\tau_B} = (\tau_{B_X}, \tau_{B_Y})$, and (ii) the dispersion tensor T_{ij}. For the former, the classical squared function dependency on the depth-averaged velocity is used

$$\tau_{B_i} = \rho\; C_F\; U_i \left|\vec{U}\right| \quad , \quad \left|\vec{U}\right| = (U_iU_i)^{1/2} \qquad (2.3.3)$$

where the friction coefficient C_F,

$$C_F = \frac{U_*^2}{\left|\vec{U}\right|^2} \qquad (2.3.4)$$

is specified with either Manning or Keulegan relations

$$C_F = gn^2H^{-1/3} \quad , \quad C_F = \left[2.5\;\ln\left(\frac{11H}{K_s}\right)\right]^{-2} \qquad (2.3.5)$$

Table 2.1: Values of Manning roughness coefficient obtained in a 20-m long, 1-m wide rectangular flume with different bed lining (shown in Figure 2.4).

Discharge	**gravel**		**plastic plants**	
Q (m^2/s)	H (m)	n (m$^{-1/3}$s)	H (m)	n (m$^{-1/3}$s)
0.0227	0.053	0.0238	0.109	0.074
0.0455	0.085	0.0254	0.144	0.057
0.0683	0.109	0.0250	0.170	0.049
0.0912	0.130	0.0244	0.196	0.045
0.1091	0.149	0.0251	0.204	0.040

respectively. In the above equations, U_* denotes shear velocity defined by

$$U_* = \sqrt{\left|\vec{\tau_B}\right|/\rho} \quad , \quad \left|\vec{\tau_B}\right| = \left(\tau_{B_X}^2 + \tau_{B_Y}^2\right)^{1/2} \quad , \tag{2.3.6}$$

where n retains its former definition, and K_s represents an effective roughness height. For the Keulegan relationship, if the stream bed of the main-channel is covered with sand waves, the approach of Van Rijn [86] can be adopted to evaluate K_s. By contrast, for overbank flows, the great variety of vegetation cover and soil factors makes it difficult to come up with a reasonable value of floodplain resistance [129]. Nevertheless, the homogeneity of the vegetated floodplains considered in this work means that it is sufficient to use a single value of n, or C_F if enough field data are available to estimate values of K_s as suggested by Kouwen and Li [97].

For the second closure relationship, a simple Boussinesq model is adopted

$$T_{ij} = \nu_t \frac{\partial U_i}{\partial X_j} \tag{2.3.7}$$

where an estimate of the depth-averaged eddy viscosity ν_t is given by

$$\nu_t = \alpha\, U_* H \tag{2.3.8}$$

The parameter α, which could be considered the dimensionless eddy viscosity, may range from approximately 0.07 to about 0.30. The standard depth-averaged value for an infinitely wide channel is $0.41/6 \simeq 0.07$. Knight and April [40] reported a value of 0.13 for their numerical calculations of turbulent flows in compound channels with the LDM. Higher values of α are found in the work of Fischer *et al.* [57]. In terms of absolute values, Bates *et al.* [111] reported the range $[0.1, 2.0]$ m^{2}s^{-1} for ν_t for their 2D river flood simulations. Wilson *et al.* [23] explored a wider range with much smaller values of ν_t when Eq.(2.3.8) was used with TELEMAC-2D to compare the influence of different eddy viscosity models on the computation of stage-discharge curves. A value of α close to 0.07 was finally adopted here for both the in-channel and floodplain areas by matching the maximum value of the measured unit discharge with the value computed with the LDM, as is later described in greater detail.

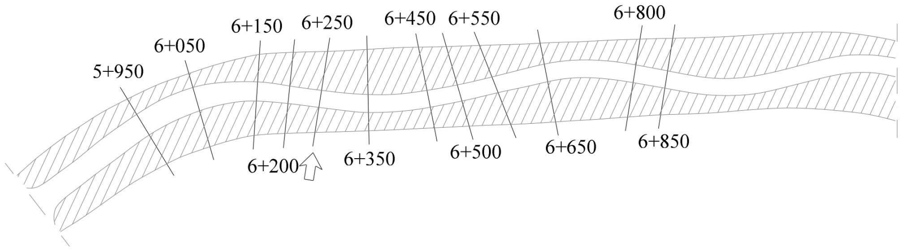

Figure 2.5: Plan view of the physical model of the Besòs River showing the cross–sections where water depth and velocity were gauged

2.3.2 Numerical solution of the SWE

In this study, once Eq.(2.3.7) is substituted into Eq.(2.3.2), and the mass conservation law is applied, the TELEMAC-2D code is used to solve the resultant non-conservative form of the SWE with the finite element method [68]. The standard version of the computational code TELEMAC-2D is based on a fractional step approach, where the velocity components (U, V) are solved first along the characteristic curves, and the Streamline Upwind Petrov Galerkin (SUPG) method is applied to H in the continuity equation to ensure mass conservation. In the SUPG formulation, the standard Galerkin weighting functions are usually set equal to the basis functions with the exception of the convective terms, where perturbed Petrov-Galerkin functions with balancing tensor diffusivity are employed [39, 4]. The latest release of TELEMAC-2D uses the momentum equations to solve the wave equation obtained after eliminating the velocity field from the mass conservation constraint. However, all results presented in this work were obtained with the primitive form of the SWE using a computational domain partitioned in linear triangular elements. Thus, once the computational domain is partitioned into a structured or non-structured mesh with N_e finite elements and N nodes, the dependent variables (U, V) and H are expanded using equal-order interpolation functions. In the second step, the remaining terms not included in the first step are coupled through an implicit time scheme, and the resulting linear system is solved with a variant of the conjugate gradient method [68].

2.4 The Lateral Distribution Method

2.4.1 Equations

It is possible to derive reduced models of the full shallow water equations under certain suitable hypotheses. One such reduced model is the so-called Lateral Distribution Method, introduced by Wark *et al.* [70] and Knight and Shiono [41] among others. In this approach, a slightly different Boussinesq model is adopted for the dispersion term,

$$T_{ij} = \frac{\nu_t}{H}\frac{\partial(HU_i)}{\partial X_j} \tag{2.4.1}$$

where ν_t is now regarded as an adjustable parameter. For the case of a straight compound channel with constant streamwise slope, $S_o = -\partial\eta/\partial X$, a base solution to Eq.(2.3.1) and Eq.(2.3.2) is obtained by assuming a steady parallel flow, $\vec{U} = (U(Y), 0)$. Then, the mass conservation constraint requires

$$Q = Q(Y)$$

i.e., the flow rate per unit width, $Q = UH$, is a function of the lateral direction only. In turn, by virtue of the parallel flow assumption, $V = 0$, the bed shear vector reduces to $(\tau_{B_X}, \tau_{B_Y}) = \rho C_F (U^2, 0)$. Accordingly, the transverse momentum balance equation implies

$$\frac{\partial(H+\eta)}{\partial Y} = 0 \quad , \quad H + \eta = const \ ,$$

and the free surface is flat along the transverse direction. The position of the stream bed surface can be expressed analytically as $G = Z - \eta(X,Y) = 0$, from which the result

$$\beta \equiv |\nabla G| = \left(1 + S_o^2 + S_Y^2\right)^{1/2} \tag{2.4.2}$$

is obtained, where $S_Y = -\partial\eta/\partial Y$ is the lateral stream bed slope. Furthermore, if all dependency upon the longitudinal coordinate X is now dropped, the equation of streamwise momentum becomes

$$0 = -gHS_o + \beta C_F\, U^2 - \frac{d}{dY}\left[\nu_t \frac{d(UH)}{dY}\right] \tag{2.4.3}$$

Eq.(2.4.3) is the model presented by Wark *et al.* [70] to determine the lateral distribution of the unit discharge, and later used by Darby [129] to evaluate the impact of floodplain vegetation on flow resistance. Using Eq.(2.3.8) in combination with Eq.(2.3.4) produces instead the homogeneous version of the equation presented by Knight and Shiono [41], albeit written in conservative form

$$0 = -gHS_o + 2\beta C_F\, \frac{(Q^2/2)}{H^2} - \frac{d}{dY}\left[\alpha\sqrt{C_F}\, \frac{d(Q^2/2)}{dY}\right] \tag{2.4.4}$$

This differential equation is linear in the variable $Q^2/2$, and its non-homogeneous version has been extensively studied by Knight and Shiono [41] , Shiono and Knight [80], Wormleaton [117], and more recently by Ervine *et al.* [33], among others, to analyze the effect of secondary motions in the vicinity of the channel-floodplain interface. In this work, the non-linear form (2.4.3) is preferred due to the direct analogy with some shallow-water flow codes available for 2D numerical simulations such as RMA2 [16] and TELEMAC-2D [130].

It is convenient now to non-dimensionalize Eq.(2.4.3) using the steady normal flow that sets in on a laterally unbounded flat channel with identical streamwise slope. Denoting such normal flow with a zero suffix, Eq.(2.4.3) implies

$$0 = -gH_oS_o + C_{F_o}U_o^2 \tag{2.4.5}$$

using the approximation $|\nabla G_o| = (1 + S_o^2)^{1/2} \simeq 1$. Firstly, Eq.(2.4.5) provides the well-known relation $F_o^2 = U_o^2/gH_o \equiv S_o/C_{F_o}$, which is the Froude number based on the normal flow quantities that set up when friction and gravity are in perfect balance (whereas an increase in S_o tends to accelerate the flow, an increase in C_{F_o} will have the opposite effect). Secondly, by virtue of Eq.(2.3.4), the expression

$$U_*^o = \sqrt{gH_oS_o} \tag{2.4.6}$$

is also obtained, which gives a common estimate of the mean shear velocity in open channel flows when S_o is replaced by the free-surface slope or the friction slope [58]. Thus, upon introducing dimensionless variables based on the normal flow condition, $y = Y/H_o$, $h = H/H_o$, $u = U/U_o$, Eq.(2.4.3) becomes

$$\frac{d}{dy}\left(\frac{\epsilon}{C_{F_o}}\frac{dq}{dy}\right) - \beta\,\frac{C_F}{C_{F_o}}\,\frac{q^2}{h^2} + h = 0 \tag{2.4.7}$$

Here, q is the dimensionless flow per unit width, relative to the base unit discharge U_oH_o, and $\epsilon = \nu_t/U_oH_o$ is the reciprocal of the Reynolds number based on the eddy viscosity ν_t. Therefore, for a given bed resistance $C_F = C_F(y)$, geometry $\beta = \beta(y)$, turbulence dissipation $\epsilon = \epsilon(y)$, and water depth $h = h(y)$, the distribution of discharge per unit width $q = q(y)$ along any given cross-section is totally determined by Eq.(2.4.7). Note that whereas the change of variable $y = -y$ leaves Eq.(2.4.7) invariant, it reverses the direction of increasing y shown in Figure 2.1 when observing data from upstream to downstream, as is customary in hydraulics.

2.4.2 Numerical solution of the LDM

In the present case, Eq.(2.4.7) is solved by the Galerkin formulation of the method of weighted residuals, and discretized into the classical linear functions of the finite element method. The resulting non-linear equation is solved with a Newton-Raphson iteration procedure starting from an initial guess, $q = q_o$, until convergence is achieved within a prescribed tolerance (i.e., until the difference between two consecutive estimates of q, relative to the newer one, is less than or equal to *tol* (e.g., $tol = 10^{-6}$)).

In spite of its simplicity, the solutions to Eq.(2.4.7) obtained by trial and error can quickly provide those values of C_F and ν_t, both in the channel and on the floodplains, that best enable the calculated distribution of unit discharge to match the observed distribution, in flumes or in natural systems. This approach could mean considerable savings in computational time when using 2D codes such as the RMA2 [16] or TELEMAC-2D [130], as explained below.

A word of caution is needed before comparing estimates of flow resistance and turbulence dissipation obtained with models of different dimensionality (1D, 2D, or even 3D). In this work, the flow resistance on vegetated floodplains is estimated with three different models: (1) the n-Manning roughness coefficient obtained from the 1D-Flume data, (2) C_F for the modelling with the 1D-LDM, and (3) C_F for the modelling with the 2D-SWE. Whereas the n-Manning coefficient is empirically based, the friction coefficient C_F is based upon the concept of self-similar turbulent boundary layer. On the other hand, the turbulence dissipation is estimated with the eddy viscosity concept, which relates the effective lateral stresses with the depth-mean velocity field [25]. In brief, then, both C_F and ν_t are physically based coefficients that lump unsolved scale processes that were filtered during the derivation of the SWE. These arguments carry over to the 1D-LDM model, which is a subset of the 2D-SWE under the aforementioned conditions. These unsolved scales represent processes taking place at scales smaller than the limit of the long wave approximation ($H/L << 1$). Therefore, neither C_F nor ν_t should depend on the grid size used in the computation to solve the SWE. Eventually, mesh refinement will be required to capture "layer zones", where the solution exhibits sharp gradients (e.g., the main channel-floodplain interface). In this case, the inflow boundary data will be "spread out" on a region of width proportional to $\sqrt{\nu_t}$ around the streamline direction (see e.g. Johnson [17], pp.174-175). The attempt to capture sharp gradients of the solution with mesh refinement should not be taken as a means of capturing flow features smaller than the limit of the long wave approximation. It can be thought that the limitation of the SWE, either 2D or 3D [116], to solve small scales processes is related with the Large Eddy Simulation (LES) approach used in 3D computations of open channel flows [65], where the interest lies only in solving the large scales of the problem. Both, the SWE model and the LES model, are obtained from the Navier Stokes equations, albeit trough completely different assumptions. By construction, the large-scale fields sought in LES do not need to be solved at scales smaller than Δx, i.e., the grid size, since they are obtained by applying a filter that annihilates all flow details smaller than the wave number $k \sim \Delta x^{-1}$. The Smagorinsky model is commonly used to express the subgrid-scale interactions as functions of the large-scale fields, where the "effective" eddy viscosity ν_t depends on the grid size explicitly [25, 65]. For example, the concept of subgrid-scale eddy viscosity can be used to study the freely decaying turbulence downstream of a grid in a shallow turbulent flow, which is indeed a 3D problem [148]. However, as long as the shallowness of the flow suppresses the three-dimensional regime, the effective eddy viscosity estimated with turbulent boundary layer theory, whose *depth-mean* value is $\nu_t \simeq \kappa U_* H/6 = \kappa\sqrt{C_F}UH/6$ [58], with κ the Von Kármán constant, provides the proper order of magnitude observed on the experiments of Uijttewaal and Jirka [148]. Consequently, some care should be exerted before comparing parameters with the same name in models of different dimensionalities or resolutions because of the changing set of unsolved scales processes which they subsume.

2.5 Numerical experiments

All flows established during the set of experiments performed in the physical model of the Besòs River, albeit subcritical, could be characterized as a thin layer of water flowing at high speed. For the particular case of the experiment considered in this work, the flow rate was 0.171 m^3/s. The average bed slope of the scale model was $S_o \simeq 0.0066$, and the average in-channel values of water depth and flow velocity were $H_o \simeq 0.18$ m, and $U_o \simeq 0.98$ m/s, respectively. The corresponding Froude number F_o was, consequently, approximately 0.74 in the main-channel, and approximately 0.52 on the floodplains.

Among the seventeen cross-sections gauged on the physical model of the Besòs River, three were selected for the initial stage of the present work in order to obtain spatially-averaged values of the hydraulic variables for the application of the LDM. These selected cross-sections were located near the inflection points of the main-channel, away from the channel bends, and quite far from the inlet and outlet regions as well. The sites were chosen to avoid the spatially varying flow conditions that normally set up in the vicinity of the inlet/outlet regions of any physical model, and were found to be representative of the mean flow behavior of the whole model. Moreover, it is reasonable to expect that the flow conditions established in these quasi-straight reaches of the main-channel were approximately within the bounds of the hypotheses that support the LDM, as discussed above in detail. For the full SWE calculations, several cross-sections were later added to verify the robustness of the parameters estimated by the LDM with independent data.

2.5.1 LDM

Table 2.2 summarizes the mean values of the hydraulic variables measured on the selected cross-sections, and required for estimating values of C_F and ν_t for running the LDM code. The convention of Shiono and Knight [80] has been adopted here, i.e., the superscripts mc and fc stand for main-channel and floodplain, respectively. The values of eddy viscosity were initially calculated with (2.3.8) for a parameter value $\alpha = 0.18$, where U_* was computed with (2.4.6) using the spatially averaged values of H included in Table 2.2. For the flow resistance, the Manning coefficient values $n^{mc} = 0.020$ and $n^{fp} = 0.046$ were used first [79], and later converted to C_F values through (6). Without loss of generality, the fitting of the computed values of $q = q(y)$ to the observed values was restricted to cross-section 6+250 (marked with an arrow on Figure 2.5). Numerical results for that cross-section computed with the LDM are depicted in Figure 2.6(a). The calibrated values of ϵ (or ν_t) were obtained by matching the peak values of the observed and calculated distributions of $q(y)$, and by controlling the smoothness of the solution profile in the floodplain regions. In turn, the values of C_F were calibrated by raising or lowering the flat portion of the $q(y)$ curve on both floodplain regions, until a reasonable matching was obtained. The calibrated values of C_F and ν_t are included in Table 2.3.

The adopted calibration procedure can be understood in terms of a sensitivity analysis. A precise measure of model sensitivity can be obtained by considering the changes in model responses with respect to the base -or calibrated- state due to changes in its kth-parameter, a_k. Denoting such a calibrated state with a zero superscript, the perturbed state for the present model is given by $q^o + \Delta q = q(y; a_1^o, ..., a_k^o + \Delta a_k, ...)$ for $a_1 = C_F$, and $a_2 = \epsilon$ (or v_t). The net effect of a change Δa_k on the calibrated value of the parameter a_k^o onto the model output is $\Delta q = (\partial q/\partial a_k)\Delta a_k$, which in turn can be rewritten in terms of the absolute value of the relative error $|\delta q_k| = \kappa(a_k^o)\,|\delta a_k|$. Then,

$$\kappa(a_k^o) = \frac{|\Delta q/q^o|}{|\Delta a_k/a_k^o|} \tag{2.5.1}$$

is known as the sensitivity coefficient of the model dependent variable q with respect to the kth-parameter a_k at the position y. The model is said to be unstable -or sensitive- if $\kappa > 1$, neutrally stable if $\kappa = 1$, and stable -or robust- if $\kappa < 1$; the uncertainty of the model output attributed to the inherent uncertainty with regard to the precise value of a_k^o grows, remains bounded, or attenuates, respectively.

Figure 2.6(b) shows the effect of increasing and decreasing the calibrated value of C_F^o by $\delta C_F = \pm 50\%$, respectively. The net effect of changing C_F is to raise or lower the curve

$q = q(y)$ about its calibrated value. Similarly, Figure 2.6(c) shows the effect of increasing and diminishing the calibrated values of ν_t^o (or ϵ^o) by $\delta\nu_t = \pm 50\%$, respectively. The function $q(y)$ becomes more and more peaked as ν_t diminishes. The sensitivity coefficients for the LDM computed at the centre of the cross-section ($y \simeq 0.82$) are shown in Table 2.4, and it can be seen that $\kappa < 1$ in all cases.

2.5.2 SWE

The calculation performed with TELEMAC-2D started from zero initial condition until convergence to a steady state was achieved for a solver accuracy of 10^{-7}. The values of C_F and ν_t initially used by TELEMAC-2D were exactly those previously obtained with the LDM, with the exception of ν_t^{mc}, since the floodplain value was applied over the entire computational domain. The LDM's calibrated values of C_F were reduced back to their Manning's counterparts through (6), with $H^{fp} = 0.14$ m and $H^{mc} = 0.18$ m (Table 2.2), yielding $n^{mc} \simeq 0.018$ and $n^{fp} \simeq 0.0474$, respectively. The inflow boundary was set at a uniform flow rate of 0.095 m^2/s (= 0.171 $\mathrm{m}^3\mathrm{s}^{-1}/1.8$ m), while the condition at the outflow boundary was prescribed as a constant free surface elevation $H + \eta$ =0.68 m above datum, in agreement with the experimental set-up of the scaled model. The remaining boundary condition was the usual no flow (or free-slip) at solid walls.

The two meshes of finite elements used for the computations with TELEMAC-2D consisted of 780 nodes and 1428 elements for the coarser mesh, and of 2987 nodes and 5712 elements for the finer mesh (Figure 2.7(a)). Both meshes were generated with the SMS's interface [16] and later adapted to TELEMAC's requirement. A typical element size was on the order of 0.4m for the coarser mesh, and approximately 0.2m for the finer (see the inset of Figure 2.7(a)). The representation of the cross-sections geometry (see Figure 2.6) was exact since at least one transition element was used to join the steep channel side slope with the floodplains. Results obtained with both meshes were indistinguishable from each other, and hence are likely grid independent. Figure 2.7(b) depicts the computed unit discharge field, and Figure 2.7(c) depicts the profile of the water surface elevation along the main-channel centerline with the measured values superimposed on the computed profile. It can be seen that the agreement is quite satisfactory, with a root-mean square of the error between the computed and observed values equal to 0.0033m; i.e., the rms of the relative error (with respect to the mean water depth (Table 2.2)) is less than 2%.

Finally, Figure 2.8 includes a comparison of measured *vs.* computed unit discharge in cross-section 6+250, marked in Figure 2.5 and analyzed in Figure 2.6 with the LDM, with the addition of eleven more sections for verification purposes. It is clear that, in spite of some discrepancies, the matching between both sets of data is good in all cross-sections, with a better definition of the peak discharge position than those previously obtained with the LDM. The values of n^{mc} and n^{fp} finally adopted for the TELEMAC-2D simulations were calibrated by matching the observed water surface profile (Figure 2.7(c)), and the gauged unit discharge distribution on the cross-section 6+250. The similarity between the calibrated values of n (or C_F) shown in Table 2.3, and the values previously obtained with the LDM is clear.

A sensitivity analysis performed with TELEMAC-2D using values of the roughness coefficient and the eddy viscosity lower and higher than those included in Table 2.3 showed no degradation of the quality of the numerical fitting shown in Figure 2.7(c)

Table 2.2: Mean values of the hydraulic variables measured in the physical model of the Besòs River.

Variable	**Cross-section**			**Average**
	6+550	6+250	6+200	
H^{mc} (m)	0.179	0.185	0.184	$\simeq 0.18$
H^{fp} (m)	0.133	0.135	0.142	$\simeq 0.14$
U^{mc} (m/s)	0.971	1.000	0.962	$\simeq 0.98$
U^{fp} (m/s)	0.558	0.570	0.560	$\simeq 0.56$
U_*^{mc} (m/s)	0.107	0.109	0.109	$\simeq 0.11$
U_*^{fp} (m/s)	0.099	0.093	0.096	$\simeq 0.10$

Table 2.3: Summary of parameter values.

	Main channel			**Floodplain**		
	C_F	n ($\mathrm{m^{-1/3}s}$)	ν_t ($\mathrm{m^2s^{-1}}$)	C_F	n ($\mathrm{m^{-1/3}s}$)	ν_t ($\mathrm{m^2s^{-1}}$)
1D-Flume	0.0109	0.025	–	0.0510	0.0520	–
1D-LDM	0.0057	0.018	0.0015	0.0425	0.0474	0.0010
2D-SWE	0.0040	0.015	0.0010	0.0417	0.0470	0.0010

and Figure 2.8. The values of the sensitivity coefficients computed with Eq.(2.5.1) are included in Table 2.4, and it can be seen that $\kappa \ll 1$ in all cases. The results generated with the 2D SWE were, as expected, more sensitive to changes in C_F than in ν_t. The corresponding water elevation profiles obtained for a perturbation of $\delta C_F = \pm 20\%$ are shown in Figure 2.7(c).

2.6 Discussion of results

The depth-averaged values of the flow velocity on the scale model were obtained with a one-point measurement at 0.4 of the local water depth from the bed, so a perfect match between computed and observed values should not be expected. Detailed velocity profiles, of the kind presented by Wilson *et al.* [24], will be required to further improve

Table 2.4: Sensitivity analysis.

	1D-LDM			**2D-SWE**		
	$\delta a_k(\%)$	$\delta q(\%)$	κ	$\delta a_k(\%)$	$\delta q(\%)$	κ
C_F^0	+50	−14.30	0.29	+20	1.68	0.084
	−50	29.50	0.59	−20	−0.27	0.014
ν_t^0	+50	−9.90	0.20	+20	−0.75	0.037
	−50	16.40	0.33	−20	0.81	0.041

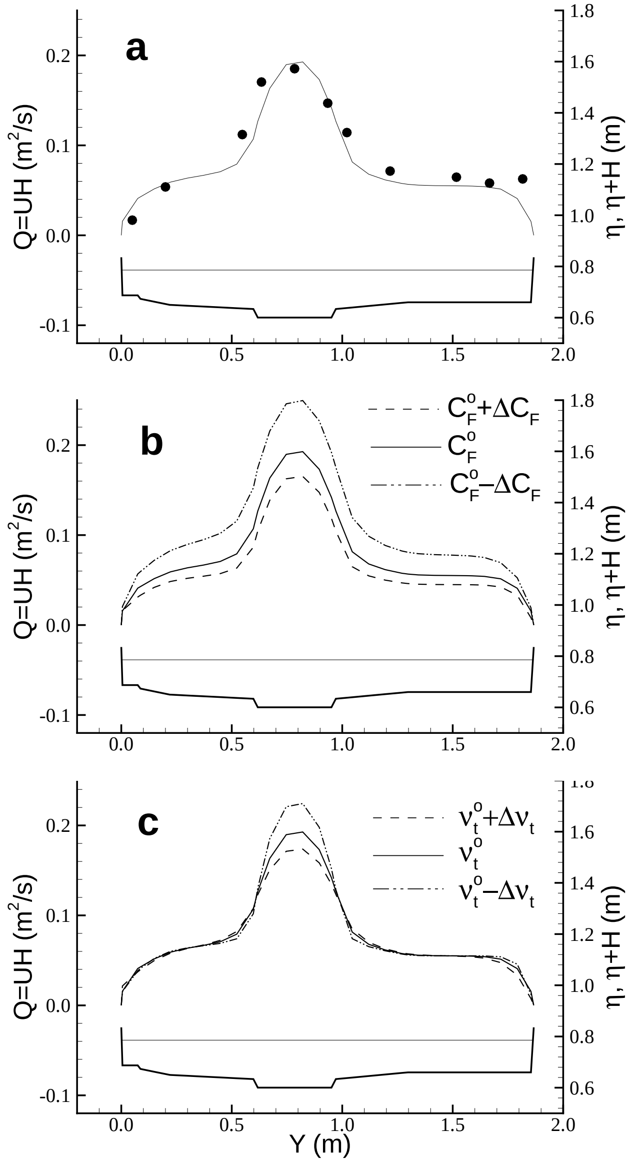

Figure 2.6: (a) Experimental data superimposed on LDM calibrated results on the selected cross–section (marked with an arrow in Figure 2.5). (b) Sensitivity analysis of the model output to changes in C_F with respect to the calibrated values. (c) Sensitivity analysis of the model output to changes in ϵ (or ν_t) with respect to the calibrated values

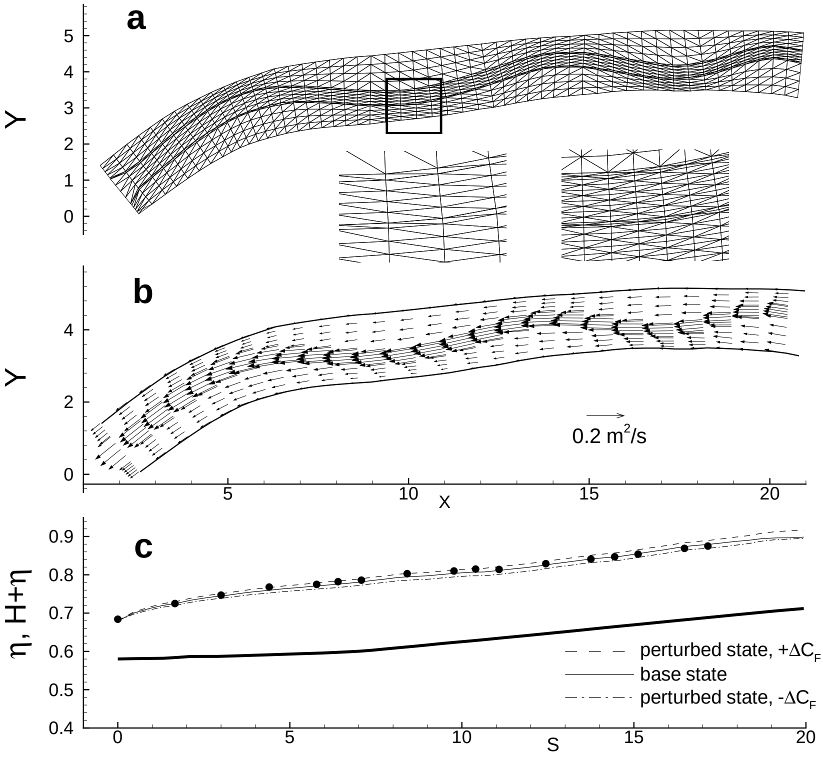

Figure 2.7: Numerical results of the physical model of Besòs River obtained with TELEMAC-2D: (a) mesh of finite elements, the inset gives detail of the two meshes used; (b) computed vector field (unit discharge); and (c) water surface profile along the main channel centre line

the estimates of C_F and ν_t obtained in this work. Nevertheless, and in spite of this shortcoming, the results presented here seem to be very valuable, and the two-step process adopted in this work delivers consistent and robust results. Indeed, the LDM as used here for the 1D calculations is fully compatible with the shallow water model adopted for the 2D calculations, i.e., the SWE solved by TELEMAC-2D reduce to Eq.(2.4.3) under suitable conditions.

Figure 2.6 illustrates the reasonable matching achieved between the LDM results and the physical model data. The numerical results shows a shift in the peak location, likely due to 3D phenomena not represented in the 1D method. Figure 2.7(b) shows that TELEMAC-2D's results tend to locate the maximum velocities, which are proportional to the depicted unit discharges, close to the inner side of the main-channel bends. This result can be attributed to the lack of correction of secondary flow effects [48] in the code. Nevertheless, this effect seems to act as a second order mechanism for the present case, and a much better fit in the peak location is obtained with the 2D calculations, with the exception of the cross-sections tagged S6+650 and S6+550 (Figure 2.8). Moreover, the typical curvature of the free surface induced by the free overfall characteristics as the flow approaches the outflow boundary [43] is clearly captured by TELEMAC-2D's results (Figure 2.7(c)), as may be expected from the experimental set-up of the physical model [79].

From the numerical results obtained with the LDM, an average value of 0.06 $\mathrm{m^2 s^{-1}}$ could be estimated for the unit discharge Q flowing on the floodplains of the physical model. If this value is interpolated with the aid of the flume data (Table 2.1), a value of $n^{fp} \simeq 0.052$ is obtained, while the value of n for the main channel is quite insensitive to variations in Q ($n^{mc} \simeq 0.025$). However, the data extracted from the flume experiments are strictly based on the classical hydraulic approximation of uniform and steady 1D flow. Therefore, the estimates of the Manning roughness coefficient, either tabulated or experimentally determined, implicitly account for the effects of turbulence, not included as a separate mechanism in the underlying 1D formulation (i.e., Eq.(2.2.1)). Indeed, the full 2D SWE model includes inertia, pressure, and curvature effects besides the 1D mechanisms considered by the LDM (i.e., gravity, flow resistance and momentum diffusion). Therefore, and given the fact that the 2D depth-averaged SWE incorporates lateral transfer of mass and momentum and considers independently the mechanism of turbulence, values of flow resistance obtained throughout 1D considerations should be somewhat larger than their actual values [75, 123]. This seems to be the present case (Table 2.3), since the values of flow resistance estimated with the LDM, for both in-channel and floodplain areas, are slightly higher than those used successfully with the 2D calculations, but smaller than the flume values obtained with the 1D formula (2.2.1). This effect is evident in Table 2.5, where the ratio of the flow resistance coefficients between floodplain and main-channel are tabulated for the three models used in this work (i.e., Eq.(2.2.1), Eq.(2.4.3), and Eqs.(2.3.1-2.3.2)). No general claim of validity is made for these results, which may be applicable only to the present experiments. However, it appears that the ratio n^{fp}/n^{mc} increases as more physical mechanisms are included in the model description. Nevertheless, since the LDM inherits some 2D effects not present in the classical Manning expression, its estimates are quite close to the final values used for the 2D calculations. Thus, based upon the aforementioned considerations and the results obtained, it can be said that the LDM might yield an upper bound of

Table 2.5: Ratio between floodplain and main-channel.

	n^{fp}/n^{mc}	C_F^{fp}/C_F^{mc}	ν_t^{fp}/ν_t^{mc}
1D-Flume	2.1	2.8	–
1D-LDM	2.6	7.5	1.5
2D-SWE	3.1	10.4	1.0

flow resistance estimates for 2D numerical modelling.

Finally, and despite the structural differences of the two Boussinesq models used here to close the set of equations of motion, the value of eddy viscosity predicted by the LDM is consistent with the 2D results. Even though (2.4.1) predicts zero normal turbulent stresses for the LDM for the case of steady flow due to the mass-conservation constraint, the closure relation (2.3.7) predicts non-zero normal stresses in case of 2D flows. However, these results are totally compatible since the LDM is by definition insensitive to streamwise turbulent diffusion. The values of the parameter α of the eddy viscosity determined with the LDM on the main channel, $\alpha^{mc} \simeq 0.076$, and on the floodplains, $\alpha^{mc} \simeq 0.071$, were in tune with its standard estimate $\simeq 0.07$, and uniformly used with the TELEMAC-2D simulations.

2.7 Conclusions

In this work, data generated from flume experiments and from a physical model were used to test the capability of the LDM to predict flow resistance and eddy viscosity for vegetated floodplains, as suggested by Darby [129]. The goodness of fit of the parameter values obtained with the LDM were, in turn, confirmed with 2D numerical simulations performed with the TELEMAC-2D computational code, and compared with the values obtained from the flume experiments. It was established that as more physical mechanisms are included in the mathematical model adopted to describe the flow in compound channel systems, the ratio between the floodplain and the main-channel flow resistance coefficients increases. Therefore, and based on those physical considerations, the values of flow resistance and eddy viscosity estimated with the LDM should be considered as an upper limit of their actual values since they include effects that are otherwise explicitly accounted for in a 2D formulation.

In practical situations, both n (or C_F) and ν_t will vary markedly in space and time. Therefore, in periods of flood or high waters, eventually many measurements will be required to characterize the variability of C_F and ν_t under different river conditions. Nowadays, accurate field measurements can be performed relatively fast with an ADCP (Acoustic Doppler Current Profiler), even in large rivers [107]. Nevertheless, whenever water depth and mean velocity distribution data for a given cross-section of a compound system are available, the LDM allows a quick determination of values of flow resistance and eddy viscosity coefficients for both in-channel and floodplain areas that are highly consistent with a 2D numerical simulation. This finding could mean considerable savings in the burdensome task of specifying flow resistance and turbulence dissipation values

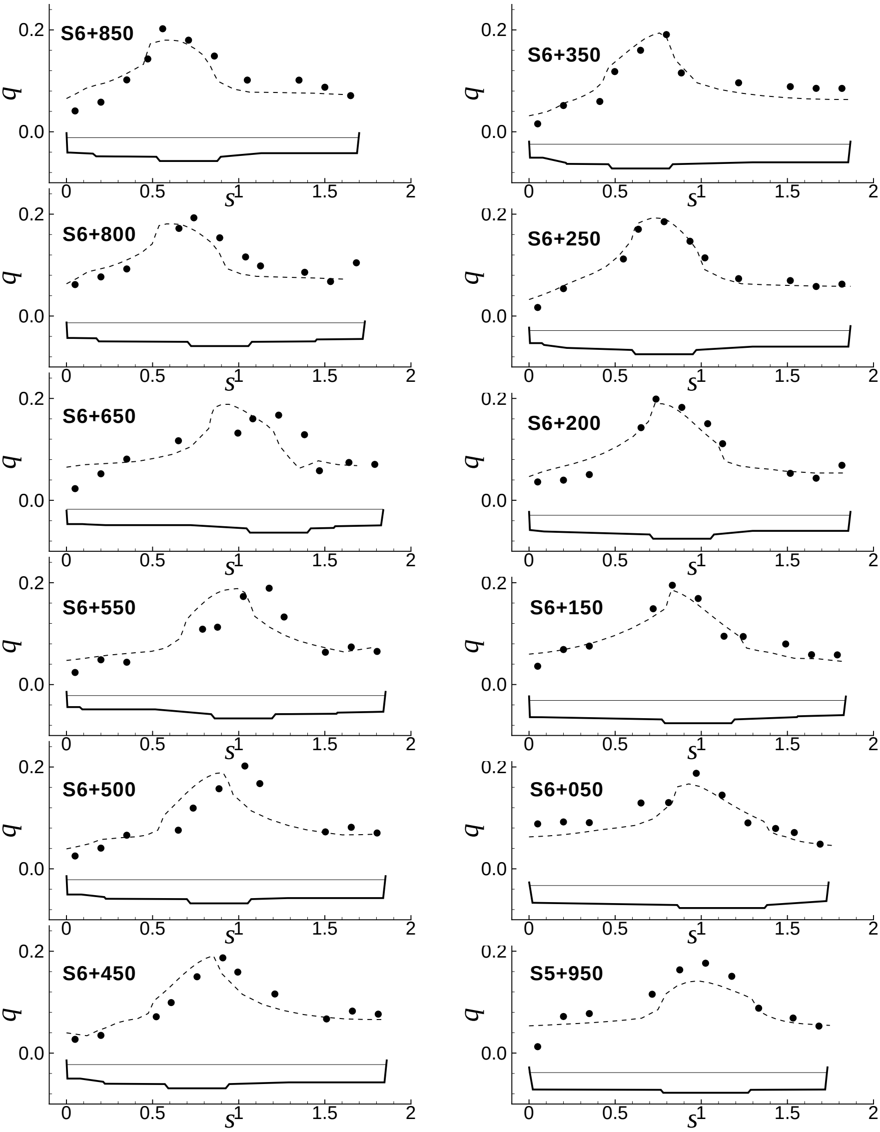

Figure 2.8: Comparison between observed (bullets) and calculated (dashed) unit discharges with Telemac-2D along the cross–sections of the physical model depicted in Figure 2.5

for 2D modelling of large compound system.

Acknowledgments: The set of experiments performed at the Technical University of Catalonia (Spain) were possible thanks to the financial support of the local authorities of Barcelona, the Barcelona Regional Council and the technical assistance of Josep Maria Prió. The numerical experiments were made possible by the financial assistance of CONICET and the Federal Agency for Promoting Science and Technology (Argentina), and their support is also gratefully acknowledged. The authors wish to thank Professor James Bathurst of the University of Newcastle upon Tyne for providing valuable suggestions, and Professor Paul Bates of the University of Bristol for providing thoughtful comments on this work. The authors also would like to thank two anonymous reviewers for their valuable criticisms that help to improve a first draft of the paper.

Chapter 3

Numerical modelling of the catastrophic flooding of Santa Fe City, Argentina

The large plain in the lower basin of the Salado River in west-central Santa Fe State, Argentina, sustains a prolific agricultural activity vital for the local economy. In April-May of 2003, the region suffered the most devastating flood on record for the Salado River, triggered by heavy rains in its lower basin. The west side of the State Capital, Santa Fe City, located at the mouth of the Salado River, was suddenly flooded when a protective levee failed. People living in the floodplains near the city, accustomed to coping with floods characterized by slowly rising water, faced a sudden increase up to 4 m of water in a matter of hours. During the flooding of one third of the city, nearly 120,000 persons were suddenly displaced from their homes, 23 died as a direct result of the flood, and other 43 are believed to have died from post-traumatic distress. This work presents a numerical reconstruction of the event, emphasizing the chain of miss-management decisions made over the years that have a share in the worst environmental disaster of Argentina's recent history[1].

3.1 Introduction

A popular current perception is that man's activities have disrupted most of the earth ecosystems. Hurricane Katrina, which wrecked New Orleans in 2005, the flood of Mozambique in Africa in 2000 [12], the landslides of Venezuela in 1999 in South America [76], and the Hurricane Mitch that devastated Central America in 1998 [12] are just few examples of largely unexpected natural phenomena with devastating consequences for hundreds, or even thousands of people. The magnitude and characteristics of these catastrophes constitute a clear signal that engineers, scientists and policy makers are compelled to

---

[1] This chapter has been published in *Int. Journal of River Basin Management*, **4**(4), 2006.

find a range of options to mitigate river and coastal floods [63]. From a scientific point of view it is difficult, however, to attribute those catastrophes to global warming [94]. Most often, a water-related disaster is directly linked to the sudden failure of a flood protection work [133], a dam break [77, 66], or even tsunamis generated in reservoirs by landslides [13]. Nevertheless, the recent flood of Santa Fe City in Argentina [19] that caused exceptional life and property losses has renewed local public interest in determining if the disaster was mainly provoked by the faulty design of a flood protection work rather than by an extreme river flood event that was beyond the design capacity of the protection structure. The catastrophic flooding of Santa Fe City was indeed initiated by high intensity rainfall concentrated in the lower basin of the Salado River (Figure 3.1). However, the rising waters of the Salado River first overtopped a precarious 5 m long levee located adjacent to the containment wall of a properly engineered levee, known as the West levee (Figure 3.2). Whereas the 7 km long West levee was built with fine and medium-size sand dredged from the Salado River bed and elevated to its final level with a mixture of properly compacted soils, the short non-engineered levee was constructed with loose soils and eventually armored with sandbags, as happened during the big flood of 1998 (Table 3.1). In brief, the purpose of the small non-engineered levee was to provide some protection while permitting access to the golf course located behind the levee on the river floodplain. Meanwhile, the non-engineered levee was meant to be reinforced during periods of high waters to close the existing gap between the West levee and the higher lands nearby (Figure 3.2).

The water overtopping the non-engineered levee eroded the foundation of the containment wall of the West levee until it finally collapsed at 8:30AM on April 29th, 2003. In a few minutes, the incoming water eroded approximately 120 m of the end portion of the West levee, which resulted in the rapid flooding of lowland neighborhoods practically without warning. A few hours later, the water elevation *inside* the city at a point located downstream of the breached area was 2.48 m *higher* than the water elevation on the river side [27].

3.1.1 Extreme Floods in the 20th Century

Santa Fe City is located at 31° south latitude, and oriented from south to north on the wedge formed by the confluence of the Salado River on the west and the alluvial system of the Paraná River on the east (Figure 3.1). There are approximately one half million inhabitants living in the metropolitan area today, a significant proportion of whom occupy both floodplains of the Salado and the Paraná rivers. Extreme discharges of the Paraná River have caused severe property damage to Santa Fe and nearby towns in the past, most notably the flood of 1982-83. Whereas stage records of the Paraná River span a century, the extreme flood of 1905 being the oldest on record, systematic measurements of the Salado River started in 1952. Thus, one of the few recorded extreme floods of the Salado River occurred in 1973, with an estimated peak discharge of $2,400$ m^3/s under the narrow bridge of the Santa Fe-Rosario freeway (Table 3.1). On that occasion, and in spite of the destruction of the freeway bridge and much other state and private property damage as well, the bridge was rebuilt with the same span. In the meantime, more and more low-income people have moved onto the floodplains of both rivers. This influx has been driven mainly by: *i*) the economic crisis of Argentina that forced many residents

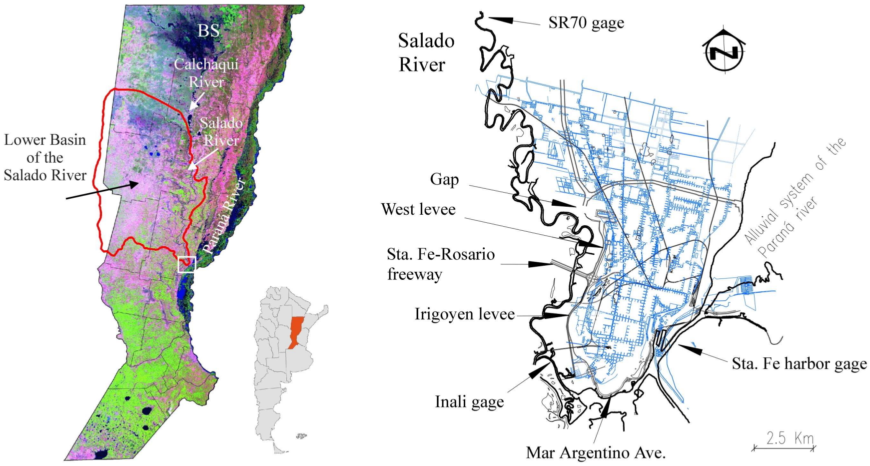

Figure 3.1: Left: Image from Argentinean satellite SAC–C taken on Jun 15/2002, cropped to Santa Fe state limits (see incept). Right: City map showing the location of several references used in this chapter.

of rural areas in northeast Argentina to seek better opportunities in larger cities, and *ii*) the lenience of official authorities to enforce the State law that explicitly prohibits settlements in flood-prone lowlands.

After a major flood of the Paraná River in 1992, the City of Santa Fe, in concordance with State authorities, decided to build several flood-control structures on the Paraná River in the east part of the city, as well as along the Salado River on the west side. With the assistance of loans from the World Bank and the government of Kuwait, the State invested about 74 million dollars in new roads, bridges, and levees all over the region. The main flood-control structure for Santa Fe City against floods of the Salado River was the so-called West levee, a northern continuation of an existing levee named Irigoyen (Figure 3.1). After completion, the whole levee ran parallel to the river for about 7 km, rising 5.2 m on average above the floodplain level. While the first two stages of construction of the West levee were completed, the third and last stage was never completed. The 3-km long third stage of the levee was meant to close a protective ring around the city's northwest side. In the meantime, lured by the sense of security transmitted by the new flood-control structure combined with low real state values, an increasing number of people moved into the west side of the city. Simultaneously, very low income people directly settled onto public lands in the river floodplain.

3.1.2 Extreme Flood of the Salado River in April 2003

Extremely high precipitation saturated the lower basin of the Salado River during the last quarter of 2002 and the first quarter of 2003. From April 20 to April 29, 2003, around 400 mm of rain fell in some regions of the basin (Figure 3.3), whose annual average

River	Year	Discharge (m^3/s)	Stage (m)^{a,b}	Stage (m)^c
Paraná	1905	50000^a	15.35^a	
	1966	42000^a	15.14^a	
	1982-83	62500^a	15.53^a	
	1992	54000^a	15.63^a	
	1998	47000^a	15.36^a	
Salado	1973	2400^b	18.52^b	13.94^c
	1998	2650^b	18.43^b	14.31^c
	2003	3100^c- 3800^b	19.22^b	14.70^c

Table 3.1: Peak discharges and water elevations of floods (gage locations are shown in Figure 3.1, stage readings are referred to mean sea level). ^{a}Santa Fe harbor gage (Paraná River), ^{b}SR70 gage (Salado River),^{c}INALI gage (Salado River).

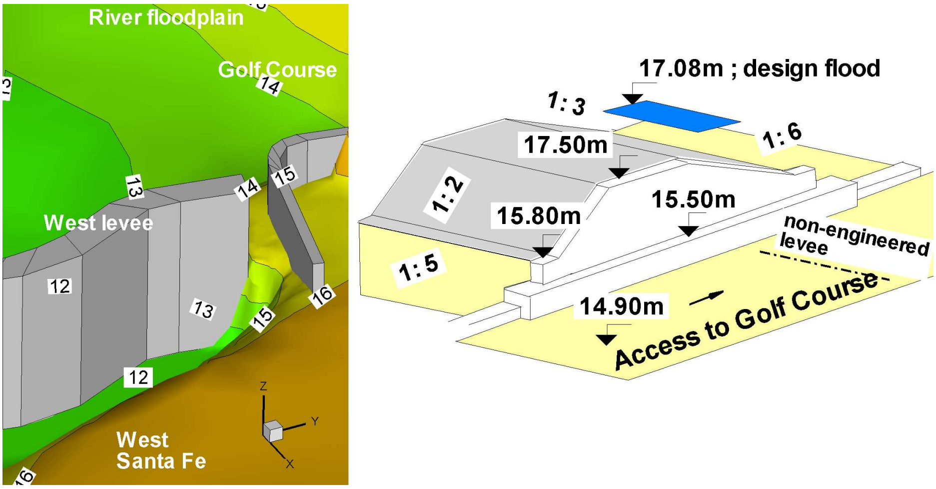

Figure 3.2: Left: Schematic of the West levee showing the gap to provide access to the golf course. Contour levels are referred to mean sea level. Right: Translation of layout 34 c of the original West levee project. The non–engineered levee was 2 m shorter than the West levee.

precipitation is about 1000 mm. The storm return period at one selected station was estimated to be over 100 years [27]. This precipitation generated a flood wave whose peak discharge was estimated at approximately $4,000$ m^3/s, according to measurements taken with an Acoustic Doppler Current Profiler upstream of the State Road 70 (see SR70 gage location in Figure 3.1). The discharge data were obtained on a floodplain-main channel cross section located upstream and far away from the State Road 70's bridge to avoid the typical high-speed approaching flow prevailing in its vicinity. Submerged trees, and submerged wire fences used in Argentina to limit land properties, could have posed the only hazardous situation faced during measurements. The return period for the flood was estimated to be over 250 years [71].

The river overtopped its narrow and wandering channel and spread over its floodplain with unusual strength, destroying bridges and roads, and isolating some small towns in its run toward its outlet to the Paraná River alluvial system near Santa Fe City. People living in west Santa Fe, accustomed to coping with floods from slowly rising water levels, faced a sudden increase in water level of about 4 m in a few hours after the breaching of the West levee. The flooding took a heavy toll, with 23 people dying in the flood, and 43 reportedly dying in the following weeks due to post-traumatic distress [26]. The new 20 million dollar facility for the Children's Hospital, a pride of the city and the region, had 1.5 m of water in its first floor, flooding very expensive equipment and forcing an emergency evacuation of dozens of in-patient children. In the chaos of the first 24 to 48 hours of the flood, an estimated 120,000 inhabitants were displaced. Schools, clubs, government facilities, churches, and non-government organizations sheltered about 50,000 people, while approximately 70,000 people are believed to have sought shelter with friends and family all over the city. One third of the city was under water at some point, including middle- and upper-class neighborhoods. One of the biggest challenges during the emergency was to control the outbreak of diseases related to the stagnant water trapped inside the city for about 3 to 4 weeks. In total, 162 cases of hepatitis and 111 cases of leptospirosis were reported in the weeks following the catastrophe [26]. The total loss attributed to the flood is being estimated on the order of 1,000 million dollars [26], though a large proportion of that is being borne by individuals and, as such, is still unreported.

3.1.3 Objectives

The use of models to test "what-if" failure scenarios of flood protection works was not a widespread practice at the local water authorities' level before the event of 2003. Right after April 29 of 2003, the city flooding seemed to provide a remarkable study case for water resources planning students and prospective engineers as well [90], given the apparent cumulative management errors made over the years that magnified the consequences of an extreme rainfall event in the lower basin of the Salado River. Consequently, a research project was initiated as part of a broader effort to extract some lessons that may be later useful for decision makers on water related issues at the State level. The ultimate goal of the project was to stress that only improving the ability to quantify and manage different flood risk scenarios could lead to effective mitigations actions to protect people, private property and public infrastructure during the occurrence of such extreme events.

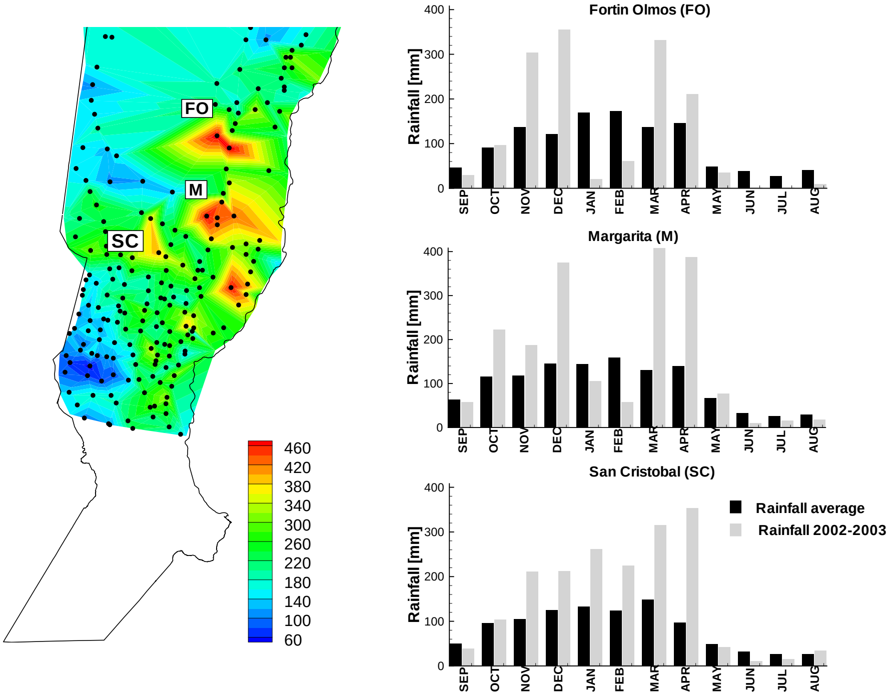

Figure 3.3: Spatial distribution of the heavy precipitation (mm) that fell over the lower basin of the Salado River from April 20th to April 29th. The dots point location of the rain gages. Right: Average *vs.* precipitation fell during 2002 – 2003 on three key gage stations.

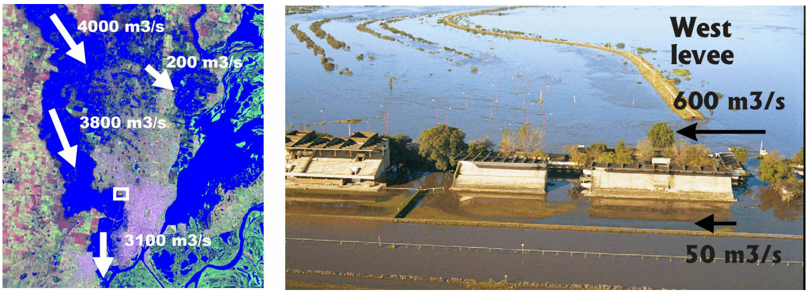

Figure 3.4: Spot image on May 3, 2003, showing Santa Fe city surrounded by water. Flow discharges measured and/or estimated during the event are indicated on the image. The inset delimits the area of the breached levee as shown on the companion areal photograph, whose view is from north to south (image provided by INA – National Water Institute, Buenos Aires, Argentina; photograph provided by "El Litoral" newspaper, Santa Fe, Argentina).

As an initial step towards that goal, this work was particularly designed to: 1) reproduce numerically the most striking features of the wave front that flooded one third of the city in a few hours, seeking a favorable comparison with field observations of inundated depth and flooded area, and 2) compile the errors made over the years by water resources planners and related authorities that contributed to the worst environmental disaster of Argentina's recent history.

A significant part of this study relies on the vast research and applications accumulated over the years in the simulation of time-varying inundation modelling due to natural river floods [113, 78, 93, 125], coastal inundation by storm surges, dam breaks [77, 78], or failure of protective works [82, 133]. These type of problems are usually characterized by a wave front, or water elevation jump, propagating either on initially dry or wet bed conditions. The numerical techniques employed in such studies are often based upon finite difference [136], finite element [68], and variants of the finite volume methods [44].

In the next section, the main geomorphologic characteristics of the lower basin of the Salado River are given first. Then, the underlying hypotheses that support the computations, which closely resemble the steps adopted for the Malpasset dam-break study [78], are summarized. Next, the 2D Shallow Water Equations (SWE) are briefly introduced, followed by the treatment of the topographical and boundary data required for the modelling purposes. The results produced with the code Telemac-2D, and their comparison with field data collected during the event, are then discussed. Finally, the work closes by examining some cumulative management errors made over the years that dramatically worsen the outcome of the flood.

3.2 Materials and Methods

The lower basin of the Salado River, whose loose limits comprise a relatively flat area of approximately $30,000$ km^2 located mostly within the State of Santa Fe boundaries (Figure 3.1), sustains considerable industrial and agricultural activity that is vital for the regional economy, as reflected by the following numbers: in 2002, the region yielded

450 thousands tons of corn, 2 million tons of soja beans, 50 thousands tons of sunflowers, 510 thousand tons of wheat, 450 thousand tons of sorghum, 250 million kg of meat, and 1 thousand million litres of milk, totalling a production capable of feeding up to thirteen million people [91].

The basin itself is part of the large north Pampa system of Argentina [37], which has been undergoing a climate transition to more humid conditions in the last 30 years [95]. Today, the region experiences a subtropical humid climate with a mean annual temperature of 18°C, and with a precipitation gradient from east to west ranging from 900 to $1,200$ mm, respectively, in the period 1971-2000 [95]. The main geomorphological feature of the lower basin of the Salado River is the presence of an elevated block bounded to the west by the Tostado Selva fault [37], inducing a topographical gradient of 10 cm/km in W-E direction and 5 cm/km in N-S direction; therefore, the river runs in a NW-SE direction when entering the Santa Fe State limits until near its junction with the Calchaqui River, then turns south toward its mouth near Santa Fe City. By contrast, the hydraulic gradient of the Salado River in overbank-flow condition is on the order of 20 cm/km. The Calchaqui River drains the region known as Bajos Submeridionales (BS), which is a markedly flat region that is frequently flooded by heavy rains (Figure 3.1). The Calchaqui River is estimated to have contributed with about $1,000$ m^3/s to the flood wave that devastated one third of Santa Fe City on April 29, 2003. There are four other tributaries to the Salado River, among them the so-called Pantanoso River, which contributed approximately another 500 m^3/s to the flood peak [27].

The Salado River is a meandering river with an average channel width of 150 m, bounded by very eroded banks, and flowing within a floodplain belt between 1500 and 2000 m wide. The floodplains are covered with sparse grassland and bushes due to the salty soil left by the periodic flooding of the Salado River, which normally carries an extremely high concentration of salts. The annual mean average discharge is 135 m^3/s for the period 1954-2002, increasing to 176 m^3/s if the period 1971-2002 is considered instead [95]. The mean discharge of the Salado River corresponds to water levels about 1 m below the elevation of the riverbanks. Thus, the bank-full situation corresponds to higher discharges of approximately 300 m^3/s [60].

3.2.1 Mathematical Model

At the time of selecting a mathematical model to study the flooding of a city there are a number of issues that may be worth considering first. One dimensional (1D) models have the advantage of being relatively simple, not very data-demanding and computationally efficient [82] in comparison to 2D models. Nevertheless, a 2D computational code with the ability to handle flooding and drying land processes has the added advantage of simulating the spreading of the flood wave inside a city in a much more realistic situation. Consequently, a 2D model was chosen for this work.

The 2D computations presented here were achieved in two stages or modes: first, in steady-state mode, and second, in dam-break mode, as is commonly done in simulation studies of flood-wave propagation over initially dry land [78]. The steady-state mode refers to the situation where water was not allowed to enter the city through the levee breach, and the transient or dam-break mode refers to the condition where water was allowed to flow through the breaching area over initially dry land.

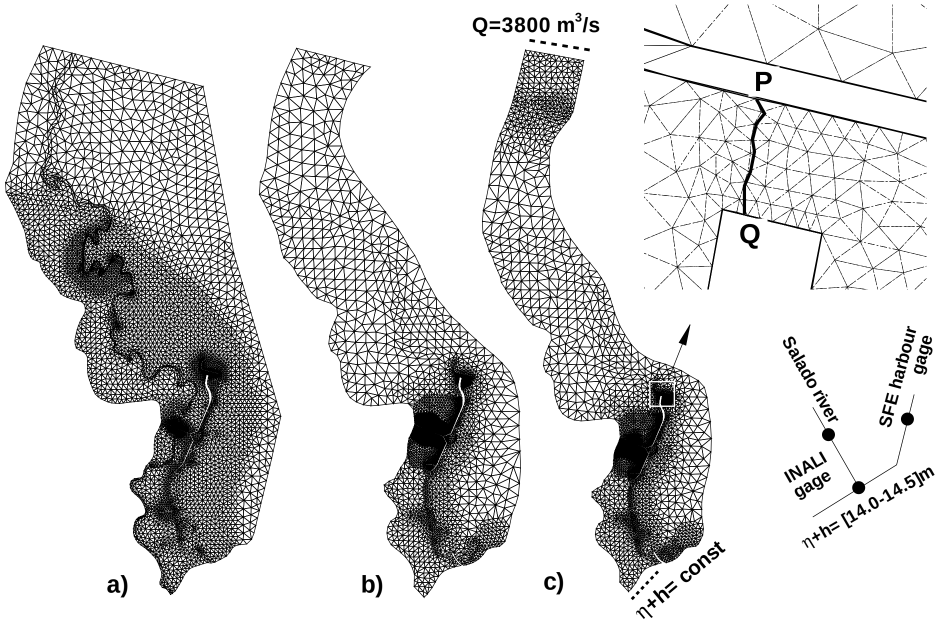

Figure 3.5: (a) High resolution mesh used to define the topography of the modeled area (mesh 1), (b) intermediate mesh used during the computations (mesh 2), (c) final mesh (mesh 4); Inset above: detail of the mesh around the breached levee; Below, schematic of gage positions and outflow BC.

In spite of the fact that the collapse of the protection work itself occurred in two stages, as explained in the introduction, the computations performed for this study were based on the following assumptions: *i*) for simplicity in the computations, a sudden collapse of the protection levee, totalling a breach width of approximately 150 m, was considered, *ii*) the water entering the city only through the levee breach (i.e, the incoming overland flow water from higher lands to the north of the breach (Figure 3.4) was ignored in the computations), *iii*) the conveyance capacity of the main channel of the river was negligible relative to the conveyance capacity of the river floodplains (i.e., if Q_{mc} represents the bank-full discharge of the main-channel and Q_{fp} the discharge of the whole-channel floodplain system considering an even main channel, it follows that the computation assumed $Q_{mc}/Q_{fp} \ll 1$ for all practical purposes), and consequently, *iv*) the hydraulic resistance of the main-channel floodplain system was uniform for the steady-state computation and increased for the transient simulation, differentiating river from urban areas [78, 125], *v*) the upstream river discharge, imposed as an inflow boundary condition onto the modelled area, remained constant during the transient computation, *vi*) the flowing water was bounded from above by a free surface free of wind effects and from below by a rigid and smooth bottom, and *vii*) the water motion was predominantly horizontal, where small-scale effects acted as an effective eddy viscosity on the large-scale motion [1].

For the transient simulation, the hydraulic resistance within the main channel-floodplain system is assumed to preserve the value used for the steady-state simulation, albeit higher within the city to represent the augmented surface roughness effect typical of an urban area. Other assumptions are justified on the grounds that some simplifications are required in order to perform the computations (e.g., a *sudden* levee failure is much more tractable than a *progressive* failure [133]), whereas others are justified on the grounds of available data. First, a crude estimate done during the emergency yielded an incoming overland flow of about 50 m^3/s (Figure 3.4), compared with the estimated incoming 600 m^3/s through the levee breach [27]. Secondly, the Salado River has a bank-full discharge of the order of 300 m^3/s [71], compared with the $4,000$ m^3/s flowing throughout the whole main-channel floodplain system for the flood studied here. An independent check using the Lateral Distribution Method [21] yielded a slightly higher bank full discharge than 300 m^3/s albeit consistent with the cited value of [71]. All these estimates yield $Q_{mc}/Q_{fp} \simeq 0.08$ and, so adding the main-channel conveyance capacity should have no major effects on the computations. The validity of this hypothesis was also reported by Hervouet [78] for the Malpasset dam-break study. In other words, as long as the constraint $Q_{mc}/Q_{fp} \ll 1$ is satisfied, any error that could be embedded in the topographical representation of the river main channel becomes, within some prescribed tolerance, irrelevant. An added advantage is that there is no major need to distinguish hydraulic resistance and eddy viscosity values between the main channel and the floodplains, as is normally required in situations where the conveyance capacity of both components are of the same order [21] (e.g. the Paraná River is characterized by a ratio $Q_{mc}/Q_{fp} \simeq 1$ [107]).

With the aforementioned hypotheses in mind, if the vertical extent of a flowing water layer, h, is assumed small in comparison with the horizontal length of the wavelike motion of the fluid, l (i.e., if $h/l \ll 1$), the motion of a free-surface flow can be analyzed by a horizontal 2D formulation known as the long wave approximation [74]. The resulting equations, known as the Shallow Water Equations (SWE) or as the Saint Venant equations, can be obtained from the depth-integrated form of the Navier-Stokes equations of motion, previously averaged over turbulence:

$$\frac{\partial h}{\partial t} + \nabla \cdot \mathbf{u} h = 0 \tag{3.2.1}$$

$$\frac{\partial \mathbf{u}}{\partial t} + \mathbf{u} \cdot \nabla \mathbf{u} + g \nabla h = -g \nabla \eta - \frac{\tau_b}{\rho h} + \frac{1}{h} \nabla \cdot (h \, \nu_t \nabla \mathbf{u}) \ , \tag{3.2.2}$$

where h is the water depth, $\mathbf{u}$ is the depth-averaged velocity vector with (u, v) components in the (x, y) horizontal directions, respectively, t is the time, η is the elevation of the stream bed above datum, g is the acceleration due to gravity, ρ is the fluid density, τ_b is the shear stress vector acting on the stream bed, and ν_t is the turbulent eddy viscosity that models the lateral stress effects that include viscous friction, the so-called Reynolds stresses, and the differential dispersion terms originating from the lack of vertical uniformity of the horizontal velocity field [25]. In the absence of wind effects, two additional relationships must be specified to close the problem: (i) the bed resistance, $\tau_b = (\tau_{b_x}, \tau_{b_y})$, and (ii) the turbulent eddy viscosity. For the former, the classical squared function dependency on the depth-averaged velocity is used

$$\tau_{b_x} = \rho \, \mathrm{C_F} \, |\mathbf{u}| \, u \quad , \quad \tau_{b_y} = \rho \, \mathrm{C_F} \, |\mathbf{u}| \, v \quad , \quad |\mathbf{u}| = \left(u^2 + v^2\right)^{1/2} \quad , \tag{3.2.3}$$

where the friction coefficient $\mathrm{C_F}$,

$$\mathrm{C_F} = \frac{u_*^2}{|\mathbf{u}|^2} \quad , \tag{3.2.4}$$

can be specified with either Manning or Keulegan relations

$$\mathrm{C_F} = g \, n^2 h^{-1/3} \quad , \quad \mathrm{C_F} = [2.5 \, \ln(\frac{11h}{k_s})]^{-2} \quad , \tag{3.2.5}$$

respectively, where n represents the Manning roughness coefficient, and k_s represents an effective roughness height. In the above equations, u_* denotes the shear velocity, defined by

$$u_* = \sqrt{|\tau_b| / \rho} \quad , \quad |\tau_b| = \left(\tau_{b_x}^2 + \tau_{b_y}^2\right)^{1/2} \tag{3.2.6}$$

For the second closure relationship, a proper estimate of the depth-averaged eddy viscosity ν_t is given by the Elder model [57].

$$\nu_t = \alpha \, u_* \, h \tag{3.2.7}$$

$$= \alpha \sqrt{\mathrm{C_F}} \, |\mathbf{u}| \, h \tag{3.2.8}$$

The model (3.2.7) is used here to specify an average eddy viscosity value, held constant during the simulations, in which case the mean shear velocity is estimated according to the procedure of Nezu and Nakawaga [58]. Alternatively, (3.2.8) can be used whenever the friction coefficient $\mathrm{C_F}$ is known. The parameter α, which could be considered the dimensionless eddy viscosity, may range from approximately 0.07 to about 0.30 [21]. The

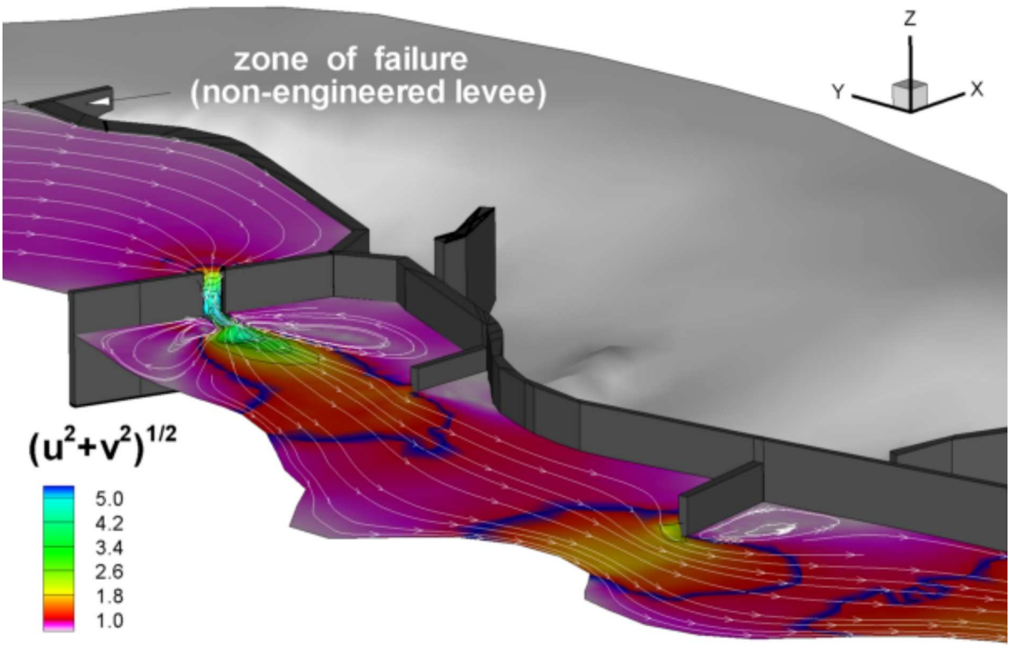

Figure 3.6: 3D projection of the steady–state simulation with an inflow BC of 3, 800 m^3/s.

standard depth-averaged value for an infinitely wide channel obtained with equilibrium turbulent boundary layer theory is $\alpha = \kappa/6$, where κ is the Von Kármán constant (see [148], for example). This estimate yields the lower bound of 0.07. Higher values of α are found in the work of Fischer *et al.*[131].

3.2.2 Numerical Solution of the SWE

The TELEMAC-2D code is used in this study to solve the primitive form of the SWE given by Eqs.(3.2.1) and (3.2.2) with the finite element method [68]. The standard version of the computational code TELEMAC-2D is based on a fractional step approach, where the velocity components (u, v) are solved first along the characteristic curves, and the Streamline Upwind Petrov Galerkin (SUPG) method is applied to h in the continuity equation to ensure mass conservation. In the SUPG formulation, the standard Galerkin weighting functions are usually set equal to the basis functions with the exception of the convective terms, where perturbed Petrov-Galerkin functions with balancing tensor diffusivity are employed [39, 4]. Briefly, the TELEMAC-2D code starts from some given initial and boundary conditions, and advances the solution one time step, Δt, for u, v, and δh, since the mass conservation constraint is treated explicitly in the form $\delta h + \Delta t \, \nabla \cdot (\mathbf{u}\, h^n) = 0$, where h^n represents the water depth at the previous time step, and $\delta h = h^{n+1} - h^n$ is the computed free-surface increment at each time step.

All results presented in this work were obtained with the primitive form of the SWE using a computational domain partitioned into linear triangular elements. Thus, once the computational domain is partitioned into a structured or non-structured mesh with N_e finite elements and N nodes, the dependent variables (u, v) and h are expanded using equal-order interpolation functions. In the second step, the remaining terms not included in the first step are coupled through an implicit time scheme, and the resulting linear system is solved with a variant of the conjugate gradient method [68].

3.2.3 Model Area and Boundary Conditions

The digital representation of the topography of the affected area for the post-flood assessment was developed using official cartographic maps provided by the Geographic Institute of the Argentinean Army (IGM). Local topographic features which were not represented in the maps, such as levees in the floodplain, were later integrated into the digital terrain model (DTM) used for the numerical simulation. The lack of information was particularly severe in the northern part of the modeled area, near SR70, where a few contour levels 0.5m apart were available for such a low gradient river. Data from a few cross sections of the main channel of the Salado River were used, though none were available on the area near the bridge of the Santa Fe-Rosario freeway. So, in this case, an old data survey of the cross section at the freeway bridge was used to recreate the riverbed topography. In brief, the interpolation of the topography data to a high-resolution finite element mesh (Figure 3.5) was based on high resolution elevation data inside the city, particularly within the flooded urban area, and on sparse data in the northern part of the modeled area. Nevertheless, the few data available on the floodplain were deemed adequate under the premise that the conveyance capacity of the main channel is negligible in comparison with the conveyance of the floodplains.

A series of post-processing procedures were applied to detect potential discrepancies between the DTM and ground observations, particularly near the area of the breached levee. Both resolutions, the vertical and horizontal scales of the DTM, were based upon the topographic information available. The resulting DTM was estimated to have few centimetres of uncertainty in the lower half portion, which covers the zone of interest in this study with the exception of the riverbed near the freeway bridge. A maximum vertical uncertainty of ±30 cm was estimated at the northern half of the modelled area, where contour levels were available at 50 cm intervals. These estimates arose from the comparison of the interpolated DTM with few topographic profiles surveyed by the Santa Fe Water Resources Department during the emergency. The horizontal spatial resolution is proportional to the size of the finite elements used for interpolating the topography, i.e., 25-40 m in the river channel, 50-75 in the floodplain, and 250-350 m in the northern portion of the modelled area (Figure 3.5a). The high-resolution finite element mesh containing topography data (Figure 3.5) was, in turn, used to interpolate bed elevation data to several coarser meshes used for the computations (Table 3.2).

The limits adopted in the final computational domain resulted from trial and error, where one of the main objectives was to determine the approximate extent of the flooded area in order to save memory and computing time. To that aim, a very coarse mesh was first used, as indicated in Table 3.2. The final computational domain occupies about 88 km^2, extending 25 km in N-S direction from 3 km upstream of the SR70 up to the point

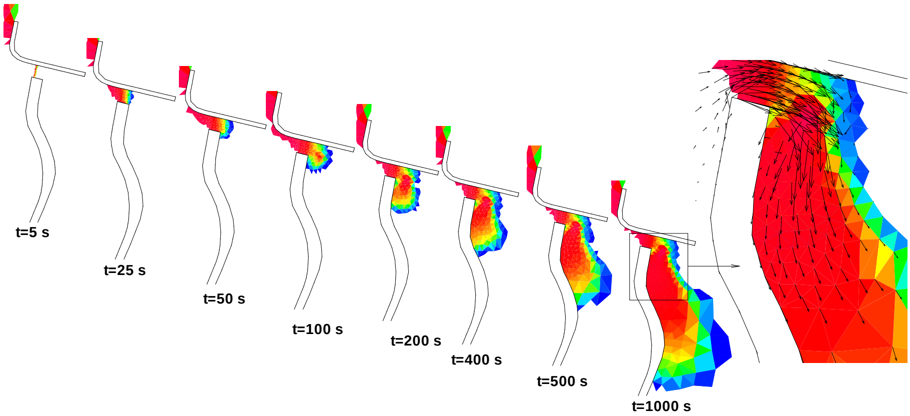

Figure 3.7: Wave front propagating over initially dry land inside the city, after a sudden breach of the West levee.

where the Salado River discharges into the alluvial system of the Paraná River (Figure 3.5). The average width of the floodplain along the modeled reach was 2000 m. Included within the model domain were the lowland areas in the western part of the city. Meshes 3 and 4 were defined over the same computational domain, the latter being a refinement of the former. So only one of them is shown in Figure 3.5c.

Figure 3.4 included an aerial photograph of the breached levee as well as a Spot image of Santa Fe City and its surroundings taken on May 3, 2003. The image shows different locations where the river discharge was measured and/or estimated: a) 200 m^3/s diverted from the Salado River to the alluvial system of the Paraná River in the northern part of the city (at one point, the city was completely surrounded by water), b) $3,800$ m^3/s coming down from the north near SR70, and measured with an ADCP, c) 600 m^3/s coming into the city trough the levee breach, d) 50 m^3/s entering the city as overland flow from relatively high land situated north of the breached levee, and e) $3,100$ m^3/s discharging into the Paraná alluvial system at the Salado River's outlet, and measured with an ADCP. The peak flood discharge was estimated at $4,000$ m^3/s upstream of SR70 before reaching the flow diversion to the alluvial system of the Paraná River. Thus, the combined flows illustrated in Figure 3.4 yield an estimated error on the flux mass balance on the order of 50 m^3/s, which represents a relative error of 1.25% with respect to the peak flood discharge [27].

Boundary conditions were defined at the upstream and downstream borders of the computational domain. Upstream, a piecewise constant-inflow condition was set until the flow rate reached the observed peak discharge value of $3,800$ m^3/s. This value was later decreased to $3,600$ m^3/s to determine the sensitivity of the model response to changes in the prescribed boundary conditions. The downstream boundary condition was defined as a constant water level ranging from 14.0 to 14.5 m along the outflow cross section (see Figure 3.5).

Mesh	**nodes**	**elements**	**used for**
1	5212	9848	topography
2	2075	3744	hydrodynamics
3	4190	7765	”
4	4464	8289	”

Table 3.2: Different meshes used for the computations.

3.3 Results

Several Landsat 5 and 7 images, as well as topographic data, were processed with ENVI [122] to define the computational domain. Mesh generation and modifications to bed topography data were treated with the SMS interface [16], and later converted to TELEMAC-2D portable files with the STBTEL interface [130]. In turn, the appropriateness of the results were assessed through the use of the RUBENS interface [130] and the visualization software TECPLOT [47]. It was necessary to write a simple code to make TELEMAC's outputs compatible with TECPLOT.

The flow through the breached levee is a function of the difference between water levels behind the levee (in the river) and immediately downstream. At the beginning, the breached levee behaves as a lateral weir, branching the main flow discharge and inducing changes in the local water surface elevation of the river nearby the gap. A much simpler set up would be given by freezing the water surface elevation behind the levee without solving the river flow behind the levee. However, the comparison of solutions obtained by different modelling strategies is not within the scope of the paper. The fully coupled flow simulation between the river flow behind the breached levee and the forward wave propagating on initially dry land after breaching was chosen instead. This scenario closely mimics the actual conditions observed during the emergency.

Consequently, the computations were performed in two steps, a steady-state and a transient simulation. The steady-state simulation was carried out with the aim of obtaining a reasonable distribution of water elevations and flow velocities on the river side that would drive the transient scenario. Achieving a steady-state condition within the floodplain limits (i.e., with the levee breach closed), was actually much more computationally demanding than the transient simulation. Instead of starting from zero initial conditions, which converged extremely slowly for a solver accuracy of 10^{-7} with the available computational resources, the computation was initiated assuming a water elevation distribution (say $z_w = h + \eta, = const$) compatible with the bed slope along the river over all of the computational domain. This initial interpolation was such that the condition $h > 0$ was satisfied for all nodes pertaining to the river domain (i.e., within the floodplains limits). Consequently, it was necessary to raise the ground elevation, η, of the mesh nodes inside the city in order to avoid an artificially flooded situation. Thus, wherever the condition $\eta > z_w$ was satisfied, a zero water depth was assigned to the corresponding node, as required. This initial condition speeded up the convergence to the sought steady-state solution quite remarkably by imposing a staircase inflow hydrograph, starting with 500 m^3/s and progressing up to the required $3,800$ m^3/s with increments of about 1000 m^3/s. Once the steady state solution was available, the ground elevations of the city were restored to their original values just by trading out the topography input files.

Because some numerical instabilities were observed near the Santa Fe-Rosario freeway bridge, the mesh around that area was highly refined to model accurately the effects of the flow contraction and the sharp increase on the free surface elevation upstream of the structure. Small elements were also placed at the breaching zone and all along the inner side of the West levee, since the wave front initially propagated over the freeway belt that runs parallel to the levee (see the city map in Figure 3.1 for details). In brief, several meshes with different levels of refinement were used (Table 3.2) until the mass flux discrepancy was less than 1.5%, which was deemed negligible and, therefore, likely mesh-independent.

Uniform values of the hydraulic resistance, in terms of the Manning's roughness coefficient n, and the eddy viscosity were used across over all of the computational domain. The roughness coefficient was later increased for the dam-break mode simulation in order to assess the additional resistance effects due to the urban area [78, 125]. Consequently, initial values of n were set between 0.021 and 0.025 for the steady-state simulation, and later increased to 0.030 for the transient simulation, whereas the eddy viscosity was set equal to $0.1 m^2/s$ throughout the simulations. Usually, the value of the eddy viscosity has rather limited impact on the SWE results, with the model output being more responsive to changes in the hydraulic resistance coefficient [78, 21]. However, instead of calibrating the model by adjusting the hydraulic resistance coefficient to achieve the best fit to the few available data, the model was calibrated by varying the water elevation at the outflow boundary within the physical range $[14.0 - 14.5]$ m, until the observed stage value at the INALI gage was matched at the moment of interest, as it is explained next. This strategy was adopted to work around the uncertainty present in the water elevation value at the river confluence with the alluvial system of the Paraná River during the flood peak. At that moment, there was about a 1 m difference between the readings of the Santa Fe (SFe) harbour and the INALI gages (Figures 3.1 and 3.5).

Figure 3.6 shows the free surface at the end of the steady-state simulation. Note the considerable difference in the free surface elevations upstream and downstream of the Santa Fe - Rosario freeway bridge caused by the severe flow contraction. The simulated difference was 1.4m while the observed difference was estimated to be around 1.2m, although this figure is not known to be reliable. This discrepancy, if any, could be attributed in part to the inaccurate representation of the alluvial valley topography adopted for the simulation in the upper portion of the computational domain, upstream of the freeway bridge, which was on the order of ±30cm as explained in Section 3.2.3, and more likely to the combined effect of a poor representation of the riverbed topography and the hydraulic resistance on the bridge.

Figure 3.7 shows the first stages of the wave front propagating inside the city at different times when the gap closure was removed for the transient simulation, obtained with a $\Delta t = 1$ s after starting with the initial condition depicted in Figure 3.6. The inset shows a detail of the velocity field and water depth contours. The gap was assumed to be 150 m wide and to extend down to ground level as shown in Figure 3.2. To complete the transient simulation, larger $\Delta t = 2, 5, 25$ and 50 s, were used. From some preliminary computations, it was found that the solution obtained with $\Delta t = 25$ s reproduced the features of the solution obtained with finer time increments quite remarkably.

The river discharge to the city through the breach was computed with the following line integral, defined over a polyline across the breach joining the two extreme points P and Q (Figure 3.5c)

$$Flux|_{\widehat{PQ}} = \int_{\widehat{PQ}} (\mathbf{u}\,h \cdot \mathbf{n})\, ds \tag{3.3.1}$$

where the unit vector normal to the differential line element $\delta\mathbf{s} = (\delta x, \delta y)$ is $\mathbf{n} = (-\delta y/\delta s, \delta x/\delta s)$, where $\delta s = (\delta x^2 + \delta y^2)^{1/2}$. Consequently, it was advantageous to introduce the standard stream function concept (i.e., an unknown scalar function $\psi(\mathbf{x}, t)$) such that

$$uh = -\psi_y \quad , \quad vh = \psi_x \tag{3.3.2}$$

Then, in the limit $\delta s \to 0$, the above line integral becomes

$$\begin{aligned} Flux|_{\widehat{PQ}} &= \int_{\widehat{PQ}} -\,u\,h\,dy + vh\,dx \\ &= \psi(\mathbf{x}_Q, t) - \psi(\mathbf{x}_P, t) \end{aligned} \tag{3.3.3}$$

The line integral (3.3.3) was evaluated for each time step of the transient computation using, for compatibility with TELEMAC-2D solution method, 1D linear piecewise functions locally defined over each side of the finite elements belonging to the polyline $\widehat{PQ}$. The outcome of this evaluation is depicted in Figure 3.8 for the same elapsed time as shown in Figure 3.7. The graph shows that the discharge entering the city attains a maximum value few seconds after the breaching of the levee, then smooths out to a constant value of approximately 540 m^3/s. This value is quite close to the estimated value of 600 m^3/s obtained by tracking floats, and reported by the Water Resources State authorities [27]. These first 1000 s of the transient simulation were obtained with $\Delta t = 1$ s after starting from the steady-state solution depicted in Figure 3.6, whereas the remainder of the simulation was continued with $\Delta t = 25$ s. Though not shown here, the inflow rate depicted in Figure 3.8 diminishes as the lowland neighborhoods filled up with water with increasing time. The inflow rate is quite sensitive to the assumed shape of the gap. Nevertheless, the computed values of the incoming flow were obtained assuming a breach of rectangular cross-section whose lower lip had the bed elevation shown in Figure 3.2, which was deemed reasonable given the lack of topographic data in and around the breaching area.

A 3D projection of the progression of the flood wave inside the city at different times is plotted in Figure 3.9. The view point on the right part of Figure 3.9 was reversed to get a better sight of the large extent of the flood wave in the southern part of the city. The flood extent 25 hrs after the breaching compares favourably with the affected area as captured by the Spot image on May 3 (Figure 3.4). The comparison is just qualitative, since the satellite image was taken 3 days after levees were ruptured in six different places to release the trapped water inside the city. One feature that emerged from the simulation is that the railroad levees built by French engineers at the end of the nineteenth century (one of them still in use) delayed the propagation of the flood wave.

The delay in the flood wave propagation due to the presence of the railroad levees is also expressed in Figure 3.10, where the water depth evolution along the inner side of

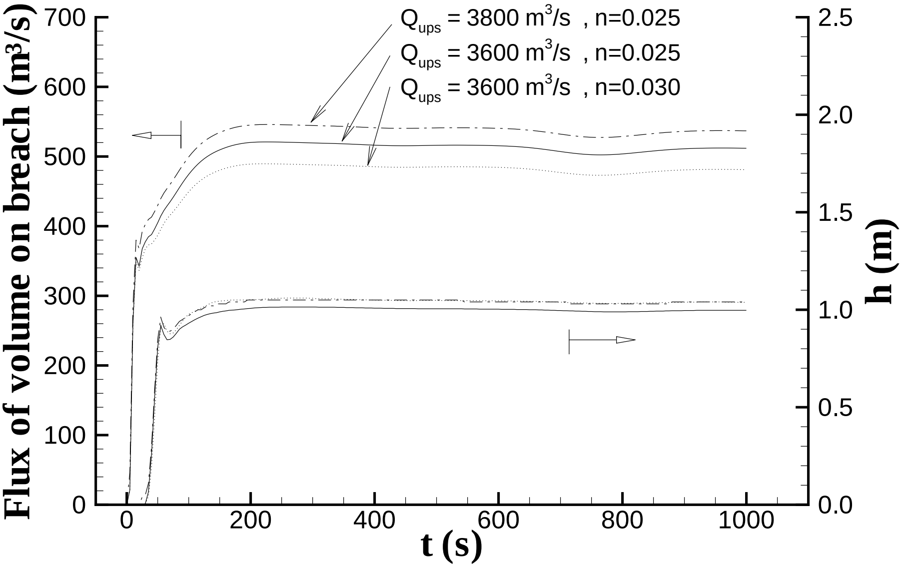

Figure 3.8: Flux of volume entering the city after the sudden breach of the West levee. Water depth is also shown as time progresses on a point located nearby the breach.

the West levee is depicted at different points approximately equally spaced. The water elevations measured on the INALI and FyG gages are also plotted on the same figure for comparison with the numerical results. The mild depletion of the simulated water level at FyG at the beginning of the transient computation is in response of the huge amount of water entering the city. Meanwhile, the simulated rising curves of z_w inside the city are bounded by the FyG readings at the end of the simulation time. Around 27 hr after the breaching, a measurement taken by the local division of the National Water Institute (INA) near the river outflow reported a water level difference of 2.48 m at both sides of the West levee. It was clear by then that the city had become a reservoir, as shown in Figure 3.9. In response, 29 hr after the breaching, the Army proceeded to blow up the West levee in four places and the Mar Argentino levee in 2 places (see Figure 3.1), to release part of the huge amount of water trapped inside the city. The reported difference of 2.48 m was numerically reached 30 hr after assuming the sudden breaching (Figure 3.10). Part of this phase lag can be attributed to the misrepresentation in the model of culverts and bridges of the railroad levees and some other waterways existing within the urban area that could have facilitated the water spreading along west Santa Fe. The constant value of the simulated water elevations at INALI, and point '*a*' as well, depicted in Figure 3.10, reflects the time-independent boundary conditions imposed further downstream. The model was calibrated to match the observed values of INALI stage at the end of the simulation. It can be concluded that, in spite of the slow time variation of the flood levels, the numerical results obtained within the bounds of the hypotheses are in good

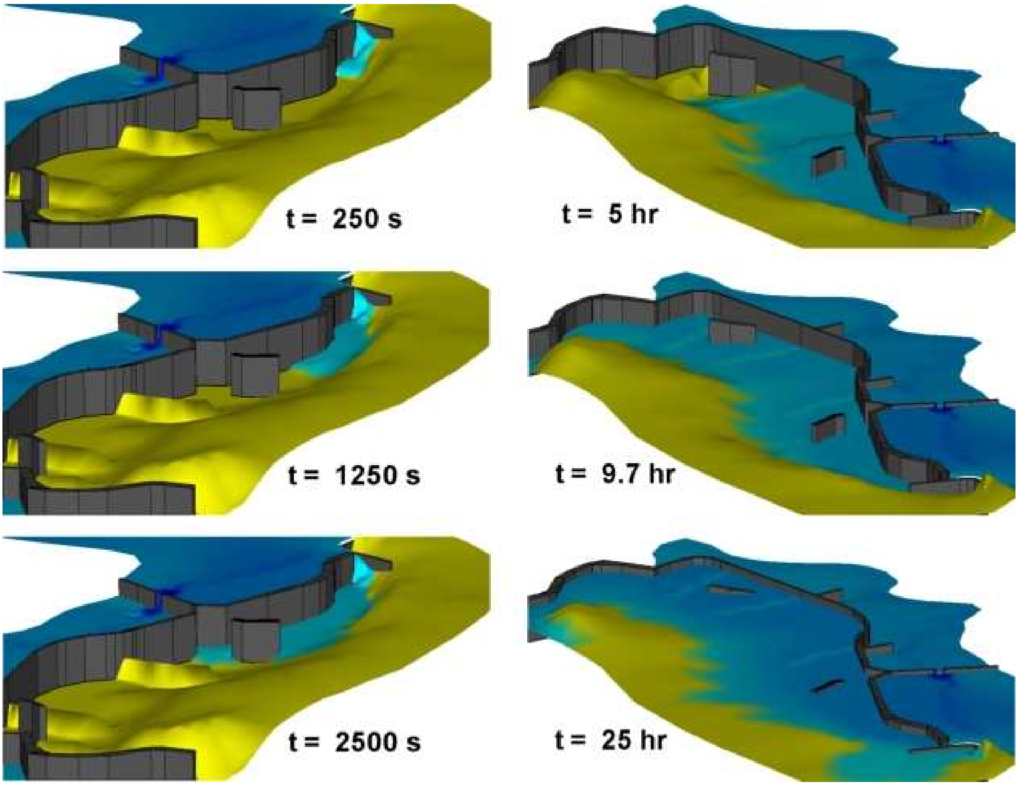

Figure 3.9: 3D projection of the flooding of west Santa Fe at different times. Left: Views from the southeast, Right: Views from the notheast, marked V_{SE} and V_{NE} in Figure 3.10, respectively.

agreement with the observed values.

Two stages are clearly identified in Figure 3.10. The first stage is that of propagation, where the water depth remains more or less uniform while the wave front moves forward relatively fast. The second stage is that of a reservoir filling as characterized by water levels just moving upward.

3.3.1 Sensitivity Analysis

Without loss of generality, the model response for some given input data at $t = t_m = m\Delta t$, $m = 0, 1, ...$, and for some set of parameter values $\mathbf{a}$, can be represented by the vector $\mathbf{y}(u, v, \delta h; \mathbf{a})$, solution of the system of algebraic equation produced by the finite element discretization method [68]. Therefore, for a given discretization, the vector $\mathbf{y}(t; \mathbf{a})$ represents the vector of unknown nodal values, from which a dependent quantity such as the inflow rate to the city through the breach can be computed. Then, the vector $\mathbf{a} = (a_1, a_2, ..., a_k)$ represents the parametric space embedded into the mathematical model (i.e., $a_1 = \mathrm{C_F}$, $a_2 = \nu_t$, $a_3 = Q_{ups}$, which is the upstream boundary condition, and

Param. change	**Model change** $\lvert\delta q\rvert$	**Sens. coeff.** θ
$\lvert\delta n\rvert = 20.0\,\%$	$6.7\,\%$	0.34
$\lvert\delta Q_{ups}\rvert = 5.3\,\%$	$4.6\,\%$	0.87

Table 3.3: Sensitivity coefficients in response to changes in the input parameter values.

so on [21]). It follows that a precise measure of the model sensitivity can be obtained by considering the changes in model responses with respect to the base (or calibrated) state due to changes (or departure) from the calibrated value a_k^o of its k^{th} parameter a_k. Thus, denoting the base state with a zero superscript, and upon linearizing the model response function about the base state, a change $\Delta\mathbf{a}$ in the calibrated value of the parameter $\mathbf{a}_o$ produces a change in the model output given by $\Delta\mathbf{y} \simeq (\mathbf{a} - \mathbf{a}^o) \cdot \partial\mathbf{y}/\partial\mathbf{a}|_o$. The entries of the Jacobian matrix are known as the sensitivity coefficients or condition numbers, $\theta_{ij} = \partial y_i(t;\mathbf{a}^o)/\partial a_j$ [128]. Taking the discharge q entering the city as the model output of paramount interest, the sensitivity coefficient can be written in terms of the absolute value of the relative error $\theta(a_k^o) \simeq |\delta q| \,/\, |\delta a_k|$, where $|\delta q| = |\Delta q/q^o|$ and $|\delta a_k| = |\Delta a_k/a_k^o|$. The model is said to be sensitive, if $\theta > 1$, particularly if θ is large, neutral if $\theta = 1$, or robust if $\theta < 1$. The uncertainty of the model output attributed to the inherent uncertainty with regard to the precise value of a_k^o grows, remains bounded, or attenuates, respectively .

Figure 3.8 shows the effects of globally increasing the calibrated value of the roughness coefficient by 20% and the inflow boundary condition by 5.3%. For this analysis, the adopted base state corresponded to $n^o = 0.025$ and $Q_{ups}^o = 3,600$ m^3/s. The resulting sensitivity coefficients are included in Table 3.3, where $q_{\max}$ (i.e., the maximum discharge coming in through the breach) was chosen for estimating the change in model response. Note that $\theta < 1$ in both cases.

3.4 Conclusions

Slowly rising waters typically characterize the Salado River floods, whereas the failure of the flood-protection work in April 2003 forced people to confront a sudden increase in water levels in a matter of a few hours. This transformation of the river behaviour is well captured in Figure 3.10, where the evolution of the recorded water levels within the floodplain outside the city at the flood peak confirms not only the validity of the hypothesis (v) used to set up the mathematical model, but also is in sharp contrast with the sudden increase of water depths inside the city. Still, the simulated levels are well within the bounds of observed stages. The simulated inflow rate through the gap, $\simeq 540$ m^3/s, compares fairly well with the estimated value of 600 m^3/s obtained by tracking floats. Additionally, the simulation shows that the catastrophic flooding of west Santa Fe City occurred in two stages: the wave front propagation stage, and the fateful reservoir-filling stage. Consequently, a tool like TELEMAC-2D could have been used during the design stage of the flood-protection work to assess the risk associated with the failure of the non-engineered levee used to close the gap left between the properly designed levee and higher lands nearby.

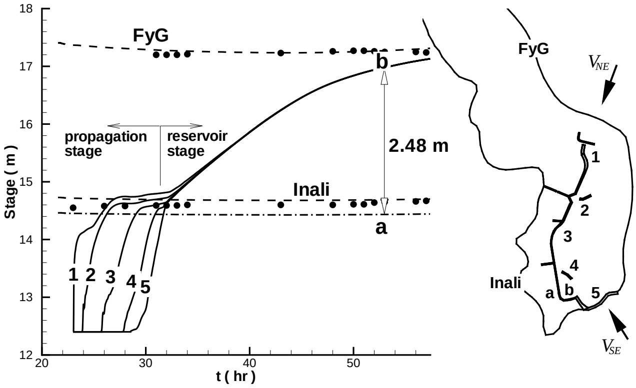

Figure 3.10: Left: Numerical results of the evolution of the water elevation at different locations inside the city (solid lines); numerical results of the evolution of the water elevation at FyG and INALI (dashed lines); stage readings (bullets). Right: Location of selected points within modeling boundaries whose water levels time evolution are shown on the left. V_{NE} and V_{SE} are the viewpoints of the 3D projections of Figure 3.9. FyG stands for Furlong and Gorriti streets.

There are many well documented issues regarding levees and earth dam breaches that could be considered in order to mitigate situations like the sudden flood experienced by one third of the population of Santa Fe City, Argentina. These issues range from the need for a river forecasting system to the need to enforce the State law prohibiting the occupation of flood-prone lowlands. Nevertheless, the authors believe that the main factor behind the catastrophe was cumulative management errors made over the years, which in turn magnified the consequences of an extreme rainfall event.

There are indications that a similar extreme flood event occurred in 1914. An ongoing research program to reconstruct it is underway based upon the historical accounts and archives of the French company that once operated the railroad network throughout the State. However, the only available record data indicates that the 2003 flood was triggered by a 100-year storm over a completed saturated basin [27]. This rainfall caused a flood with a return period estimated above 250 years [71]. In spite of the flood wave severity running down the Salado River, no portion of the levee around Santa Fe that was built to engineering standards failed. Moreover, no portion of the engineered West levee was overtopped with the exception of the lateral weir formed where the railroad crossed the protection structure, rapidly blocked with sandbags by neighbors and State workers.

Among the chain of miss-management decisions that have contributed to the risk of flooding of west Santa Fe City, as explicitly or implicitly mentioned in this work, are: **1**) the freeway bridge was rebuilt with the same span, 155m, in spite of being washed away during the big flood of 1973. The State never decided to increase its span, ignoring technical studies indicating the urgency to do so [59]. Currently, the bridge is being rebuilt with a span of 550 m, **2**) the West levee was constructed on the floodplain itself, diminishing the conveyance capacity of the river in periods of high waters by approximately a factor of 2, from its original average width of 2000 m to the current 1000 – 1200 m, **3**) the provisional closure of the West levee was located near an acute turn of the river (Figure 3.6), where the stream's stronger erosive capacity due to recirculation and turbulence related to flow deceleration could have been anticipated, **4**) the West levee was terminated just few meters before reaching higher lands, which serve as a natural levee constructed by the river over geologic time (Figure 3.2). A continuation of the properly designed levee for others 100 m or nearly so would have diminished the inflow rate to the city by a factor of approximately ten (i.e., about the ratio of incoming overland flow to incoming discharge through the gap (Figure 3.4)). Today, the third stage of the West levee to close the protective ring for the city is under construction, **5**) the State agencies in charge of West levee maintenance and related aspects showed a total lack of coordination. Whereas the State Highway Administration held responsibility for the West levee maintenance, and the State Water Resources Authorities were responsible for issuing flood warnings, no one was assigned the responsibility of reinforcing the non-engineering levee during floods. This lack of coordination could be attributed in part to the success of the non-engineered portion of the flood protection levee during the big flood of 1998 (Table 3.1), and **6**) specially designed devices or gates, to release excess water trapped inside the city in case of a levee breach were not available. The West levee had to be blown up in four places and the city highway belt at two other points. Those sites had to be reconstructed afterwards at a considerable cost.

Finally, the 20 million dollar new Children Hospital was supposed to be built on lands with zero risk of flooding with the assistance of a World Bank loan. A close up look of the sudden end of the West levee by a team of experts could have recognized the high likelihood of failure of the non-engineered levee in case of extreme floods, and helped to put in the public eye the lack of any contingency plan to reinforce the gap during the emergency, among other deficiencies.

Acknowledgments: This work was made possible thanks to the financial support of the National Agency for Promoting Science and Technology (ANPCyT) through the research grant number PID74, and the National Institute of Scientific and Technological Research (CONICET) through a PIP98-616 research grant. Their support is gratefully acknowledged. The authors also want to thank Dr. Laurel Lacher for her thoughtful comments that helped to improve the first draft of the paper.

Chapter 4

Space discontinuous Galerkin method for shallow water equations

In this chapter, a second order space discontinuous Galerkin (DG) method is presented for the numerical solution of inviscid shallow water flows over varying bottom topography. Novel in the implementation is the use of HLLC and kinetic numerical fluxes[1] in combination with a dissipation operator, applied only locally around discontinuities to limit spurious numerical oscillations. Numerical solutions over (non-)uniform meshes are verified against exact solutions; the numerical error in the L_2-norm and the convergence of the solution are computed. Bore-vortex interactions are studied analytically and numerically to validate the model; these include bores as "breaking waves" in a channel and a bore travelling over a conical and Gaussian hump. In these complex numerical test cases, we correctly predict the generation of potential vorticity by non-uniform bores. Finally, we successfully validate the numerical model against measurements of steady oblique hydraulic jumps in a channel with a contraction. In the latter case, the kinetic flux is shown to be more robust[2].

4.1 Introduction

Many river and estuarine flows are three-dimensional (3D), highly variable in time and well-described by the conservation laws of mass and momentum without the need to resort to the more complex situation of a density-stratified fluid. Furthermore, it is often sufficient to consider a restricted form of the Euler equations for an incompressible, homogeneous fluid, namely its hydrostatic, depth-averaged form, which is 2D in the horizontal plane [25]. The resulting, so-called shallow water equations (SWE) are often

---

[1] HLLC stands for the Harten, Lax, and Van Leer or HLL flux extended to deal with Contact waves, whence the abbreviation HLLC.

[2] This chapter has been published in *Advances in Water Resources*, **30**(4), 2007.

used as leading order model for river and shallow lake hydrodynamics, floodplain flows, coastal circulation as well as long wave run-up, among other cases of engineering and scientific interest.

Several numerical algorithms have been developed over the years to solve the SWE approximately with finite difference, finite volume and finite element methods. Early numerical experiments showed, however, that when the discrete finite element problem is formulated by approximating the depth-averaged velocity $\mathbf{u}$ and the water depth h in the SWE with an inappropriate choice of interpolation functions, the solution does not converge as the mesh is refined. In some instances, so-called "checker-board modes" arise in such a way that large oscillations enter into the computed solution [120]. The use of non-staggered grids in a finite difference setting or the straightforward use of equal-order interpolation spaces in a finite element formulation thus often lead to spurious modes. These modes can be suppressed through the use of staggered grids [25], variables suited to potential flow, or with mixed interpolation spaces that satisfy a consistency condition [120]. The other successful techniques in removing spurious oscillation modes from the solution to the SWE that received considerable attention in recent years are the quasi–bubble approximation and the Generalized Wave Continuity Equation method (GWCE)[67]. The GWCE manipulates the primitive form of the SWE prior to its approximation within the finite element framework, and possesses a monotonic dispersion relationship that does not inherit a second artificial high wave number associated with spurious modes [114]. On the other hand, the quasi–bubble approach adds velocity nodes at the centre of the linear space used to approximate the water depth. Nevertheless, a numerical scheme based on equal order approximations procedure is considered to be more efficient from an implementation point of view [98], [103], [124]. Such a scheme is considered in this paper.

In the last few years, the discontinuous Galerkin (DG) method merged ideas from high-resolution finite difference and finite volume schemes for solving nonlinear hyperbolic systems within a finite element framework [11]. In the DG formulation, locally continuous basis and trial functions are introduced, which are globally discontinuous, within each element. Added advantages of DG finite-element methods are such that it is relatively easy [7]: (i) to improve the order of accuracy, thus allowing efficient p-adaptivity; (ii) to refine the grid locally, without taking into account the continuity restrictions typical of conforming finite element methods, thus allowing efficient h-adaptivity; and, (iii) to perform parallel computations [73], since the method is extremely local in data communication. However, the overall formulation involves more degrees of freedom in comparison with finite volume and finite difference methods. For more details and extensions to DG methods with moving boundaries in compressible and shallow water flows, we also refer to Cockburn and Shu [8], Van der Vegt and Van der Ven [138], Bokhove [99] and Bokhove *et al.* [101], and references therein.

This chapter is concerned with the design of a DG finite-element approximation for inviscid SWE. Novel in this work are: I) the use of numerical fluxes in combination with a dissipation operator, applied only locally around discontinuities to limit spurious numerical oscillations; II) the derivation and application of a kinetic numerical flux as alternative to existent numerical fluxes such as the HLLC numerical flux; III) the study of the generation of potential vorticity (PV) anomalies due to bore-vortex interactions in shallow water flows; and, IV) a validation of the numerical model against laboratory data of oblique hydraulic jumps for flow in a flume with a contraction. Bores in shallow water flows are discontinuities in the water depth and akin to shocks, or discontinuities in the density, in gas dynamics. In contrast to flow gas dynamics, energy is dissipated in the bores and hydraulic jumps in the SWE, while mass and (locally) momentum are conserved across such discontinuities. The original shallow water model for smooth flows is therefore extended to include these bores, where energy is dissipated such that multivalued solutions only occur as jumps. In two horizontal dimensions these jumps occur along (time dependent) line discontinuities, and in one dimension at isolated (time dependent) points. These simulations of bore-vortex interaction form demanding test cases, especially for the numerical dissipation around bores, which is unfortunately less well-known in the CFD community. The generation of PV by bores has a counterpart in compressible flow as the generation of Ertel's PV and entropy by shocks, implying that our bore-vortex tests have wider applicability. Furthermore, our numerical verification confirms the stability and efficiency of the DG method.

We thus consider a formulation of the SWE properly allowing for hydraulic jumps and bores as a simple (asymptotic) model of wave breaking. Consequently, we do not use a potential flow formulation, which is more stable but only valid in wave propagation outside regions with shoaling and wave breaking.

The outline of the chapter is as follows. We introduce the SWE in Section 4.2 in dimensional and non-dimensional form, and provide a simplified exposition of potential vorticity generation by bores. The DG spatial discretization is presented in Section 4.3 for the SWE, including a presentation of HLLC and kinetic numerical fluxes. In Section 4.4, the numerical scheme is verified by comparing simulations over (non-)uniform grids with exact one-dimensional solutions. The model is validated by analyzing bore-vortex interactions in a channel and over conical and Gaussian topography, and against laboratory measurements of oblique hydraulic jumps in Section 4.5. Conclusions are drawn in Section 4.6.

4.2 Governing Equations

The SWE in conservative form read (see, e.g., [64])

$$\begin{aligned} \partial_{t^*} h^* + \partial_{x^*}(h^* u^*) + \partial_{y^*}(h^* v^*) &= 0, \\ \partial_{t^*}(h^* u^*) + \partial_{x^*}(h^* u^{*2} + g^* h^{*2}/2) + \partial_{y^*}(h^* u^* v^*) &= - g^* h^* \partial_{x^*} h_b^*, \\ \partial_{t^*}(h^* v^*) + \partial_{x^*}(h^* u^* v^*) + \partial_{y^*}(h^* v^{*2} + g^* h^{*2}/2) &= - g^* h^* \partial_{y^*} h_b^*, \end{aligned} \tag{4.2.1}$$

where partial derivatives are denoted by $\partial_{t^*} = \partial/\partial t^*$ and so forth; $\mathbf{u}^*(\mathbf{x}^*, t^*) = (u^*(\mathbf{x}^*, t^*), v^*(\mathbf{x}^*, t^*))^T$ is the depth-averaged velocity as function of horizontal coordinates $\mathbf{x}^* = (x^*, y^*)^T$ and time t^* (with $(\cdot)^T$ the transpose); and the free surface resides at $z^* = h^* + h_b^*$ with $h^*(\mathbf{x}^*, t^*)$ the total water depth and $h_b^*(\mathbf{x}^*)$ the elevation of the bottom topography above datum, both measured along the vertical coordinate, z^*, and aligned in the direction of the acceleration of gravity of magnitude g^*.

It is convenient to treat the SWE in non-dimensional form for computational reasons and to clarify the coupling of the flow to other physics phenomena, such as erosion and transport of sediments over an erodible bed, a process that introduces a sediment transport time scale much smaller than the flow time scale (see, e.g., Hall [106]). We therefore introduce the dimensionless variables

$$\mathbf{x} = \mathbf{x}^*/l_0^*, \quad t = t^*/t_0^*, \quad h = h^*/h_0^*, \quad h_b = h_b^*/h_0^* \quad \text{and} \quad \mathbf{u} = \mathbf{u}^*/u_0^*, \tag{4.2.2}$$

where l_0^*, t_0^*, h_0^* and u_0^* are suitable, characteristic scales for the length of the fluid motion (usually a reference value of the channel width), time response, water depth and flow velocity, respectively. With (4.2.2), the system (4.2.1) reduces to a non-dimensional form, concisely written in index notation as

$$\partial_t U_i + \partial_j F_{ij}(\mathbf{U}) = S_i \quad \text{in the flow domain } \Omega \tag{4.2.3}$$

for $i = 1, 2, 3$ and $(\partial_x, \partial_y)^T = (\partial_1, \partial_2)^T$ with $j = 1, 2$. Here, summation over repeated indices is understood. In (4.2.3), $\mathbf{U} = (h, hu, hv)^T$ is the vector of the conserved quantities, and

$$F(\mathbf{U}) = \begin{pmatrix} uh & vh \\ u^2h + \mathsf{F}^{-2}h^2/2 & vuh \\ uvh & v^2h + \mathsf{F}^{-2}h^2/2 \end{pmatrix} \text{and}\, S = \begin{pmatrix} 0 \\ -\mathsf{F}^{-2}h\partial_x h_b \\ -\mathsf{F}^{-2}h\partial_y h_b \end{pmatrix}, \tag{4.2.4}$$

are flux and “source” terms, respectively. The Froude number $\mathsf{F} = u_0^*/\sqrt{g^*\, h_0^*}$ is the ratio between the flow velocity and surface gravity-wave speed. We emphasize that the variables $(h, h\,u, h\,v)^T$ are used to properly model bores and hydraulic jumps as discontinuities in a simple model of breaking waves, cf. the classical results in Lamb and Whitham [62, 54], summarized shortly. The numerical model presented later will thus include the physical energy dissipation across these jumps: this dissipation should be contrasted with any (much smaller) numerical dissipation in the numerical scheme. The system (4.2.3) and (4.2.4) is completed with initial conditions $\mathbf{U}(\mathbf{x}, 0)$, boundary conditions such as in- and outflow, and/or slip flow along solid walls. The latter are expressed as $\mathbf{U} = \mathbf{U}^b$ at the boundary $\partial\Omega$.

4.2.1 Potential vorticity

The vertical component of the vorticity, $\Lambda = \partial_x v - \partial_y u$, is conserved for smooth flows ([64]),

$$\partial_t \Lambda + \boldsymbol{\nabla} \cdot (\mathbf{u}\,\Lambda) = 0 \tag{4.2.5}$$

with spatial gradient operator $\boldsymbol{\nabla} = (\partial_x, \partial_y)^T$, which follows readily from (4.2.1), or (4.2.3) and (4.2.4). By combining (4.2.5) with the mass equation, the PV $\Pi = \Lambda/h$ is found to be a materially conserved quantity ([64]),

$$\partial_t \Pi + (\mathbf{u} \cdot \boldsymbol{\nabla})\Pi = 0. \tag{4.2.6}$$

Bores and hydraulic jumps are discontinuities in the flow variables of the SWE, where energy is dissipated but mass and (local) momentum are conserved. In two dimensions these discontinuities occur along lines, and in one dimension at points, thus limiting multivalued solutions along lines and at points only. For a curvilinear bore we introduce a local coordinate system (η, τ) with η in the bore direction and τ the direction along the bore, in the usual orientation. In the present configuration we take $h_2 > h_1$ and $[h] = h_1 - h_2$ with h_2 lying in the region where the bore has passed. The energy dissipation $E_D = B_1 - B_2$, the difference between the Bernoulli function B_1 before and B_2 after passing of the bore with $B = (u-c)^2/2 + \mathsf{F}^{-2}(h + h_b)$ and c the speed of the bore, is given by ([62, 54])

$$E_D = \mathsf{F}^{-2}\,(h_2 - h_1)^3/(4\,h_1\,h_2). \tag{4.2.7}$$

Note that since $h_2 > h_1$ dissipation E_D is indeed positive such that energy is lost in the bore. Pratt [87] and Peregrine [35] show then that, in the presence of such discontinuities, the newly obtained PV, Π_2, is

$$\Pi_2 - \Pi_1 = -\sqrt{\frac{2}{\mathsf{F}^{-2}\,h_1\,h_2\,(h_1 + h_2)}}\,\frac{\partial E_D}{\partial \tau}. \tag{4.2.8}$$

Bühler [102] shows that only PV anomalies can be generated by bores, such that the total PV remains the same in the absence of other sources or sinks of PV than the bores and hydraulic jumps.

4.3 Space Discontinuous Galerkin Method

4.3.1 Space elements and tessellation

The flow domain $\Omega \in \mathbb{R}^2$ is a bounded area which in turn is partitioned into N_{el} elements K_k. It has a fixed boundary $\partial\Omega \in \mathbb{R}$. The tessellation of the domain Ω is defined as

$$\mathcal{T}_h = \left\{ K_\mathsf{k} | \bigcup_{\mathsf{k}=1}^{N_{el}} \bar{K}_\mathsf{k} = \bar{\Omega}_\mathsf{h} \text{ and } K_\mathsf{k} \cap K_{\mathsf{k}'} = 0 \text{ if } \mathsf{k} \neq \mathsf{k}', 1 \leq \mathsf{k}, \mathsf{k}' \leq N_{el} \right\}, \tag{4.3.1}$$

such that the computational domain $\Omega_\mathsf{h} \to \Omega$ as $\mathsf{h} \to 0$, with h the magnitude of the smallest radius of the largest circle completely containing element $K_\mathsf{k} \in \mathcal{T}_h$, and $\bar{K}_\mathsf{k}$ the closure of K_k (and likewise for $\bar{\Omega}$). Each element K_k can be transformed into a reference element $\hat{K}$ with the mapping

$$F_K : \hat{K} \mapsto K_\mathsf{k} : \bar{\xi} \mapsto \mathbf{x} := \sum_j \mathbf{x}_j\,\chi_j(\bar{\xi}), \tag{4.3.2}$$

where $\bar{\xi} = (\xi_1, \xi_2)$ are the reference coordinates, $\mathbf{x}_j$ are the coordinates of the local nodes $j = 1, \ldots, N_{l,\mathsf{k}}$, and $\chi_j(\bar{\xi})$ the standard shape functions used in finite elements. For quadrilateral elements $N_{l,\mathsf{k}} = 4$ and for triangular elements $N_{l,\mathsf{k}} = 3$. In general, the element boundary ∂K_k is connected through faces $\mathcal{S}$ either to its neighboring elements or to the boundary of the domain. The set of all faces in $\Omega \cup \partial\Omega$ is denoted by Γ. The set of all interior faces in Ω is denoted by Γ_{int} and the set of all boundary faces on $\partial\Omega$ is denoted by Γ_{bou}.

4.3.2 Function spaces

The finite element broken space is defined as

$$\mathcal{V}_{\mathsf{h}}^d := \{\mathbf{V}_{\mathsf{h}} | \mathbf{V}_{\mathsf{h}}|_K \in (P^1(K))^d\}, \tag{4.3.3}$$

where P^1 is the space of linear polynomials, $d = \dim(\mathbf{V}_{\mathsf{h}})$ and $\mathbf{V}_{\mathsf{h}}$ the polynomial approximation defined as $\mathbf{V}_{\mathsf{h}} := \sum_m \hat{\mathbf{V}}_m(t)\psi_m(\mathbf{x})$ with $\hat{\mathbf{V}}_m$ the expansion coefficients and ψ_m the polynomial basis functions. In the reference element $\hat{K}$, the set of polynomials is defined as

$$\{\hat{\phi}_0, \hat{\phi}_1, \hat{\phi}_2, \hat{\phi}_3\} := \{1, \xi_1, \xi_2, \xi_1 \xi_2\}, \tag{4.3.4}$$

where the $\hat{\phi}_m(\bar{\xi})$'s for $m = 0, 1, 2, 3$ are the basis functions on a quadrilateral element. On triangular elements, we use $\hat{\phi}_m(\bar{\xi})$ for $m = 0, 1, 2$. If the topography $h_b(\mathbf{x})$ is discretized continuously, the extra function $\hat{\phi}_3$ is required on quadrilateral elements. It then enforces rest flow to be preserved numerically, see section 4.4.3. The local basis functions in $\hat{K}$ can be related to the basis functions in K_{k} by $\hat{\phi}_m(\bar{\xi}) = \hat{\phi}_m(F_K^{-1}(\bar{\xi})) = \phi_m(\mathbf{x})$. We split the approximations of the conserved quantities in the space element K_{k} into mean and fluctuating parts. The basis functions are then redefined as

$$\psi_m(\mathbf{x}, t) = \begin{cases} 1 & \text{if} \quad m = 0 \\ \phi_m(\mathbf{x}) - c_m & \text{otherwise} \end{cases} \tag{4.3.5}$$

with $c_m = \frac{1}{|K_{\mathsf{k}}|} \int_{K_{\mathsf{k}}} \phi_m(\mathbf{x})\,\mathrm{d}\mathbf{x}$. Here, $|K_{\mathsf{k}}| = \int_{K_{\mathsf{k}}} dK$ is the area of the element K_{k}. If $\mathbf{x}$ is a point on a face $\mathcal{S}$ in Γ and $\mathbf{n}_K$ is the outward unit normal vector of the boundary ∂K_{k}, then the trace of the function $\mathbf{V}_{\mathsf{h}}$ on the element interior boundary ∂K_{k}, relative to K_{k}, is defined as $\mathbf{V}_{\mathsf{h}}(\mathbf{x})|_{\partial K_{\mathsf{k}}} = \mathbf{V}^- := \lim_{\epsilon \uparrow 0} \mathbf{V}_{\mathsf{h}}(\mathbf{x} - \epsilon \mathbf{n}_K)$. The traces of the functions on each face relative to the neighboring element are, in general, discontinuous since $\mathbf{V}_{\mathsf{h}}(\mathbf{x}) \in \mathcal{V}_{\mathsf{h}}^d$.

4.3.3 Weak formulation

The space discontinuous Galerkin weak formulation is obtained by multiplying (4.2.3) by a test function $\mathbf{W}_{\mathsf{h}}$ in the finite element space $\mathcal{V}_{\mathsf{h}}^d$, integrating over the space element K_{k}, and replacing the exact solution $\mathbf{U}$ by its approximation $\mathbf{U}_{\mathsf{h}} \in \mathcal{V}_{\mathsf{h}}^d$

$$\int_{K_{\mathsf{k}}} W_{\mathsf{h}i} \partial_t U_{\mathsf{h}i}\,\mathrm{d}K + \int_{K_{\mathsf{k}}} W_{\mathsf{h}i} \partial_j F_{ij}(\mathbf{U}_{\mathsf{h}})\,\mathrm{d}K - \int_{K_{\mathsf{k}}} W_{\mathsf{h}i} S_i\,\mathrm{d}K = 0. \tag{4.3.6}$$

Applying Gauss's theorem to the flux term of (4.3.6) and after summing over all elements, the weak formulation is: *find a* $\mathbf{U}_{\mathsf{h}} \in \mathcal{V}_{\mathsf{h}}^d$ *such that for all* $\mathbf{W}_{\mathsf{h}} \in \mathcal{V}_{\mathsf{h}}^d$

$$\sum_{K_{\mathsf{k}}} \Big\{ \int_{K_{\mathsf{k}}} W_{\mathsf{h}i} \partial_t U_{\mathsf{h}i}\,\mathrm{d}K + \int_{\partial K_{\mathsf{k}}} n_{Kj} W_{\mathsf{h}i}^- F_{ij}{}^-\,\mathrm{d}\Gamma - \int_{K_{\mathsf{k}}} \partial_j W_{\mathsf{h}i} F_{ij}(\mathbf{U}_{\mathsf{h}})\,\mathrm{d}K - \int_{K_{\mathsf{k}}} W_{\mathsf{h}i} S_i\,\mathrm{d}K \Big\} = 0 \tag{4.3.7}$$

is satisfied, where $W_{\mathsf{h}i}^-$ and $U_{\mathsf{h}i}^-$ are the traces of $W_{\mathsf{h}i}$ and $U_{\mathsf{h}i}$ respectively; $F_{ij}^- = F_{ij}(\mathbf{U}_{\mathsf{h}}^-)$; and $\mathrm{d}\Gamma$ is an infinitesimal boundary segment. The communication of mass and momentum between neighboring elements occurs through the element faces.

In the weak formulation (4.3.6), there is thus an ambiguity because $U_{\mathsf{h}i}$ is discontinuous, implying that the flux F at a face is discontinuous. Considering the integrals over the element boundaries with a counterclockwise ordering such that n^l_{Kj}, F^l_{ij}, and $W^l_{\mathsf{h}i}$ are the outward normal, the flux, and the test function for a left element, and n^r_{Kj}, F^r_{ij}, and $W^r_{\mathsf{h}i}$ the corresponding quantities for the right element, we find

$$\sum_{K_\mathsf{k}} \int_{\partial K_\mathsf{k}} n_{Kj} W^-_{\mathsf{h}i} F_{ij}{}^- \, \mathrm{d}\Gamma = \sum_{\mathcal{S}} \int_{\mathcal{S}} (n^l_{Kj} W^l_{\mathsf{h}i} F^l_{ij} + n^r_{Kj} W^r_{\mathsf{h}i} F^r_{ij}) \, \mathrm{d}\Gamma =$$

$$\sum_{\mathcal{S}} \int_{\mathcal{S}} (\alpha \mathcal{F}^l_{ij} + \beta F^r_{ij})(n^l_{Kj} W^l_{\mathsf{h}i} + n^r_{Kj} W^r_{\mathsf{h}i}) + (n^l_{Kj} F^l_{ij} + n^r_{Kj} F^r_{ij})(\alpha W^l_{\mathsf{h}i} + \beta W^r_{\mathsf{h}i}) \, \mathrm{d}\Gamma$$

with $\alpha + \beta = 1$ and $\alpha, \beta \geq 0$. If the flux is taken to be conservative such that

$$\int_{\mathcal{S}} n^l_{Kj} W^l_{\mathsf{h}i} F^l_{ij} \mathrm{d}\Gamma = - \int_{\mathcal{S}} n^r_{Kj} W^r_{\mathsf{h}i} F^r_{ij} \mathrm{d}\Gamma \tag{4.3.8}$$

and $n^l_{Kj} = -n^r_{Kj}$ at a face, then

$$\sum_{K_\mathsf{k}} \int_{\partial K_\mathsf{k}} n_{Kj} W^-_{\mathsf{h}i} F_{ij}{}^- \, \mathrm{d}\Gamma = \sum_{\mathcal{S}} \int_{\mathcal{S}} n^l_{Kj} (W^l_{\mathsf{h}i} - W^r_{\mathsf{h}i})(\alpha F^l_{ij} + \beta F^r_{ij}) \mathrm{d}\Gamma. \tag{4.3.9}$$

The flux $(\alpha F^l_{ij} + \beta F^r_{ij})$ in (4.3.9) is replaced by a numerical flux $\tilde{F}_{ij}(\mathbf{U}^l, \mathbf{U}^r, \mathbf{n}_K)$, which depends on the discontinuous trace values $\mathbf{U}^l$ and $\mathbf{U}^r$ directly adjacent to each interface. The boundary condition $\mathbf{U}^r = \mathbf{U}^b$ is applied on faces belonging to a boundary $\mathcal{S} \in \Gamma_{bou}$. Finally, the weak formulation for the space DG method for each space element now becomes: *find a* $\mathbf{U}_\mathsf{h} \in \mathcal{V}^d_\mathsf{h}$ *such that for all* $\mathbf{W}_\mathsf{h} \in \mathcal{V}^d_\mathsf{h}$

$$\begin{aligned} \sum_{\mathcal{S}} \left\{ \int_{\mathcal{S}} n_{Kj} \tilde{F}_{ij}(\mathbf{U}^l, \mathbf{U}^r, \mathbf{n}_K) \, (W^l_{\mathsf{h}i} - W^r_{\mathsf{h}i}) \mathrm{d}\Gamma \right\} + \\ \sum_{K} \left\{ \int_{K_\mathsf{k}} W_{\mathsf{h}i} \partial_t U_{\mathsf{h}i} \, \mathrm{d}K - \int_{K_\mathsf{k}} \partial_j W_{\mathsf{h}i} F_{ij}(\mathbf{U}_\mathsf{h}) \, \mathrm{d}K - \int_{K_\mathsf{k}} W_{\mathsf{h}i} S_i \, \mathrm{d}K \right\} = 0 \end{aligned} \tag{4.3.10}$$

is satisfied. This form is also used in the numerical implementation. Numerically, the element and face integrals are approximated using Gauss quadrature.

4.3.4 Numerical flux

In this work, the HLLC numerical flux of Toro *et al.* [134] and the kinetic numerical flux are used. The HLLC flux is an accurate and efficient approximation to a numerical flux based on a one-dimensional Riemann problem in the direction normal to each face at the relevant quadrature points. It is a modification of the HLL [2] scheme that takes into account the influence of contact waves [105, 134]. On the other hand, the kinetic numerical flux is based on the theory of kinetic schemes for gas dynamics and links Vlasov equations with hydrodynamic equations [15]. The main difference of the kinetic flux with respect to the HLLC flux is the incorporation of the topographic term in the derivation of the approach. Their formulations are given next.

HLLC numerical flux

If we suppose that the element face $\mathcal{S}$, whose unit normal vector $\mathbf{n}_K = (n_{Kx}, n_{Ky})^T$ is oriented is such a way that $\partial_{\hat{x}} = \mathbf{n}_K \cdot \boldsymbol{\nabla}$ defines the derivative normal to the face $\mathcal{S}$, then the normal flux is determined by considering the SWE (i.e., (4.2.3 and (4.2.4) without source terms) along $\mathbf{n}_K$, and the following one-dimensional Riemann problem can be distilled from the SWE

$$\partial_t \mathbf{U} + \partial_{\hat{x}} \hat{\mathbf{F}}(\mathbf{U}) = 0 \tag{4.3.11}$$

with initial constant states $\mathbf{U}^l$ and $\mathbf{U}^r$ left and right of each face, $\hat{\mathbf{F}}(\mathbf{U}) = q\mathbf{U} + \hat{\mathbf{P}}$, $q = \mathbf{n}_K \cdot \mathbf{u}$ the normal velocity, $\mathbf{u} = (u, v)^T$, $\hat{\mathbf{P}} = (0, n_{Kx}P, n_{Ky}P)^T$ the normal pressure, and $P = \mathsf{F}^{-2}h^2/2$ the effective pressure. The HLLC approximation to the normal flux vector $\hat{\mathbf{F}}(\mathbf{U})$ at the cell boundary is proposed next and is based on this Riemann problem.

The HLLC approach for the case of a wet bed assumes that there are four states from left to right, that is $\mathbf{U}^l$, $\mathbf{U}^{*l}$, $\mathbf{U}^{*r}$, $\mathbf{U}^r$, separated by left (l), right (r), and middle (m) transition lines defined by wave speeds s_l, s_r, s_m, respectively (see Figure 4.1):

$$\mathbf{U} = \begin{cases} \mathbf{U}^l & \hat{x}/t < s_l \\ \mathbf{U}^{*l} & s_l < \hat{x}/t < s_m \\ \mathbf{U}^{*r} & s_m < \hat{x}/t < s_r \\ \mathbf{U}^r & \hat{x}/t > s_r \end{cases}, \tag{4.3.12}$$

where $\mathbf{U}^{*l,r}$ are the averaged intermediate states and $\hat{x} = 0$ is chosen to coincide with the relevant face. After integration of (4.3.11) over two control volumes, $DEFC$ and $EABF$ (Figure 4.1) around the element edge for the following four cases (1) $s_l < 0$, $s_r, s_m > 0$, (2) $s_l < 0, s_r > 0$, $s_m \geq 0$, (3) s_l, s_m, $s_r < 0$, and (4) s_r, s_m, $s_r > 0$ see [105, 134], $\hat{\mathbf{F}}$ is computed as the average of the contribution on either side of the face. Using Gauss' theorem in space and time, the HLLC flux is

$$\begin{aligned} \hat{\mathbf{F}}(\mathbf{U}^l, \mathbf{U}^r) = & \frac{1}{2}\big\{\hat{\mathbf{F}}^l + \hat{\mathbf{F}}^r - (|s_l| - |s_m|)\mathbf{U}^{*l} \\ & + (|s_r| - |s_m|)\mathbf{U}^{*r} + |s_l|\mathbf{U}^l - |s_r|\mathbf{U}^r\big\}, \end{aligned} \tag{4.3.13}$$

where $\hat{\mathbf{F}}^{l,r} = \hat{\mathbf{F}}(\mathbf{U}^{l,r})$. From the HLL approximation, an expression for the intermediate state $\mathbf{U}^*$ is obtained [105]

$$\mathbf{U}^* = \big(s_r\mathbf{U}^r - s_l\mathbf{U}^l - (\hat{\mathbf{F}}^r - \hat{\mathbf{F}}^l)\big)/(s_r - s_l). \tag{4.3.14}$$

An expression for speed s_m can be found [105] assuming that

$$s_m = q_l^* = q_r^* = q^*, \tag{4.3.15}$$

where q^* is the average velocity between the left and right waves. From (4.3.14) and the latter expression, (4.3.15) the following wave speed s_m is obtained

$$s_m = q^* = \mathbf{n}_K \cdot \mathbf{u}^* = \frac{P_l - P_r + h_r q_r(s_r - q_r) - h_l q_l(s_l - q_l)}{h_r(s_r - q_r) - h_l(s_l - q_l)}. \tag{4.3.16}$$

By using the Rankine-Hugoniot relations for (4.3.11), the intermediate states U^{*l} and U^{*r} are found to be

$$(s_{l,r} - s_m)U_i^{*l,*r} = (s_{l,r} - q_{l,r})U_i^{l,r} + (\hat{P}_i^{*l,*r} - \hat{P}_i^{l,r}), \tag{4.3.17}$$

where the average intermediate normal pressure $P_i^{*l,*r} = (0, n_{Kx}P^*_{l,r}, n_{Ky}P^*_{l,r})^T$. After some algebraic manipulations of (4.3.17), we find

$$P^* = P^*_{l,r} = h_{l,r}(q_{l,r} - s_{l,r})(q_{l,r} - s_m) + P_{l,r}. \tag{4.3.18}$$

Finally, the wave speeds are estimated based on the left and right moving rarefaction wave speeds

$$s_l = \min(q_l - a_l, q_r - a_r) \qquad \text{and} \qquad s_r = \max(q_l + a_l, q_r + a_r), \tag{4.3.19}$$

respectively, with $a^2 = \partial P/\partial h$. When $s_l > 0$ the flux simplifies to $\hat{\mathbf{F}}^l$, and when $s_r < 0$ to $\hat{\mathbf{F}}^r$, that is, the classic upwind cases. We refer to [105] for more information.

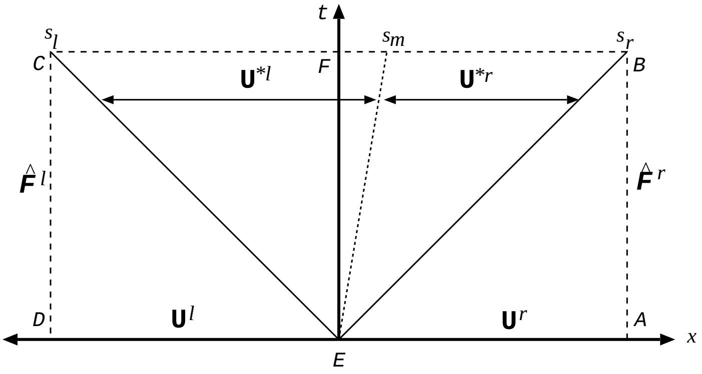

Figure 4.1: A sketch is given of the simplified Riemann fan with its two intermediate states as used in the HLLC flux.

Kinetic numerical flux

Consider the collisionless kinetic or Vlasov equation [115, 100]

$$\partial_t \mathsf{D} + \boldsymbol{\nabla} \cdot (\bar{\zeta}\,\mathsf{D}) - \boldsymbol{\nabla}_\zeta \cdot [(\mathsf{F}^{-2}\,\boldsymbol{\nabla} h_b)\,\mathsf{D}] = 0 \tag{4.3.20}$$

with distribution function $\mathsf{D} = \mathsf{D}(\mathbf{x}, \bar{\zeta}, t)$ a function of horizontal coordinates $\mathbf{x}$, velocity coordinates $\bar{\zeta} = (\zeta_1, \zeta_2)^T$ and time; potential $h_b(\mathbf{x})/\mathsf{F}^2$; and a velocity gradient operator $\boldsymbol{\nabla}_\zeta$. Note that the Vlasov equation is a conservation law linear in D.

Consider a function $\chi : \mathcal{R}^2 \to \mathcal{R}^+$ with the following symmetry properties

$$\chi(\cdot) \geq 0, \quad \chi(\bar{\omega}) = \chi(-\bar{\omega}), \quad \int_{\mathcal{R}} \chi(\bar{\omega})\,\mathrm{d}\bar{\omega} = 1, \quad \int_{\mathcal{R}} \omega_i^2 \chi(\bar{\omega})\,\mathrm{d}\bar{\omega} = 1 \tag{4.3.21}$$

with $\bar{\omega} = (\omega_1, \omega_2)$, $\mathrm{d}\bar{\omega} = \mathrm{d}\omega_1\, \mathrm{d}\omega_2$, and $i = 1, 2$. Hence, $\int_{\mathcal{R}} \omega_i\, \chi(\bar{\omega})\mathrm{d}\bar{\omega} = 0$. The distribution function D is restricted to be in the equilibrium state

$$\mathsf{D} = K(h)\, \chi\left((\bar{\xi} - \mathbf{u})/G(h)\right) \tag{4.3.22}$$

with (Eulerian) fluid velocity $\mathbf{u} = \mathbf{u}(\mathbf{x}, t)$ and pseudo-density $h = h(\mathbf{x}, t)$. We define the functions $K(h)$ and $G(h)$ such that

$$h = K\, G^2 \qquad \text{and} \qquad P(h) = K\, G^4 = h^2/(2\,\mathsf{F}) \tag{4.3.23}$$

with $P(h)$ the effective pressure, a smooth, increasing function of h.

Proposition 4.3.1. *The two-dimensional shallow water equations (4.2.3) and (4.2.4) follow from the kinetic equation of motion (4.3.20) when the distribution function is constrained to (4.3.22) and (4.3.23) for a function $\chi(\cdot)$ in (4.3.22) with symmetry properties (4.3.21).*

Proof: see Appendix B.

Note that (4.3.20) can also be written in the concise form (4.2.3) by taking $U = \mathsf{D}(\mathbf{x}, \bar{\zeta}, t)$, $F = \bar{\zeta}\,\mathsf{D}$, and $S = \boldsymbol{\nabla}_{\zeta} \cdot [(\mathsf{F}^{-2}\, \boldsymbol{\nabla} h_b)\,\mathsf{D}]$.

Weak formulation from kinetic formulation

A discretization of the equations of motion (4.2.3) and (4.2.4) for the $P(h)$–fluid can be formulated from a discretization of the kinetic equation (4.3.20). In this way, one directly obtains a numerical flux. In contrast to the higher-order discontinuous finite-element discretization proposed here, Perthame [14] and Perthame and Simeoni [15] considered a kinetic flux formulation for a first-order finite-volume discretization of the compressible Euler equations and SWE, respectively.

The weak formulation for the kinetic equations of motion (4.3.20) is

$$\begin{aligned} \sum_{K_{\mathsf{k}}} \int_{K_{\mathsf{k}}} w_{\mathsf{h}} \partial_t \mathsf{D}\, \mathrm{d}K + \int_{\partial K_{\mathsf{k}}} (\hat{n}_{\mathsf{k}}^- \cdot \bar{\zeta}) w_{\mathsf{h}}^- \tilde{\mathsf{D}}_{\mathsf{h}}\, \mathrm{d}\Gamma - \\ \int_{K_{\mathsf{k}}} \mathsf{D}_{\mathsf{h}}\, \boldsymbol{\nabla} w_{\mathsf{h}} \cdot \bar{\zeta}\, \mathrm{d}K - \int_{K_{\mathsf{k}}} w_{\mathsf{h}}\, (f\, \bar{\zeta}^{\perp} + \mathsf{F}^{-2}\, \boldsymbol{\nabla} h_b) \cdot \boldsymbol{\nabla}_{\zeta} \mathsf{D}_{\mathsf{h}}\, \mathrm{d}K = 0, \end{aligned} \tag{4.3.24}$$

where we used the upwind flux

$$\tilde{\mathsf{D}} = \mathsf{D}_{\mathsf{k}}^-\, \Theta(\hat{n}_{\mathsf{k}}^- \cdot \bar{\zeta}) + \mathsf{D}_{\mathsf{k}}^+\, \Theta(-\hat{n}_{\mathsf{k}}^- \cdot \bar{\zeta}) \tag{4.3.25}$$

with Heaviside function $\Theta(\cdot)$ (i.e. $\Theta(a) = 0$ for $a < 0$ and $\Theta(a) = 1$ for $a \geq 0$), and traces $\mathsf{D}_{\mathsf{k}}^-$ and $\mathsf{D}_{\mathsf{k}}^+$ of D in- and outside the element along the faces of the element K_{k}. The test function w_{h} is a scalar function since D is a scalar function, in contrast to the test functions introduced in the weak formulation (4.3.6) for the SWE. The DG numerical approximation in space, $\mathbf{x}$, of D is D_{h}.

Multiplying (4.3.24) by $(1, \bar{\zeta})^T$, integrating over $\bar{\zeta}$, and applying the same operations as in the continuous case, yields a numerical discretization of the SWE

$$\begin{aligned} \int_{K_{\mathsf{k}}} w_{\mathsf{h}} \frac{\mathrm{d}U_{\mathsf{h}i}}{\mathrm{d}t}\, \mathrm{d}K + \int_{\partial K_{\mathsf{k}}} w_{\mathsf{h}}^-\, \tilde{F}_{ij}^{kin}\, \mathrm{d}\Gamma - \int_{K_{\mathsf{k}}} \partial_j\, w_{\mathsf{h}}\, F_{ij}(\mathbf{U}_{\mathsf{h}})\, \mathrm{d}K + \\ \int_{K_{\mathsf{k}}} w_{\mathsf{h}}\, h_{\mathsf{h}}\, (0, f\, \mathbf{u}^{\perp} + \mathsf{F}^{-2}\, \boldsymbol{\nabla} h_b)_i^T\, \mathrm{d}K = 0 \end{aligned} \tag{4.3.26}$$

with the numerical kinetic flux vector

$$\tilde{F}^{kin} = \tilde{F}^{\mathrm{out}}(\mathbf{U}^l) + \tilde{F}^{\mathrm{in}}(\mathbf{U}^r) \tag{4.3.27}$$

$$\tilde{F}^{\mathrm{out}}(\mathbf{U}^l) = \int \mathsf{D}^l \, (\hat{n}_{\mathsf{k}}^- \cdot \bar{\zeta}) \, \Theta(\hat{n}_{\mathsf{k}}^- \cdot \bar{\zeta}) \, (1, \bar{\zeta})^T \, \mathrm{d}\bar{\zeta} \tag{4.3.28}$$

$$\tilde{F}^{\mathrm{in}}(\mathbf{U}^r) = \int \mathsf{D}^r \, (\hat{n}_{\mathsf{k}}^- \cdot \bar{\zeta}) \, \Theta(-\hat{n}_{\mathsf{k}}^- \cdot \bar{\zeta}) \, (1, \bar{\zeta})^T \, \mathrm{d}\bar{\zeta}. \tag{4.3.29}$$

For $S = (0, \mathsf{F}^{-2} \, \boldsymbol{\nabla} h_b)^T$, the difference between the weak formulation (4.3.10) with the HLLC numerical flux and (4.3.26) lies in the definition of the numerical flux and the test functions W_{h} and w_{h} Further information about the implementation of the kinetic flux is found in Appendix C.

4.3.5 Stabilization operator and discontinuity detector for DG

Higher-order numerical schemes produce spurious oscillations around discontinuities that can lead to numerical instabilities and to unbounded results in finite time. As pointed out in [119], only schemes that are first-order accurate are able to produce monotonic solutions when discontinuities are present. Such schemes produce too much numerical dissipation, which severely deteriorates the solution quality. Several flux limiting strategies have been developed to cope with spurious oscillations [139]. The approach presented here uses the jump in the polynomial representation of the solution at the element faces in the discontinuous Galerkin discretization, and is based on the approach followed by [138] for a space-time discontinuous Galerkin method. We add the following stabilizing operator to the weak formulation per space element K_{k}:

$$\int_{K_{\mathsf{k}}} \partial_l W_{\mathsf{h}i} \mathcal{D}_{\mathsf{k},lj}(\mathbf{U}_{\mathsf{h}}^l, \mathbf{U}_{\mathsf{h}}^r) \partial_j U_{\mathsf{h}i} dK, \tag{4.3.30}$$

where $\mathbf{U}_{\mathsf{h}}^{l,r}$ is the discontinuous Galerkin solution in neighboring elements and $\mathcal{D}_{\mathsf{k},lj}(\mathbf{U}_{\mathsf{h}}^l, \mathbf{U}_{\mathsf{h}}^r)$ is the dissipation matrix. Instead of flux limiting after each time step, we include it in the weak formulation, which is advantageous for steady state calculations. Since it is desirable to obtain solutions with neither excessive amount of dissipation nor spurious oscillations, a discontinuity detector proposed by Krivodonova *et al.* [84] is implemented for the SWE, defined as

$$\mathcal{I}_{\mathsf{k}} = \frac{\displaystyle\sum_{\mathcal{S} \in \partial K_{\mathsf{k}}} \int_{\mathcal{S}} |h_{\mathsf{h}}^r - h_{\mathsf{h}}^l| \, d\mathcal{S}}{\mathsf{s}_K^{(p+1)/2} |\partial K_{\mathsf{k}}| \max \parallel h_{\mathsf{h}} \parallel}, \tag{4.3.31}$$

where $|\partial K_{\mathsf{k}}|$ is the length of the element boundary, s_K is the cell measure defined as the radius of the largest circumscribed circle in the element K_{k}, p is the order of the polynomial used, $h_{\mathsf{h}}^{l,r}$ is the approximate water depth in adjacent elements, and $\max \parallel \cdot \parallel$ the maximum norm based on local solution maxima at Gauss integration points in the element K_{k}. The solution is smooth if $\mathcal{I}_{\mathsf{k}} > 1$ and the solution is discontinuous if $\mathcal{I}_{\mathsf{k}} < 1$ [84].

Combining the stabilization operator (4.3.30) with the discontinuity detector (4.3.31), and upon introducing the Heaviside step function $\Theta(\mathcal{I}_{\mathsf{k}}-1)$, the weak formulation reduces to: *find a* $\mathbf{U}_{\mathsf{h}} \in \mathcal{V}_{\mathsf{h}}^d$ *such that for all* $\mathbf{W}_{\mathsf{h}} \in \mathcal{V}_{\mathsf{h}}^d$

$$
\begin{aligned}
\sum_{\mathcal{S}} \left\{ \int_{\mathcal{S}} n_{Kj} \tilde{F}_{ij}(\mathbf{U}^l, \mathbf{U}^r, \mathbf{n}_K))(W_{\mathsf{h}i}^l - W_{\mathsf{h}i}^r) \mathrm{d}\Gamma \right\} + \\
\sum_K \Big\{ \int_{K_{\mathsf{k}}} W_{\mathsf{h}i} \partial_t U_{\mathsf{h}i}\, \mathrm{d}K - \int_{K_{\mathsf{k}}} \partial_j W_{\mathsf{h}i} F_{ij}(\mathbf{U}_{\mathsf{h}})\, \mathrm{d}K - \int_{K_{\mathsf{k}}} W_{\mathsf{h}i} S_i - \\
\Theta(\mathcal{I}_{\mathsf{k}} - 1) \int_{K_{\mathsf{k}}} \partial_l W_{\mathsf{h}i} \mathcal{D}_{\mathsf{k},lj}(\mathbf{U}_{\mathsf{h}}^l, \mathbf{U}_{\mathsf{h}}^r) \partial_j U_{\mathsf{h}i} dK \Big\} = 0
\end{aligned}
\tag{4.3.32}
$$

is satisfied.

4.3.6 Stabilization matrix

An artificial viscosity matrix is introduced such that the stabilization operator operates independently in all computational coordinate directions using the relation

$$
\mathcal{D}_{\mathsf{k}}(\mathbf{U}_{\mathsf{h}}^l, \mathbf{U}_{\mathsf{h}}^r) = \mathcal{R}^T \tilde{\mathcal{D}}_{\mathsf{k}}(\mathbf{U}_{\mathsf{h}}^l, \mathbf{U}_{\mathsf{h}}^r) \mathcal{R}, \tag{4.3.33}
$$

where the matrix $\mathcal{R}$ is defined as $\mathcal{R} = 2\mathcal{H}^{-1}\boldsymbol{\nabla} F_K$ and $\tilde{\mathcal{D}}_{\mathsf{k}}(\mathbf{U}_{\mathsf{h}}^l, \mathbf{U}_{\mathsf{h}}^r)$ is the stabilization matrix in reference coordinates. The diagonal matrix $\mathcal{H}$ is introduced to ensure that both $\mathcal{D}_{\mathsf{k}}(\mathbf{U}_{\mathsf{h}}^l, \mathbf{U}_{\mathsf{h}}^r)$ and $\tilde{\mathcal{D}}_{\mathsf{k}}(\mathbf{U}_{\mathsf{h}}^l, \mathbf{U}_{\mathsf{h}}^r)$ have the same mesh dependence as function of c_i, defined as $\mathcal{H} = \mathrm{diag}(c_1, c_2)$, where the c_i's are the leading terms of the expansion of the mapping F_K in the reference coordinates. For quadrilaterals $c_1 = |\mathbf{x}_1 + \mathbf{x}_2 - \mathbf{x}_0 - \mathbf{x}_3|/4$ and $c_2 = |\mathbf{x}_2 + \mathbf{x}_3 - \mathbf{x}_0 - \mathbf{x}_1|/4$. For the evaluation of the coefficients $\tilde{\mathcal{D}}_{\mathsf{k},qq}(\mathbf{U}_{\mathsf{h}}^l, \mathbf{U}_{\mathsf{h}}^r)$ of the stabilization matrix, the artificial viscosity model proposed by Jaffre *et al.* [61] is adopted here

$$
\begin{cases}
\tilde{\mathcal{D}}_{\mathsf{k},qq}(\mathbf{U}_{\mathsf{h}}^l, \mathbf{U}_{\mathsf{h}}^r) = C\, c_K^2 R_{\mathsf{k}}(\mathbf{U}_{\mathsf{h}}^l, \mathbf{U}_{\mathsf{h}}^r) & \text{for } q = 1, 2 \\
0, & \text{otherwise}
\end{cases}
\tag{4.3.34}
$$

with the residual $R_{\mathsf{k}}(\mathbf{U}_{\mathsf{h}}^l, \mathbf{U}_{\mathsf{h}}^r)) = \sum_{\mathcal{S} \in \partial K_{\mathsf{k}}} \frac{1}{c_K} \max \parallel n_{Kj}^l (F_{ij}^l - F_{ij}^r) \parallel$, where $c_K = \sqrt{c_1^2 + c_2^2}$ the scaling factor, $\parallel \cdot \parallel$ is based on the maximum at the local Gauss integration points, and C is a positive constant with values between the range $[0.01; 0.1]$.

4.3.7 Time discretization

The discretized weak formulation arises when the test functions $W_{\mathsf{h}i}$ are alternately chosen as the functions ψ_m. It consists of a system of ordinary differential equations. We use the explicit third order TVD Runge Kutta scheme of [20] to step forward in time. The associated time step constraint has the form $\Delta t = \mathit{CFL}\ \min_{K_{\mathsf{k}}} \big(|K_{\mathsf{k}}| / \max_{K_{\mathsf{k}}} |\mathbf{u} \pm \sqrt{h}/\mathsf{F}| \big)$ with the Courant-Friedrichs-Lewy number $\mathit{CFL} \leq 1$.

$N \times N$	h		hu	
	L_2 error	Order p	L_2 error	Order p
20×20	1.049e-03		5.003e-04	
40×40	2.796e-04	1.90	1.300e-04	1.94
80×80	7.329e-05	1.93	3.297e-05	1.97
160×160	1.888e-05	1.95	8.291e-06	1.99

Table 4.1: The L_2 error of h and hu and convergence rates for Burgers' solution of the SWE on non-uniform meshes are shown for the HLLC flux.

4.4 Verification of the model

The discontinuous Galerkin finite element method has been implemented on a quadrilateral mesh using the C++ programming language. To verify numerical solutions against exact ones, regular as well as irregular meshes are used. The latter are constructed by a restricted, random movement of the internal nodes of a regular grid. The error in the L_2-norm,

$$\Big(\int_{\Omega_{\mathsf{h}}} (\mathbf{U}_{\mathsf{e}} - \mathbf{U}_{\mathsf{h}})^2 \, d\Omega\Big)^{1/2} = \Big(\sum_{K} \int_{K_{\mathsf{h}}} (\mathbf{U}_{\mathsf{e}} - \mathbf{U}_{\mathsf{h}})^2 \, d\Omega\Big)^{1/2}, \tag{4.4.1}$$

is used in the verification tests with $\mathbf{U}_{\mathsf{e}}$ and $\mathbf{U}_{\mathsf{h}}$ the exact and computed solutions, respectively. These exact solutions are described in Appendix A.

4.4.1 "Burgers' solution"

A solution is found of one characteristic of the one-dimensional SWE, symmetrized to vary only in the x–direction, while the other characteristic is fixed. The former characteristic is then reduced to Burgers' equation with use of the latter characteristic, and the resulting Burgers' equation is solved implicitly. These shallow water solutions are valid before the onset of breaking in Burgers' equation. Numerical simulations were carried out in a domain $\Omega = 1 \times 1$ with initial condition $\sqrt{K - 9\,h(x,0)^2\,\mathsf{F}^{-2}} = 0.4\sin(2\pi x)$, and $u = K - 2\,\mathsf{F}^{-1}\sqrt{h}$, $\mathsf{F} = 1$ and $K = 2$. At the zonal boundaries (at $x = 0$ and $x = 1$), periodic boundary conditions were imposed or the exact solutions. Slip flow was imposed at the solid meridional boundaries ($y = 0$ and $y = 1$). The numerical and exact evolution of the water depth $h(x,t)$ is displayed in Figure 4.2. At time $t = t_b = 1/(0.8\,\pi) \approx 0.4$ the initially smooth solution develops a discontinuity. The L_2-norm error and the order of accuracy on non-uniform grids at time $t = 0.2$ are given for mass h and momentum hu in Tables 4.1 and 4.2 for the HLLC and kinetic numerical fluxes on the same meshes, respectively. It shows that the numerical scheme is second order accurate. Note that the two-dimensional code is tested on these non-uniform grids.

4.4.2 Dam-break problem

To demonstrate the shock-capturing ability of the numerical scheme, a Riemann problem consisting of an idealized dam break flow for the one-dimensional SWE is considered

$N \times N$	h		hu	
	L_2 error	Order p	L_2 error	Order p
20×20	9.809e-04		4.629e-04	
40×40	2.556e-04	1.94	1.185e-04	1.96
80×80	6.593e-05	1.95	2.973e-05	1.99
160×160	1.727e-05	1.93	7.650e-06	1.96

Table 4.2: The L_2 error for h and hu and convergence rates for Burgers' solution on non-uniform meshes are shown for the kinetic flux.

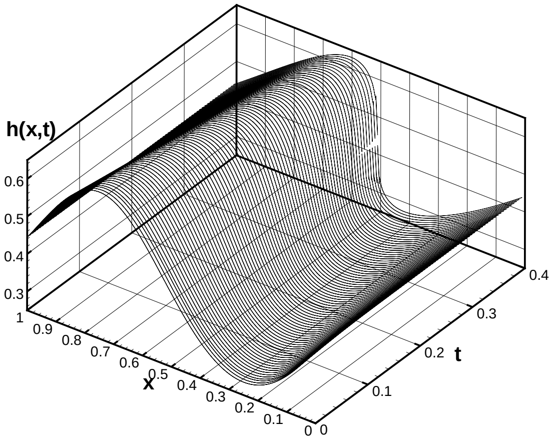

Figure 4.2: Snapshots of the DG and exact solutions of the water depth $h(x, t)$ are shown for the inviscid Burgers' test (solid and dotted lines, respectively).

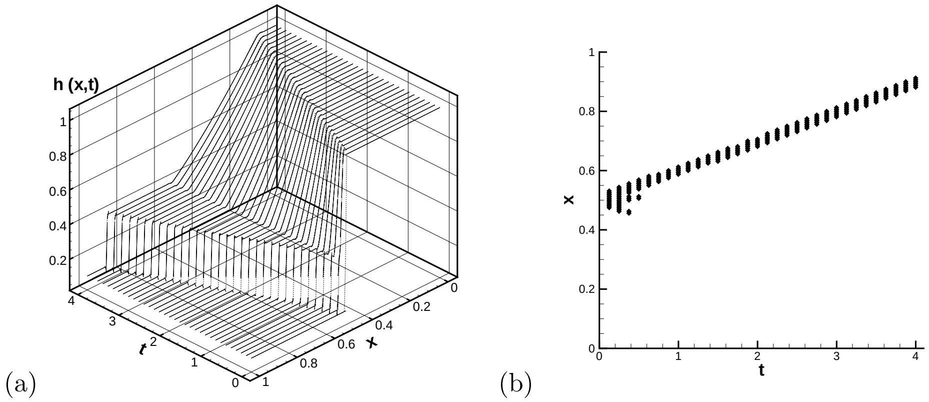

Figure 4.3: a) The evolution of water depth $h(x,t)$ is shown for the dam-break problem; numerical (solid line) and exact (dotted line) solutions are nearly indistinguishable. b) The space-time plot shows where the discontinuity detector identifies a discontinuity (crosses).

in a domain $\Omega = 1 \times 1$ with extrapolating boundary conditions and initial condition: $h(x,0) = 1$ for $x \leq x_0$ and $h(x,0) = 0.10$ for $x > x_0$ and rest flow $\mathbf{u}(x,0) = 0$. At $t = 0$, the dam is removed and the solution develops into a rarefaction wave propagating upstream and a hydraulic jump propagating downstream. Numerical and exact profiles of the water depth h are shown in Figure (4.3a) from time $t = 0$ to time $t = 4$ for the kinetic numerical flux (a similar result holds for the HLLC flux). Krivodonova's discontinuity detector predicts the bore region well, see Figure 4.3b), and the agreement between the numerical and exact solution is good.

4.4.3 Still water test

To test the ability of the numerical scheme to preserve the steady state of rest over varying bathymetry, the numerical solution of the SWE is computed over bathymetry given by $h_b(x) = a\big(b - (x - x_p)\big)\big(b + (x - x_p)\big)/b^2$ for $|x - x_p| \leq b$ and zero otherwise. The exact solution is $\mathbf{u} = 0$ and $H = h + h_b = 1$. ($x_p = 10$, $a = 0.5$, $b = 2$, and $\mathsf{F} = 1$.) The rest state is preserved up to machine precision, at least as long as $t = 20$ on irregular grids. The topography and depth are approximated here with the same basis and test functions. Hence, the rest state is exactly preserved. The proof of the latter is as follows. Due to the continuous approximation of topography h_b all variables are continuous for the rest state. Both numerical fluxes are consistent for the rest state, i.e. $\tilde{F}(U,U) = F(U)$, and therefore reduce to the real flux. Finally, the weak formulation shows that hydrostatic balance is then preserved, see also [142]. The simplicity of this result stems from our continuous approximation of topography, which approach can not be used when the bottom is discontinuous or moving discontinuously. We then refer to the more complex approaches in [42] and [88].

$N \times N$	h		hu	
	L_2 error	Order p	L_2 error	Order p
20×1	1.059e-02		2.545e-02	
40×1	2.190e-03	2.27	4.546e-03	2.49
80×1	4.188e-04	2.38	7.775e-04	2.55
160×1	8.676e-05	2.27	1.330e-04	2.54

Table 4.3: The L_2 error for h and hu and convergence rates are given for subcritical flow on an irregular mesh for the HLLC flux at $t = 20$.

$N \times N$	h		hu	
	L_2 error	Order p	L_2 error	Order p
20×1	8.921e-03		2.546e-02	
40×1	1.836e-03	2.28	4.562e-03	2.48
80×1	3.712e-04	2.30	7.802e-04	2.54
160×1	6.860e-05	2.43	1.366e-04	2.51

Table 4.4: The L_2 error for h and hu and convergences rate are shown for subcritical flow on an irregular mesh for the kinetic flux at $t = 20$ and for the same meshes as in Table 4.3.

4.4.4 Sub- and supercritical flow over an isolated ridge

Consider the flow over an isolated parabolic ridge. By solving a cubic polynomial for given bottom topography and certain upstream Froude number, smooth sub- and supercritical solutions are found [30]. We consider the same bathymetry as in Section 4.4.3 with initial condition: $h + h_b = 1$, $v = 0$ and $u = 1$ in $\Omega = 20 \times 1$. The inflow is specified at the entrance of the channel at $x = 0$ and extrapolated at the outflow boundary at $x = 20$; it depends on the numerical flux (approximating the characteristics) to what extent this information is used. Both sub- and supercritical flows with $\mathsf{F} = 0.2$ and $\mathsf{F} = 1.9$ are considered. After reaching a steady state, accuracy errors and convergence rates are shown for the two numerical fluxes and two flow states in Tables 4.3 to 4.6. Furthermore, the computational costs of the simulations have been calculated. Table 4.7 presents the absolute CPU time T_a (in seconds) for the HLLC and kinetic numerical fluxes (T_a^{hllc} and T_a^{kin}, respectively), as well as the relative computational cost $T_r = T_a^{kin}/T_a^{hllc}$. The kinetic flux is thus more expensive for these simple test, but it turns out to be more robust in complex simulations with multiple bores. Figures 4.4a,b) show comparisons between numerical and exact solutions for the sub- and supercritical cases.

4.5 Validation of the model

From (4.2.8), we see that PV is generated when the dissipation E_D varies along the bore. In the absence of bores, PV is materially conserved. Furthermore, since $h\,\Pi = \partial_x v - \partial_y u$ is the vorticity, sheared flows are vortical flows. The generation of PV is most clearly illustrated when the initial flow has zero vorticity. In the absence of another source of

$N \times N$	h		hu	
	L_2 error	Order p	L_2 error	Order p
20×1	4.216e-02		1.212e-04	
40×1	7.701e-03	2.45	4.826e-06	4.65
80×1	1.464e-03	2.39	8.941e-07	2.43
160×1	2.771e-04	2.40	7.983e-09	6.80

Table 4.5: The L_2 error for h and hu and convergence rates are shown for supercritical flow on an irregular mesh for the HLLC flux at $t = 60$. The superconvergence in $h\,u$ occurs because it is constant in steady state (after transients have disappeared).

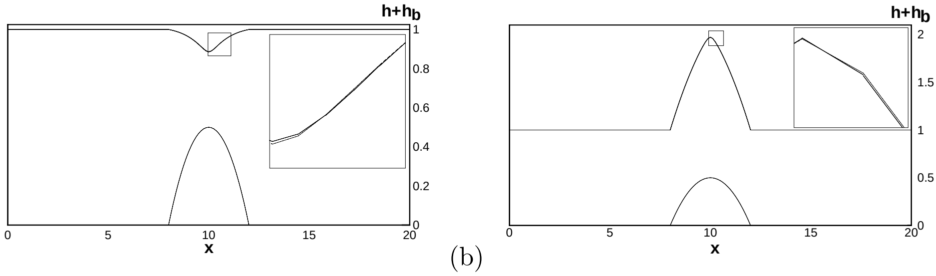

(a) (b)

Figure 4.4: Snapshots of the DG and exact solutions of the topography $h_b(x)$ and water surface $H(x,t) = h_b(x) + h(x,t)$ are shown for: a) subcritical flow (160 elements) and b) supercritical flow (160 elements) over an isolated ridge using the kinetic flux. Computations (solid lines) and exact solutions (dotted lines) are nearly indistinguishable.

$N \times N$	h		hu	
	L_2 error	Order p	L_2 error	Order p
20×1	2.692e-02		1.243e-03	
40×1	6.026e-03	2.15	2.174e-04	2.51
80×1	1.240e-03	2.28	4.649e-05	2.22
160×1	2.267e-04	2.45	8.618e-06	2.43

Table 4.6: The L_2 error for h and hu and convergence rates are shown for supercritical flow on an irregular mesh for the kinetic flux at $t = 60$.

$N \times N$	*Subcritical flow*			*Supercritical flow*		
	T_a^{hllc}	T_a^{kin}	T_r	T_a^{hllc}	T_a^{kin}	T_r
20×1	40	79	1.975	146	217	1.486
40×1	93	134	1.440	264	448	1.696
80×1	160	287	1.790	542	818	1.501
160×1	692	1142	1.650	1097	1709	1.550

Table 4.7: Computational performance of the subcritical and supercritical flow tests.

dissipation than the one in bores, PV can only be generated through non-uniform shallow-water wave breaking represented by these bores. The following three simulations aim to illustrate the PV generation mechanism. In all these examples, the expression (4.2.8) allows us to qualitatively predict the ensuing vortical flows as the associated shear profile or signature of the eddies generated. Once the PV is generated it is actively advected by the flow.

The following three cases are considered. (i) A linear normal mode solution of a gravity wave is used as initial condition in simulations of the nonlinear flow. Given these linear solutions at time zero, $u_0(\mathbf{x}), v_0(\mathbf{x})$ and $\eta_0(\mathbf{x})$, the initial condition of the nonlinear flow is $u_0(\mathbf{x}), v_0(\mathbf{x})$ and $h_0(\mathbf{x}) = H + \eta_0(\mathbf{x})$ with H the constant still water depth and $\eta_0(\mathbf{x})$ the initial departure of the free surface from it. In addition, both for the linear and nonlinear flow, the PV is zero initially and remains zero unless PV is generated through non-uniform bore formation. Given a periodic channel in the x direction, the average potential vorticity $q = \bar{\Pi}(y,t)$ and shear $\bar{u}(y,t)$, both averaged in the x direction, signal a transfer from the zero PV gravity waves to the vortical flow. (ii,iii) Uniform bores are simulated to encounter non-uniform topographical features, such that the non-uniform bores emerge and generate PV in the form of eddies whose signs we predict. Peregrine [36] sketches qualitatively how bores of finite length or pierced in the middle generate eddies. In particular, we simulate flow of an initially uniform bore over (ii) conical and (iii) Gaussian topography to compare with Hu's results [51].

4.5.1 Shallow water waves and bores in a channel

Nonlinear wave breaking is investigated by initializing the flow with a gravity wave solution of the linearized shallow water equations, in which $h(\mathbf{x},0) = H + A\sin(ly)\,\sin k\,x$

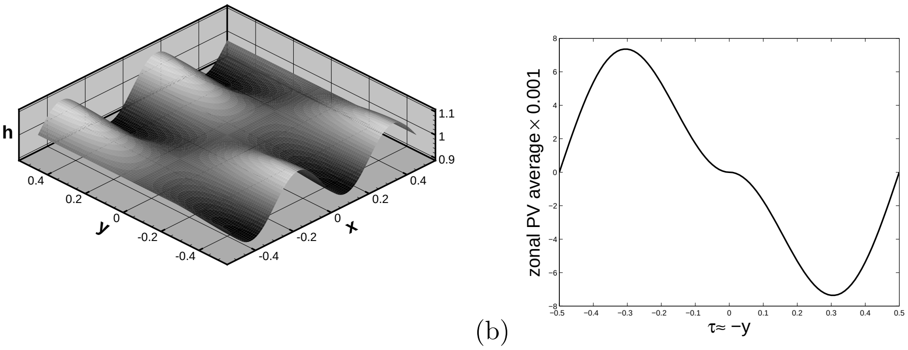

(a) (b)

Figure 4.5: (a) Initial condition for the test with steepening waves and bores in a channel with a resolution of 100×100 elements, see Appendix D. (b) We show an estimate of the PV generated by a non-uniform bore based on formulas (4.2.8) and (4.5.1). The along-bore coordinate τ is roughly opposite to y.

with $l = (2\,n + 1)\,\pi/L_y$, $k = 2\,\pi\,m/L_x$; and, $\mathsf{F} = H = 1, A = 0.1$ and $n = 0, m = 2$. The domain is a channel of size $L_x \times L_y = 1 \times 1$ with a flat bottom, solid walls at $y = \pm 0.5$, and periodic boundary conditions in the zonal direction x. The PV is initially zero. We expect the initially harmonic waves to steepen, break into bores, and subsequently dampen due to the localized energy dissipation (4.2.7) at the bores. Free surface profiles and PV contours are shown at times $t = 0.2, 0.5, \ldots, 15$ in Figures 4.6 to 4.7. The wave peaks depicted in Figure 4.5a) appear to be preserved in the depth profiles, shown at subsequent times $t = 0.2$ and $t = 0.5$ in Figures 4.6a) and 4.6c), respectively. PV should be zero before wave breaking starts; what is seen at $t = 0.0$ and $t = 0.2$ are second-order truncation errors. This suggest the following estimate of h_1 and h_2 from the initial condition given above

$$h_2 = H + A\sin\left(l\,|\tau|\right) \qquad \text{and} \qquad h_1 = H - A\sin\left(l\,|\tau|\right) \tag{4.5.1}$$

with $-0.5 < \tau < 0.5$ and τ aligned roughly opposite to y as the bore is traveling in the negative x-direction. Although the bores will commence near the walls, they are seen to grow into the center of the channel. Based on our rough estimates (4.5.1) and (4.2.8), we calculate the approximate PV profile given in Figure 4.5b). We expect the formation of two jets after many wave periods with a negative zonal average $\bar{u}(y, t) < 0$ for $y > 0$ ($\tau < 0$), since PV is positive, and negative for $y < 0$ ($\tau > 0$). Note that the harmonic waves specified as initial condition have zero zonal average. The estimated profile of PV in Figure 4.5 is recognized in the early calculated profiles of zonally averaged PV in Figure 4.8. A rough estimate of the time t_b of wave breaking is given by using the initial profile for one characteristic, which yields the Burgers' equation estimate $t_b \approx 0.53$. For smooth flows in the zonally periodic channel the energy $\mathsf{E}(t) = \frac{1}{2}\int_{\Omega_\mathrm{h}} h|\mathbf{u}|^2 + \mathsf{F}^{-2}h^2 d\Omega = \sum_K \frac{1}{2}\int_{K_\mathrm{h}} h|\mathbf{u}|^2 + \mathsf{F}^{-2}h^2 d\Omega$ is conserved. Energy is plotted from time $t = 0$ to $t = 25$ in Figure 4.9a). It is seen to be approximately conserved before the onset of breaking around $t = 0.5$: thereafter energy is dissipated in the non-uniform bores. Once the bores have disappeared, the energy should be conserved exactly again, which is approximately the case in the numerics for large times ($t \gtrapprox 15$). In Figure 4.9b) zonally averaged profiles $\bar{u}(y,t)$ of the velocity are shown as function of y and t. Two jets eventually form near the walls.

4.5.2 Flow over a conical hump

The passage of a bore over a conical hump is considered, cf. Matsutomi and Mochizula [56] and Hu [51]. The bore is generated via a dam break and the geometry is given in Figure 4.10. The isolated conical shaped hump of height h_{b_v} and radius r_v,

$$h_b(\mathbf{x}) = \begin{cases} h_{b_v} - \frac{h_{b_v}}{r_v}\sqrt{(x-x_v)^2+(y-y_v)^2} & \text{if } (x-x_v)^2+(y-y_v)^2 \le r_v^2 \\ 0 & \text{otherwise} \end{cases},$$

is located in a rectangular domain $\Omega = [L_x \times L_y]$ and centered at (x_v, y_v). The initial condition is given by a discontinuity in the water surface $h(\mathbf{x},0) = h_l$ for $x < x_0$ and $h(\mathbf{x},0) = h_r$ for $x \ge x_0$ and fluid initially at rest, $\mathbf{u}(\mathbf{x},0) = 0$. Parameter values are $h_{b_v} = 0.012$, $r_v = 1.2$, $(x_v, y_v) = (2.5, 1.3)$, $L_x = 4$, $L_y = 2.6$, $x_0 = 1$, $h_l = 0.09$, $h_r = 0.02$, and $\mathsf{F} = 1$. All boundaries are considered to be solid walls except an open boundary at $x = 4$. After the collapse of the dam, a bore is formed and propagates downstream over the conical hump. A qualitative prediction of the PV generation follows from (4.2.8). Bore dissipation is higher in the shallower waters over the conical hump. Consider a bore aligned approximately in the y-direction. We and also Ambati and Bokhove [142] observe from their simulations that the free surface remains rather flat, which allows a more quantitative analysis of (4.2.8). For $y < 0$ and $\tau < 0$, $\partial E_D/\partial y > 0$ and vice versa for $y > 0$ and $\tau > 0$. Hence, a positive PV anomaly is expected for $y > 0$ and a negative one for $y < 0$, which are symmetric in shape due to the symmetry of the conical hump. After the PV anomaly has been generated, it is advected along. Figure 4.11 shows that the evolution of the PV —at times $t = 0, 2, 4, 6, 8$ and $t = 10$— confirms our qualitative prediction, and is similar to the simulations of Hu [51], who used LeVeque's finite volume scheme [119]. The numerical noise in our simulation, caused by the discontinuous first derivative of the topography, is less than in [51]. The global vorticity or weighted PV should remain zero, which is approximately true in the simulations. Finally, we display the surface profiles at various times in Fig. 4.12; these compare well with the experiments of Matsutomi and Mochizula [56] and Hu [51].

4.5.3 Flow over a Gaussian hump

In this test, a bore forms after a dam breaks in a rectangular domain $\Omega = [L_x \times L_y]$ with bottom topography consisting of a isolated Gaussian hump defined by

$$h_b(\mathbf{x}) = h_{b_v} e^{\left(-12.5(x-x_v)^2 - 12.5(y-y_v)^2\right)},$$

centered at (x_v, y_v) and with maximum height h_{b_v}. The initial condition is given by $h(\mathbf{x},0) = h_l$ for $x < x_0$ and $h(\mathbf{x},0) + h_b(\mathbf{x}) = h_r$ for $x \ge x_0$ and fluid initially at rest,

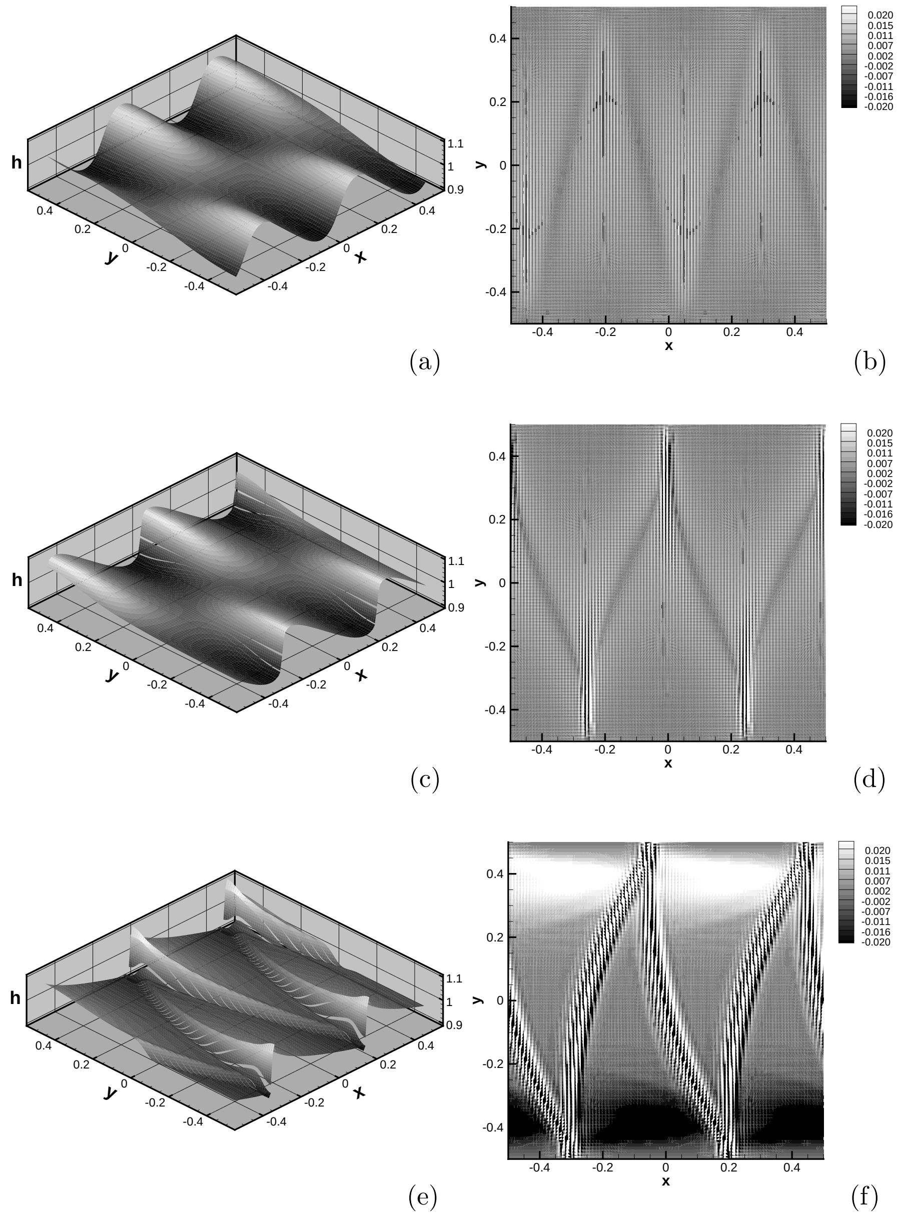

Figure 4.6: a) Numerical solution of $h(\mathbf{x}, t)$ and b) PV for steepening waves in a channel at time $t = 0.20$. Waves travel in the minus x-direction. The period of corresponding harmonic waves is 0.49. c) Numerical solution of $h(\mathbf{x}, t)$ and d) PV for breaking waves in a channel at time $t = 0.50$. Bore formation has begun. (e,f) Same at time $t = 2$. Before breaking, just begun near the walls at $t = 0.5$, PV should be zero, but as it is not preserved numerically some PV noise is visible in (b) and (d). This noise will stay visible around the bores in (f), where the numerically solution limits numerical oscillations, which nevertheless locally hamper the calculation of PV as it is a derived quantity from our prime flow variables.

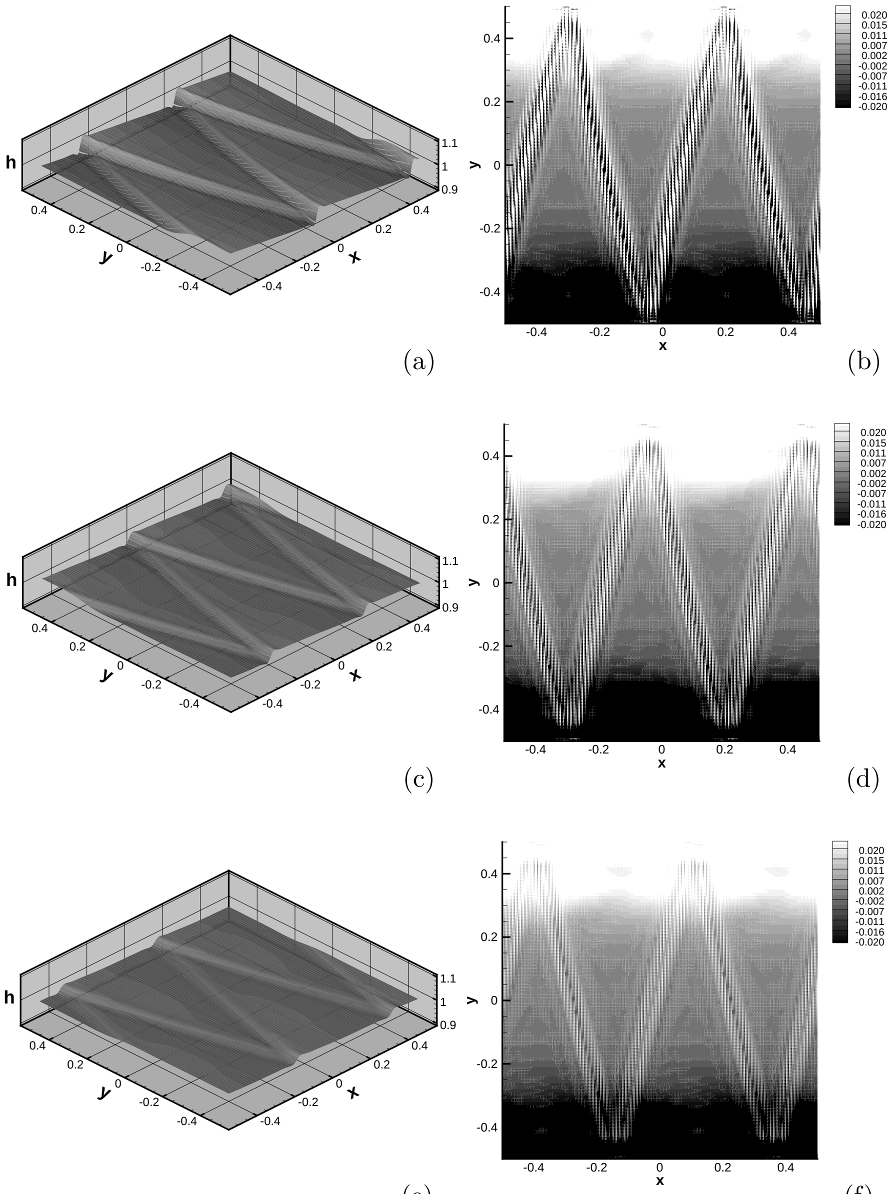

(a) (b)

(c) (d)

(e) (f)

Figure 4.7: a) Numerical solution of $h(\mathbf{x}, t)$ and b) PV in a channel at time $t = 8$. (c,d) Same at time $t = 15$. (e,f) Same at $t = 25$. PV noise stays visible around the bores in (b,d,f).

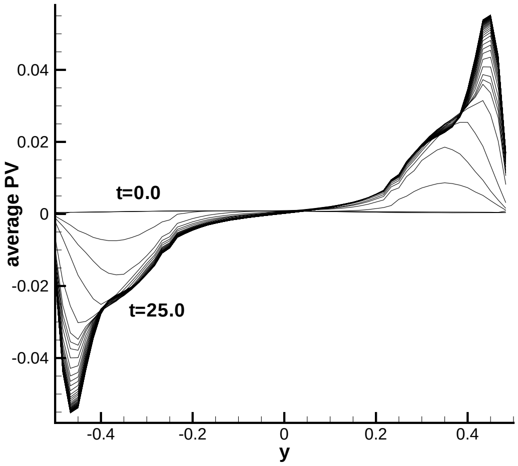

Figure 4.8: The zonal average of the PV, defined by $q(y,t) = \bar{\Pi}(\mathbf{x}, t)$, is shown as function of y and t.

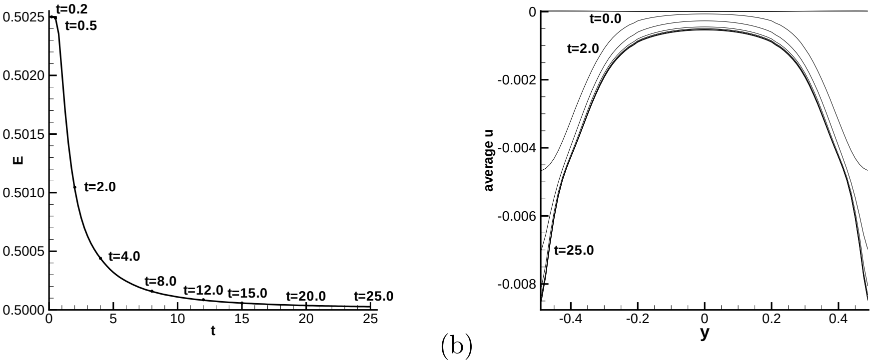

(a) (b)

Figure 4.9: (a) The global energy, the sum of kinetic and potential energy, is shown as function of time. Before bores emerge, the energy should be conserved exactly, which is approximately the case in the numerics. After bore formation, energy is dissipated in the bores, which is clearly visible after $t \approx 0.5$, till the bores have dissipated at large times. (b) The zonal average of the velocity u, defined by $\bar{u}(y,t)$, is shown as function of y and t at times $0, 0.2, 0.5, 2, 4, 8, 12, 15, 20, 25$.

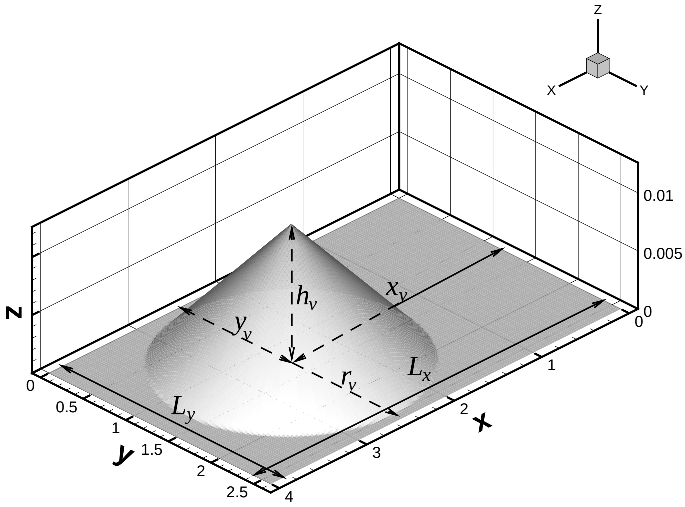

Figure 4.10: The geometry is shown for the conical hump experiment.

$\mathbf{u}(\mathbf{x}, 0) = 0$. Parameter values are $h_{b_v} = 0.015$, $(x_v, y_v) = (1.75, 1.75)$, $L_x = L_y = 3.5$, $x_0 = 0.5$, $h_l = 0.11$, $h_r = 0.02$, and $\mathsf{F} = 1$. Boundary conditions are the same as in the conical hump test, but the exit of the channel is located at $x = 3.5$. After the collapse of the dam, a bore is formed and propagates downstream over the Gaussian hump. The generation of two initial eddies and their signs, in Figure 4.13 at times $t = 4$ and 6, has the same explanation as in the previous test of flow over a conical hump. Figure 4.13 at times $t = 8$ and $t = 10$ shows the formation of two new eddies arising from a reflected bore. In Figure 4.14, a second hydraulic jump is seen to develop at time $t = 8$ as the bore propagates downstream. The bore propagates against the current with maximum dissipation along the centerline $y \approx 0$ where waters are most shallow, so $y < 0$ corresponds to $\tau > 0$ and $\partial E_D / \partial \tau < 0$ and vice versa for $y > 0$ and $\tau < 0$. Hence, for the second group of eddies, formation of a negative PV anomaly is expected for $y < 0$ ($\tau > 0$) and a positive one for $y > 0$ ($\tau < 0$). Our simulations confirm these and Hu's results [51].

4.5.4 Oblique hydraulic jumps in flow through a contraction

Theoretical [5] and experimental results [6] reveal the development of steady oblique hydraulic jumps in narrow flumes with a contraction. From the shock relations of the shallow water system (4.2.3) and (4.2.4), the jump ratio h_1/h_0 across the shock and the angle θ_s of the shock can be determined by the following equations [5]:

$$\frac{h_1}{h_0} = \frac{\tan\theta_s}{\tan(\theta_s - \theta_c)} \quad \text{and} \quad \sin\theta_s = \sqrt{\frac{1}{2\mathsf{F}^2}\frac{h_1}{h_0}\left(1 + \frac{h_1}{h_0}\right)}, \tag{4.5.2}$$

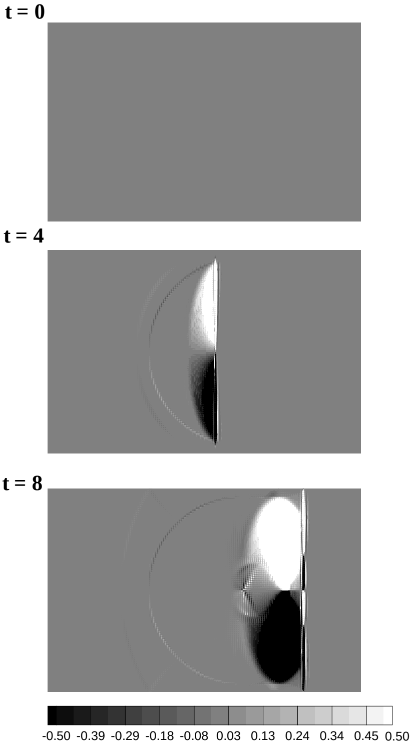

Figure 4.11: Contours of PV generated by a dam break flow over a conical hump. We used 160×100 elements.

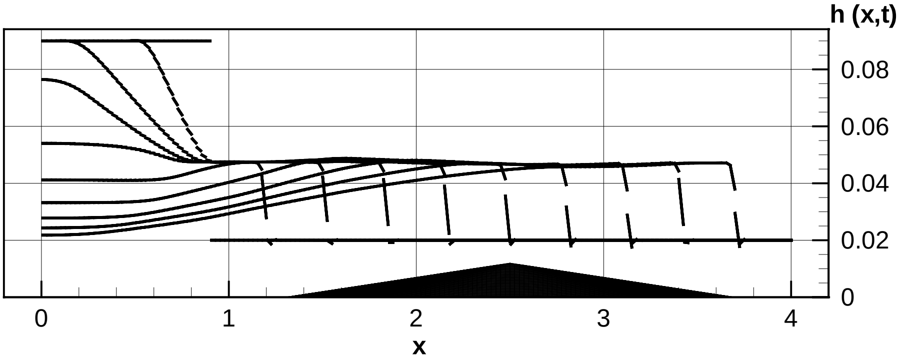

Figure 4.12: Surface profiles of $h(\mathbf{x}, t)$ are shown in the middle of the channel at times 0.0 to 10.0 with an increment of 1.0. These profiles compare favorably with simulations of Hu [51] and laboratory experiments of Matsutomi and Mochizula [56].

where h_0 and h_1 are the upstream and downstream depths across the oblique hydraulic jump, and θ_c and θ_s are the angles of the contraction and the shock measured relative to the horizontal wall of the flume, respectively. To assess the convergence to steady state and to compare the HLLC and kinetic flux, we perform simulations of two-dimensional flow through a flume with a contraction with a scaled minimum width b_c and a constant upstream width $b_0 = 1$. The initial condition was a flow at rest with a small constant depth $h(x, 0) = 0.001$. Simulations were run to steady state for a Froude number $\mathsf{F} = 3.65$, outflow and solid wall boundary conditions, and inflow with $h(0, t) = 1, u(0, t) = 1, v(0, t) = 0$. To avoid negative water depths, the slopes in the numerical approximation of water depth were set to zero when the depth becomes smaller than $h(x, 0)$. The computational domain, non-dimensionalized with the flume width $l_0^* = 20$ cm, consists of an inlet section, a contraction section, and an outlet section, see Fig. 4.15a). This configuration naturally enforces a critical condition at the point of minimum width, at which point in the experiment the water falls into a bucket. The length of the contraction along the wall is 1.5. For $b_c = 0.6$, theoretical calculations yield a jump ratio $h_1/h_0 = 1.5463$ and a jump angle $\theta_s = 22.608°$, and for $b_c = 0.7$, $h_1/h_0 = 1.4019$ and $\theta_s = 20.824°$. The convergence to steady state has been considered for simulations on four different meshes. Details of each mesh are given in Table 4.8 as well as the convergence rates to the exact shock angle and jump ratio.

Figure 4.15a) shows the steady oblique jumps at time $t = 7.0$. A similar result was obtained experimentally by Akers [6] as shown in Figure 4.15b). The computational cost of simulations is presented in Table 4.9 and shows ultimately that runs with the kinetic flux are faster for both second and third order Runge–Kutta methods. While the kinetic flux is slower per time step, it allows the use of larger time steps. The same steady state results were reached in all these simulations.

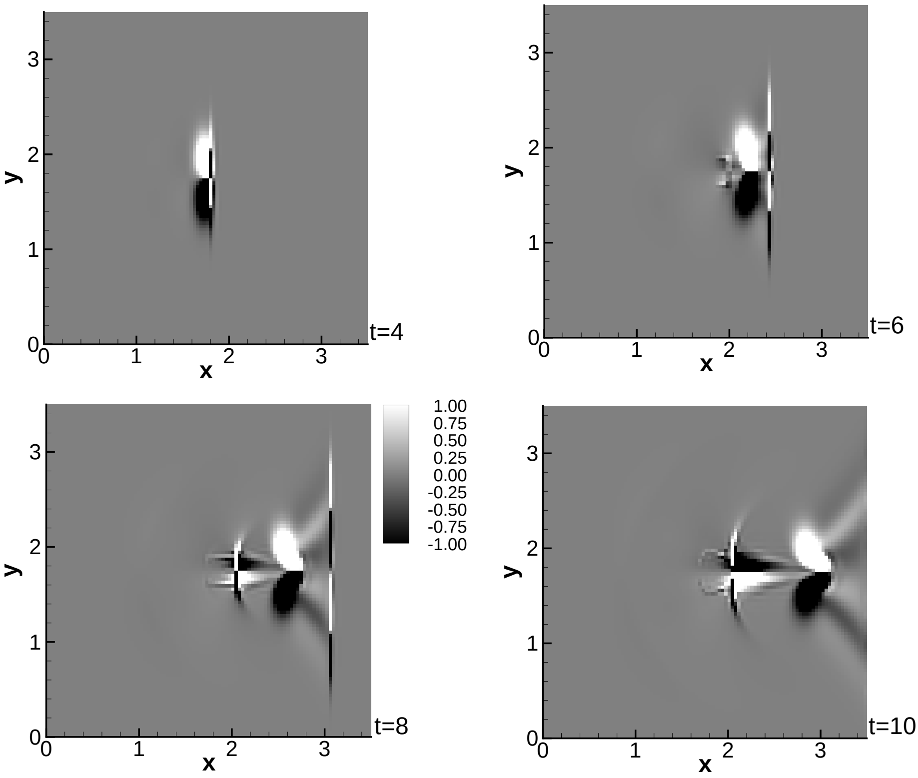

Figure 4.13: Contours of PV generated by a dam break flow over a Gaussian hump. We used 100 × 100 elements.

Mesh	*Flow through a contraction*						
	Inlet	*Contraction*	*Outlet*	b_c	θ_c	θ_s	h_1/h_0
I	10 × 10	10 × 10	10 × 5	0.6	7.54°	$22.96° \pm 0.72°$	1.551 ± 0.007
II	20 × 20	20 × 20	20 × 10	0.6	7.54°	$22.76° \pm 0.20°$	1.551 ± 0.005
III	40 × 40	40 × 40	40 × 20	0.6	7.54°	$22.70° \pm 0.08°$	1.551 ± 0.001
IV	40 × 40	40 × 40	40 × 20	0.7	5.65°	$20.85° \pm 0.08°$	1.400 ± 0.001

Table 4.8: Computational meshes used for flow through a contraction and numerical values of θ_s and h_1/h_0.

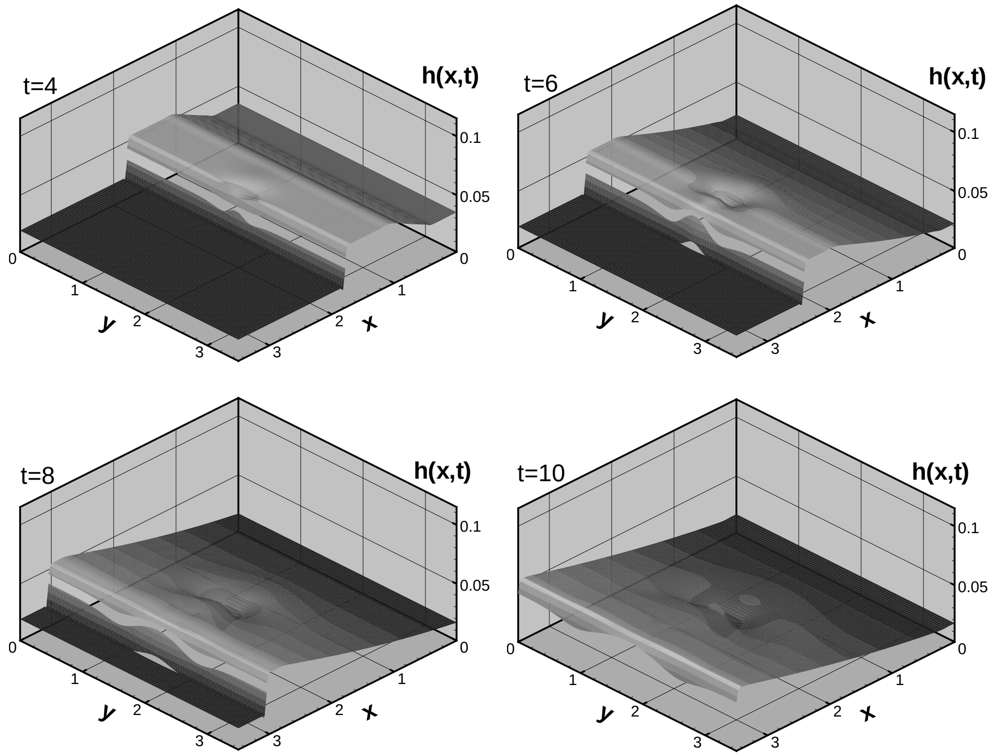

Figure 4.14: Free surface profiles at times $4.0, 6.0, 8.0$ and 10.0.

Mesh	*Runge–Kutta 2*			*Runge–Kutta 3*		
	T_a^{hllc}	T_a^{kin}	T_r	T_a^{hllc}	T_a^{kin}	T_r
I	89	124	1.393	134	291	2.171
II	687	531	0.772	1540	938	0.609
III	6460	2195	0.339	13287	3742	0.281

Table 4.9: Computational performance for the simulated flow through a contraction using the second and third order Runge–Kutta time integration methods.

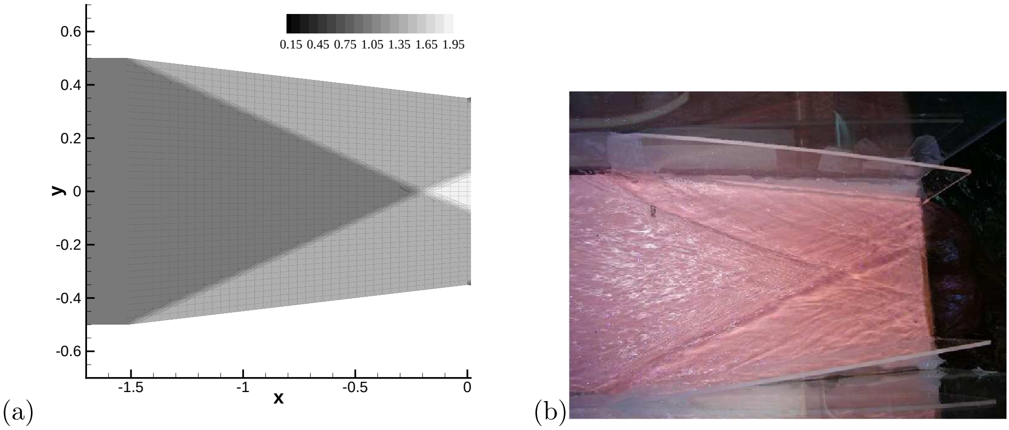

Figure 4.15: a) Numerical results of steady oblique hydraulic jumps in a channel with a contraction for mesh *IV*. b) Experimental results of steady oblique hydraulic jumps in a channel with a contraction, with Froude number $\mathsf{F} = 3.65$ at the inlet and minimum contraction width $b_c = 0.7$ at the critical point and outlet in the experiment. Measured jump ratio is unknown and angle $\theta_s = 22.0^\circ \pm 1^\circ$; courtesy Ben Akers [6].

4.6 Conclusions

A discontinuous Galerkin finite element discretization has been presented for shallow water flows over varying bathymetry. This discretization had the following novel aspects. First, two accurate numerical fluxes were presented and compared, the HLLC numerical flux [105] and a kinetic flux [15]. While the HLLC flux is a direct approximation to the Riemann problem in a Godunov-type approach at second order in the absence of bathymetry, the kinetic approach directly and more consistently includes the bathymetric terms. The kinetic approach yields a spatial discretization of the relevant Vlasov equation, which is subsequently transformed to the discretized hydrodynamic equations, using the transformation between the partial differential equations of the kinetic and SWE. The resulting weak formulations differ only with respect to the numerical flux, and both approaches can be extended to higher order. Second, the bathymetry was projected on the quadrilateral elements with the usual second-order finite element basis functions such that the resulting discretized bathymetry was continuous. In addition, the flow variables were also projected using these four basis functions. Consequently, the rest flow state can be preserved exactly in the discretization and to machine precision in the implementation. On triangles, this preservation can be achieved directly with the usual linear basis functions. The verification of numerical and exact solutions showed the methods to be second order in spatial accuracy using equal-order interpolation for the approximation of the flow variables.

The shallow water equations globally and locally preserve mass, energy, and mass weighted functions of the potential vorticity (PV) for smooth flows and appropriate boundary conditions. The PV is also a materially conserved quantity consisting of the total vertical vorticity, $\partial_x v - \partial_y u$, divided by the depth. In the presence of non-uniform bores, PV anomaly can be generated (cf. section 4.2.1 and [35]). By construction, our numerical method only conserves momentum (for h_b constant) and mass exactly. We therefore validated simulations of bore-vortex interactions against a qualitative and asymptotic analysis of the generation of potential vorticity (PV) anomalies. Consequently, we could predict the signs of the emerging vortices and shear flows. The latter validation is important because numerical schemes may generate vortices of incorrect shape and sign, as was shown by Hu [51]. The counterpart in compressible flows would be the (in)correct generation of entropy by non-uniform shocks. We considered, in particular, bore-vortex interactions of breaking waves in a channel and the flow of a bore over conical and Gaussian topography. The emerging vortices simulated in the flow over the conical and Gaussian hump compared favorably with simulations of Hu [51], performed with LeVeque's finite volume scheme [119], and laboratory experiments of Matsutomi and Mochizula [56]. Final simulations compared the numerical fluxes for oblique hydraulic jumps in a contraction, also with a laboratory experiment [6]. The kinetic flux turned out to be more robust when shocks are involved.

Acknowledgments: P.T. gratefully acknowledges a two-year scholarship of the EU Alβan program. Financial assistance from Conicet (Argentina) is also gratefully acknowledged. We kindly thank Professor Howell Peregrine for his insightful comments on PV generation by bores and for pointing out an error. We thank the anonymous reviewers for their valuable remarks.

Appendices

A Summary of exact solutions

Exact solutions used in the verification tests of Section 4.4 are given next.

A.1 Burgers' solution

An exact solution of the Burgers' equation has been constructed by taking one of the Riemann invariants of the one-dimensional frictionless SWE to be constant. The solution of u and h can be related to the implicit solution $w = w(x,t)$ of the inviscid Burgers' equation before wave breaking. The exact solution for h and u is given by

$$h = \big((K - w)\,\mathsf{F}/3\big)^2, \quad u = K - 2\mathsf{F}^{-1}\sqrt{h}, \tag{A.1}$$

with $w(x,t) = w_0(x')$, $x = x' + w_0(x')\,t$ and $w(x,0) = w_0(x)$ as initial condition. Wave breaking occurs at time $t_b = -1/\min(dw_0/dx)$.

A.2 Flow over isolated ridge: subcritical and supercritical cases

Assuming a steady state, Houghton and Kasahara [30] analyzed the one-dimensional flow over a smooth convex obstacle. The solution to (4.2.3) and (4.2.4) is

$$hu = \mathcal{K}_1 \quad \text{and} \quad \mathsf{F}^2\, u^2/2 + (h + h_b) = \mathcal{K}_2, \tag{A.2}$$

where $\mathcal{K}_1$ and $\mathcal{K}_2$ are integration constants. Far away from the obstacle, it can be assumed that the non-dimensional velocity and water depth are both equal to one and the bed topography level is equal to zero. Therefore,

$$\mathcal{K}_1 = 1, \qquad \mathcal{K}_2 = \mathsf{F}^2/2 + 1. \tag{A.3}$$

After some algebraic manipulations, the following third-order equation in u is obtained

$$\mathsf{F}^2\, u^3/2 + (h_b - \mathsf{F}^2/2 - 1)\, u + 1 = 0, \tag{A.4}$$

which is solved to obtain the flow over a smooth convex obstacle.

B Proof of proposition 4.3.1

From (4.3.21) and (4.3.22) we find that

$$h = K\,G^2 = \int \mathsf{D}\,\mathrm{d}\bar{\zeta} \quad \text{and} \quad (\sigma\, u_i) = \mu_i = K\,G^2\, u_i = \int \zeta_i\,\mathsf{D}\,\mathrm{d}\bar{\zeta}. \tag{B.1}$$

Multiply (4.3.20) by the vector $(1, \bar{\zeta})^T$ and integrate over $\bar{\zeta}$ to obtain

$$\int \left[\partial_t \mathsf{D} \begin{pmatrix} 1 \\ \bar{\zeta} \end{pmatrix} + \boldsymbol{\nabla}\cdot(\bar{\zeta}\,\mathsf{D}) \begin{pmatrix} 1 \\ \bar{\zeta} \end{pmatrix} - \boldsymbol{\nabla}_{\zeta}\cdot[(\mathsf{F}^{-2}\,\boldsymbol{\nabla} h_b)\,\mathsf{D}] \begin{pmatrix} 1 \\ \bar{\zeta} \end{pmatrix}\right] \mathrm{d}\bar{\zeta} = 0. \tag{B.2}$$

Evaluating the integrals in (B.2) while using definition (4.3.22), (B.1), the symmetry properties (4.3.21) of χ, integration by parts, and (4.3.23), we find

$$\begin{aligned} \int \mathsf{D}\,(1,\bar{\zeta})^T \mathrm{d}\bar{\zeta} &= (h, h\,\mathbf{u})^T, \\ \int \boldsymbol{\nabla}\cdot(\bar{\zeta}\,\mathsf{D}) \begin{pmatrix} 1 \\ \bar{\zeta} \end{pmatrix} \mathrm{d}\bar{\zeta} &= \begin{pmatrix} \boldsymbol{\nabla}\cdot(h\,\mathbf{u}) \\ \partial_x(h\,u^2 + P(h)) + \partial_y(h\,u\,v) \\ \partial_x(h\,u\,v) + \partial_y(h\,v^2 + P(h)) \end{pmatrix}, \\ \int -\boldsymbol{\nabla}_\zeta\cdot[(\mathsf{F}^{-2}\,\boldsymbol{\nabla} h_b)\,\mathsf{D}] \begin{pmatrix} 1 \\ \bar{\zeta} \end{pmatrix} \mathrm{d}\bar{\zeta} &= \begin{pmatrix} 0 \\ h\,\mathsf{F}^{-2}\,\partial_x h_b \\ h\,\mathsf{F}^{-2}\partial_y h_b \end{pmatrix}. \end{aligned} \tag{B.3}$$

Combining expressions (B.3) with (B.2) confirms the proposition. Finally, we get $K = h^2/P(h)$ and $G = \sqrt{P(h)/h}$, since $K\,G^2 = h$ and $K\,G^4 = P(h)$. ☐

C Integral expressions in discretized kinetic formulation

In the following, details about the implementation of the kinetic numerical flux are presented In (4.3.27)–(4.3.29), evaluation is required of the integrals

$$\left(\tilde{F}^{\text{out}}_\sigma(U^-), \tilde{F}^{\text{out}}_{\boldsymbol{\mu}}(U^+)\right) = \int_{\hat{n}^-_{\mathsf{k}}\cdot\bar{\zeta}>0} \mathsf{D}^-\,(\hat{n}^-_{\mathsf{k}}\cdot\bar{\zeta})\,(1,\bar{\zeta})^T\,\mathrm{d}\bar{\zeta} \tag{C.1}$$

$$\left(\tilde{F}^{\text{in}}_\sigma(U^+), \tilde{F}^{\text{in}}_{\boldsymbol{\mu}}(U^+)\right) = \int_{\hat{n}^-_{\mathsf{k}}\cdot\bar{\zeta}\leq 0} \mathsf{D}^+\,(\hat{n}^-_{\mathsf{k}}\cdot\bar{\zeta})\,(1,\bar{\zeta})^T\,\mathrm{d}\bar{\zeta}, \tag{C.2}$$

where

$$\mathsf{D} = K(h)\,\chi\left((\bar{\xi} - \mathbf{u})/G(h)\right). \tag{C.3}$$

In two dimensions a simple choice of $\chi(\bar{w})$ in (C.3) satisfying (4.3.21) is

$$\chi(\bar{w}) = \left\{ \begin{array}{ll} C_\chi = 1/4\,\pi & \text{if} \quad |\bar{w}| < R = 2 \\ 0 & \text{if} \quad |\bar{w}| \geq R \end{array} \right. . \tag{C.4}$$

The line $\hat{n}_{\mathsf{k}}\cdot\bar{\zeta} = \hat{n}_{\mathsf{k}}\cdot(G\,\bar{w} + \mathbf{u}) = 0$ demarcates the "left" and "right" integration regions in (C.1) and (C.2). Defining the distance $R_I = |\hat{n}_{\mathsf{k}}\cdot\mathbf{u}|/G$ of the origin in the $\bar{w}$–plane to the line $\hat{n}_{\mathsf{k}}\cdot\bar{\zeta} = 0$, the following situations emerge considering the left region in which the domain of integration is $\hat{n}_{\mathsf{k}}\cdot\bar{\zeta} > 0$:

a) the line does not intersect the circle where $\chi(\cdot)$ jumps to zero, so $R_I > R$, and the circle lies outside the integration domain $\hat{n}_{\mathsf{k}}\cdot\bar{\zeta} > 0$ since $\hat{n}_{\mathsf{k}}\cdot\mathbf{u} < 0$, *i.e.* the origin $\bar{w} = 0$ is excluded;

b) the line does not intersect the circle where $\chi(\cdot)$ jumps to zero, so $R_I > R$, and the circle lies inside the integration domain $\hat{n}_{\mathsf{k}}\cdot\bar{\zeta} > 0$ since $\hat{n}_{\mathsf{k}}\cdot\mathbf{u} \geq 0$, *i.e.* the origin $\bar{w} = 0$ is included; and c1) circle and line intersect $R_I \leq R$ since $\hat{n}_\mathsf{k} \cdot \mathbf{u} < 0$. *i.e.* the origin $\bar{w} = 0$ is excluded; and

c2) circle and line intersect $R_I \leq R$ since $\hat{n}_\mathsf{k} \cdot \mathbf{u} \geq 0$, *i.e.* the origin $\bar{w} = 0$ is included.

These situations are sketched in Fig. 16.

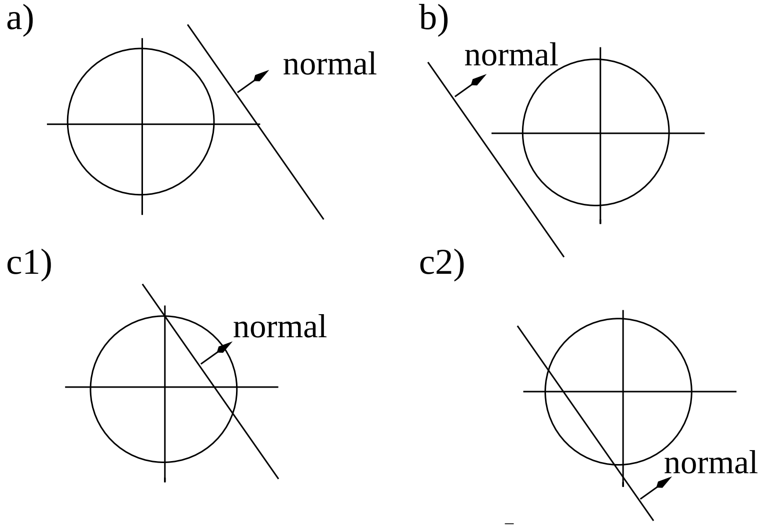

Figure 16: The circle with radius R in (C.4) and the line $\hat{n}_\mathsf{k} \cdot \bar{\zeta} = 0$ are sketched in the $\bar{w}$–plane. Situations at stake in the $\bar{w}'$–plane: a) $R_I > R$ and $\hat{n}_\mathsf{k} \cdot \mathbf{u} < 0$; b) $R_I > R$ and $\hat{n}_\mathsf{k} \cdot \mathbf{u} \geq 0$; c1) $R_I \leq R$ and $\hat{n}_\mathsf{k} \cdot \mathbf{u} < 0$; and c2) $R_I \leq R$ and $\hat{n}_\mathsf{k} \cdot \mathbf{u} \geq 0$.

For the left region, in situation a) the integrals are zero, and in situation b) the symmetry properties can be used. Vice versa, for the right region, in situation b) the integrals are zero, and in situation a) the symmetry properties can be used. Situation c) requires more attention. Rotating to new coordinates $\bar{w}'$ such that the line intersects the positive w_1'-axis only and runs parallel to the w_2'-axis. In case c1), with $\hat{n}_\mathsf{k} = (n_1, n_2)$ the unit vectors of $\bar{w}'$ are

$$\hat{e}_1' = (n_1, n_2) = (m_1, m_2) \qquad \text{and} \qquad \hat{e}_2' = (-n_2, n_1) = (-m_2, m_1). \tag{C.5}$$

In case c2), with $\hat{n}_\mathsf{k} = (n_1, n_2)$ the unit vectors of $\bar{w}'$ are

$$\hat{e}_1' = -(n_1, n_2) = (m_1, m_2) \qquad \text{and} \qquad \hat{e}_1' = (n_2, -n_1) = (-m_2, m_1). \tag{C.6}$$

Hence, the two coordinates can be related as follows

$$w_1 = m_1 w_1' - m_2 w_2' \qquad \text{and} \qquad w_2 = m_2 w_1' + m_1 w_2'. \tag{C.7}$$

Thus,

$$\hat{n}_\mathsf{k} \cdot \bar{w} = (n_1 m_1 + n_2 m_2) w_1' + (-n_1 m_2 + n_2 m_1) w_2' = a_1 w_1' + a_2 w_2'. \tag{C.8}$$

The following basic integrals in the $\bar{w}'$–plane are calculated using xMaple under Linux

$$\begin{aligned} I_0 = & C \int_B \mathrm{d}\bar{w}' \\ & =(1/(4\,\pi))\,(2\,\pi - 4\,(R_I/2)\,\sqrt{1-(R_I/2)^2} - 4\arcsin(R_I/2)) \\ I_1 = & C \int_B w'_1\,\mathrm{d}\bar{w}' = (4/(3\,\pi))\,(1-(R_I/2)^2)^{3/2} \\ I_2 = & C \int_B w'_2\,\mathrm{d}\bar{w}' = 0 \end{aligned} \tag{C.9}$$

and

$$\begin{aligned} I_{11} = & C \int_B (w'_1)^2\,\mathrm{d}\bar{w}' \\ & =(2\,\pi + (2\,R_I - R_I^3)\,\sqrt{1-(R_I/2)^2} - 4\arcsin(R_I/2))/(4\,\pi) \\ I_{12} = & C \int_B w'_1\,w'_2\,\mathrm{d}\bar{w}' = 0 \\ I_{22} = & C \int_B ({w'}_2)^2\,\mathrm{d}\bar{w}' \\ & = (6\,\pi + (-10\,R_I + R_I^3)\,\sqrt{1-(R_I/2)^2} - 12\arcsin(R_I/2))/(12\,\pi) \end{aligned} \tag{C.10}$$

with $B = \{\bar{w} | w'_1 > R_I, |\bar{w}'| < R\}$ and $R_I < R$. In addition, by construction

$$\begin{aligned} V_1 = & C \int_{B_t} w'_1 \mathrm{d}\bar{w}' = V_2 = C \int_{B_t} w'_2 \mathrm{d}\bar{w}' = V_{12} = C \int_{B_t} w'_1 w'_2 \mathrm{d}\bar{w}' = 0, \\ V_0 = & C \int_{B_t} \mathrm{d}\bar{w}' = V_{11} = C \int_{B_t} (w'_1)^2 \mathrm{d}\bar{w}' = V_{22} = C \int_{B_t} (w'_2)^2 \mathrm{d}\bar{w}' = 1 \end{aligned} \tag{C.11}$$

with $B_t = \{\bar{w}' \big| \, |\bar{w}'| < R\}$. Putting these results together, it can be found that

$$F_\sigma^{\mathrm{out}} = K^- \, (G^-)^2 \begin{cases} 0 & \text{a)} \\ \hat{n}_{\mathsf{k}} \cdot \mathbf{u}^- & \text{b)} \\ G^- \, a_1 \, I_1^- + \hat{n}_{\mathsf{k}} \cdot \mathbf{u}^- \, I_0^- & \text{c1)} \\ -G^- \, a_1 \, I_1^- + \hat{n}_{\mathsf{k}} \cdot \mathbf{u}^- \, (V_0 - I_0^-) & \text{c2)} \end{cases} \tag{C.12}$$

$$F_\sigma^{\mathrm{in}} = K^+ \, (G^+)^2 \begin{cases} \hat{n}_{\mathsf{k}} \cdot \mathbf{u}^+ & \text{a)} \\ 0 & \text{b)} \\ -G^+ \, a_1 \, I_1^+ + \hat{n}_{\mathsf{k}} \cdot \mathbf{u}^+ \, (V_0 - I_0^+) & \text{c1)} \\ G^+ \, a_1 \, I_1^+ + \hat{n}_{\mathsf{k}} \cdot \mathbf{u}^+ \, I_0^+ & \text{c2)} \end{cases} \tag{C.13}$$

$$F_{\mu_{(j)}}^{\mathrm{out}} = K^- \, (G^-)^2 \begin{cases} 0 & \text{a)} \\ (\hat{n}_{\mathsf{k}} \cdot \mathbf{u}) \, u_j^- + \hat{n}_{\mathsf{k}j} \, (G^-)^2 & \text{b)} \\ A_{11}^{(j)} \, I_{11}^- + A_{22}^{(j)} \, I_{22}^- + A_1^{(j)} \, I_1^- + A_0^{(j)} \, I_0^- & \text{c1)} \\ A_{11}^{(j)} \, (1 - I_{11}^-) + A_{22}^{(j)} \, (1 - I_{22}^-) - A_1^{(j)} \, I_1^- + A_0^{(j)} \, (1 - I_0^-) & \text{c2)} \end{cases} \tag{C.14}$$

$$F_{\mu_{(j)}}^{\mathrm{in}} = K^+ \, (G^+)^2 \begin{cases} (\hat{n}_{\mathsf{k}} \cdot \mathbf{u}) \, u_j^+ + \hat{n}_{\mathsf{k}j} \, (G^+)^2 & \text{a)} \\ 0 & \text{b)} \\ A_{11}^{(j)} \, (1 - I_{11}^+) + A_{22}^{(j)} \, (1 - I_{22}^+) - A_1^{(j)} \, I_1^+ + A_0^{(j)} \, (1 - I_0^+) & \text{c1)} \\ A_{11}^{(j)} \, I_{11}^+ + A_{22}^{(j)} \, I_{22}^+ + A_1^{(j)} \, I_1^+ + A_0^{(j)} \, I_0^+ & \text{c2)} \end{cases} \tag{C.15}$$

with

$$\begin{aligned} a_1 &= n_1 \, m_1 + n_2 \, m_2, \quad a_2 = -n_1 \, m_2 + n_2 \, m_1, \quad A_0^{(1)} = (\hat{n}_{\mathsf{k}} \cdot \mathbf{u}) \, u_1, \\ A_1^{(1)} &= G \, [a_1 \, u_1 + (\hat{n}_{\mathsf{k}} \cdot \mathbf{u}) \, m_1], \quad A_2^{(1)} = G \, [a_2 \, u_1 - (\hat{n}_{\mathsf{k}} \cdot \mathbf{u}) \, m_2], \quad A_{11}^{(1)} = G^2 \, a_1 \, m_1, \\ A_{22}^{(1)} &= - \, G^2 \, a_2 \, m_2, \quad A_{12}^{(1)} = G^2 \, [-a_1 \, m_2 + a_2 \, m_1], \quad A_0^{(2)} = (\hat{n}_{\mathsf{k}} \cdot \mathbf{u}) \, u_2, \\ A_1^{(2)} &= G \, [a_1 \, u_2 + (\hat{n}_{\mathsf{k}} \cdot \mathbf{u}) \, m_2], \quad A_2^{(2)} = G \, [a_2 \, u_2 + (\hat{n}_{\mathsf{k}} \cdot \mathbf{u}) \, m_1], \quad A_{11}^{(2)} = G^2 \, a_1 \, m_2, \\ A_{22}^{(2)} &= G^2 \, a_2 \, m_1, \quad A_{12}^{(2)} = G^2 \, [a_1 \, m_1 + a_2 \, m_2] \end{aligned}$$

evaluated with the proper trace value as is clear from each case but not explicitly denoted. Note that the expressions are consistent: When $R_I = R$, $I_{0,1,2} = 0, I_{11}, I_{22} = 0$ and cases c1,c2 reduce to cases a,b, respectively. When $R_I = 0$ cases c1 and c2 give the same result, since $I_0 = I_{11} = I_{22} = 1/2$ and $I_1 = 4/(3\,\pi)$ and $(m_1, m_2) = (n_1, n_2)$ for case c1 and $(m_1, m_2) = -(n_1, n_2)$ for case c2.

D Shallow water waves and bores in a channel

Nonlinear wave breaking is investigated by initializing the flow with a gravity wave solution of the linearized shallow water equations:

$$\begin{aligned} h(\mathbf{x},t) &= H + A\sin(ly)\,\sin(kx+\omega t), \\ u(\mathbf{x},t) &= -\frac{A\,\mathsf{F}^{-2}k}{\omega}\,\sin(ly)\,\sin(kx+\omega t) \\ v(\mathbf{x},t) &= \frac{A\,\mathsf{F}^{-2}l}{\omega}\,\cos(ly)\,\cos(kx+\omega t) \end{aligned} \tag{D.1}$$

with amplitude A, frequency $\omega = \pm\sqrt{a^2\,(k^2+l^2)}$, $a^2 = \mathsf{F}^{-2}\,H$, and $l = (2n+1)\pi/L_y$, $k = 2\pi m/L_x$. In the simulation, the following parameters were used $L_x = L_y = 1.0$, $A = 0.1$, $\mathsf{F} = 1$, $H = 1$, $m = 2$, and $n = 0$.

Chapter 5

A discontinuous Galerkin finite element model for river bed evolution under shallow flows

The accurate representation of morphodynamic processes and the ability to propagate changes in the riverbed over a wide range of space and time scales make the design and implementation of appropriate numerical schemes challenging. In particular, requirements of accuracy and stability for medium and long term simulations are difficult to meet. In this work, the derivation, design, and implementation of a discontinuous Galerkin finite element method (DGFEM) for sediment transport and bed evolution equations are presented. Numerical morphodynamic models involve a coupling between a hydrodynamic flow solver which acts as a driving force and a bed evolution model which accounts for sediment flux and bathymetry changes. A space DGFEM is presented based on an extended approach for systems of partial differential equations with nonconservative products, in combination with two intertwined Runge-Kutta time stepping schemes for the fast hydrodynamic and slow morphodynamic components. The resulting numerical scheme is verified by comparing simulations against (semi–)analytical solutions. These include the evolution of an initially symmetric, isolated bedform; the formation and propagation of a step in a straight channel due to a sudden overload of sediment discharge; the propagation of a travelling diffusive sediment wave in a straight channel; and, the evolution of an initially flat bed in a channel with a contraction. Finally, a comparison is made between numerical model and field data of a trench excavated in the main channel of the Paraná river near Paraná City, Argentina[1].

5.1 Introduction

Quantifying the interaction between sediment transport and water flow plays an important role in many river and coastal engineering applications. Traditionally, research on

---

[1] This chapter has been submitted to *Computer Methods in Applied Mechanics and Engineering*, 2007.

river processes was primarily based on field observations and laboratory scale modelling. Laboratory scale models have been essential for understanding complex river processes and as design and verification tools, despite their high cost of construction, maintenance and operation. Field measurements are also costly and difficult to realize especially for large–scale systems. An alternative that has been growing in popularity and acceptance is mathematical and numerical modelling of river flows. River modelling is the simulation of flow conditions based on the formulation and solution of a mathematical model or a discretization thereof expressing conservation laws. Predictions of morphodynamic changes of the bed in natural channels can be analyzed by integrating in a mathematical model several modules, which are initially segregated in different physical mechanisms acting within the system according to their time response, i.e., it is a multi-scale problem. In summary, the relevant mechanisms that drive morphodynamic changes of alluvial rivers are: (i) hydrodynamics, with conservation laws of mass and momentum; (ii) bed evolution, with a conservation law for sediment mass; and, (iii) sediment transport, with predictors for the river sediment carrying capacity to sediment transport. Such a modelling system is often referred to as a *morphodynamic model*.

There are particular difficulties associated with solving hyperbolic partial differential equations, including the propagation of sediment bores or discontinuous steps in the bedform, which must be overcome by a good numerical scheme. There exist many different numerical methods to solve the system of conservation laws of water and sediment. We have chosen the discontinuous Galerkin finite element method (DGFEM) for the numerical solution of the morphodynamic model. Among other advantages, the accuracy and local nature of the numerical scheme, make it suitable for these morphodynamic problems. Furthermore, conservation of the transported quantity is satisfied on a local or elemental level. For a DGFEM discretization of hydrodynamic shallow water flows, we refer to [108]. Here we extend and refine that method to include the bed evolution as well. A partly nonconservative formulation is used that allows the application of the unified space and space–time discontinuous Galerkin discretization for hyperbolic systems of partial differential equations with nonconservative products developed in [126] to solve the entire morphodynamic model. In our case, the nonconservative product consists of the topographic terms present in the momentum equations. For the diffusive term in the bed evolution equation, we used the primal formulation of [38, 18, 28]. Additionally, we made use of advanced time stepping schemes to deal with the multiscale property of the morphodynamic problem. In summary, novel in this work are: (I) the application of the discontinuous Galerkin finite element discretization to systems with nonconservative products developed in [126] to solve the hydrodynamic and bed evolution model; (II) the implementation of the primal formulation to deal with the downhill rolling sediment term present in the sediment transport formula; (III) the verification of the results of the DGFEM with a survey of original (semi–)analytical solutions; and, (IV) the validation of these computed results against measurements.

The outline of the chapter is as follows. The governing equations and the scaling are introduced in Section 5.2. The spatial discretization of the DGFEM is introduced in Section 5.3. A time discretization is required to solve the ordinary differential equations that emerge from the spatial finite element discretization. Numerical complications may arise due to the presence of a small parameter ϵ in front of the time derivatives in the depth and momentum equations. Here, ϵ expresses the ratio of the fast hydrodynamic time scale and the slow sediment transport time scale. However, in the limit $\epsilon \to 0$, a set of coupled differential-algebraic equations emerges. The essentials of the time stepping procedure for space DGFEM are described in Section 5.3.6. In Section 5.4, the numerical scheme is verified by comparing simulations with (semi–)analytical solutions. A comparison between the numerical model and field data of a trench excavated in the main channel of the Paraná river (Argentina) and the evolution in time of flow and bed through a transition in channel width are proposed as validation tests in Section 5.5. At several instances, we also mention the intercomparison of the space DGFEM presented here with the space-time DGFEM developed in [126], and extended and refined here in our morphodynamical application. Conclusions are drawn in Section 5.6.

5.2 Governing equations and scaling

A system of hydrodynamic and bed evolution equations is introduced. Both the hydrodynamic and morphodynamic components of this system are based on a depth-average over the water column. We present these hydrodynamic and morphodynamic components first in separation before combining them.

5.2.1 Hydrodynamic shallow water equations

The shallow water equations (SWE) in nearly conservative form read (cf. [25])

$$\begin{aligned} \partial_{t^*} h^* + \boldsymbol{\nabla}^* \cdot (h^* \mathbf{u}^*) &= 0, \\ \partial_{t^*}(h^* \mathbf{u}^*) + \boldsymbol{\nabla}^* \cdot (h^* \mathbf{u}^* \mathbf{u}^*) + g \boldsymbol{\nabla}^* (h^{*2}/2) &= -g h^* \boldsymbol{\nabla}^* b^* - \boldsymbol{\tau}_b^*/\rho^*, \end{aligned} \tag{5.2.1}$$

where partial derivatives are denoted by $\partial_{t^*} = \partial/\partial t^*$ and so forth; $\boldsymbol{\nabla}^* = (\partial_{x^*}, \partial_{y^*})^T$ with transpose $(\cdot)^T$; $\mathbf{u}^*(\mathbf{x}^*, t^*) = (u^*(\mathbf{x}^*, t^*), v^*(\mathbf{x}^*, t^*))^T$ is the depth-averaged velocity as function of horizontal coordinates $\mathbf{x}^* = (x^*, y^*)^T$ and time t^*; and the free surface resides at $z^* = h^* + b^*$ with $h^*(\mathbf{x}^*, t^*)$ the total water depth and $b^*(\mathbf{x}^*, t^*)$ the elevation of the bottom topography above datum, both measured along the vertical coordinate z^*, and aligned against the direction of the acceleration of gravity of magnitude g. A relationship for the bed resistance term $\boldsymbol{\tau}_b^* = (\tau_{b_x}^*, \tau_{b_y}^*)^T$ must be specified and the classical quadratic dependency on the depth–averaged velocity is adopted:

$$\boldsymbol{\tau}_b^* = \rho^* \, C_f^* \, |\mathbf{u}^*| (u^*, v^*)^T \quad \text{with} \quad |\mathbf{u}^*| = \sqrt{u^{*2} + v^{*2}}, \tag{5.2.2}$$

with a constant friction coefficient C_f^* and constant density ρ^*.

5.2.2 Sediment continuity equation

The evolution of the bed $b^*(\mathbf{x}^*, t^*)$ is governed by a sediment continuity equation [69, 140, 145, 52]

$$\partial_{t^*} b^* + \boldsymbol{\nabla}^* \cdot \mathbf{q}_b^* = 0 \tag{5.2.3}$$

with volumetric bed load sediment flux $\mathbf{q}_b^*(\mathbf{x}^*, t^*) = (q_{b_x}^*, q_{b_y}^*)^T$ through a vertical cross section of the bed. We adopt a simple power-law form of transport for noncohesive sediment of uniform grain size [69] and include the downslope gravitational transport component that generalizes ideas going back to the earlier work of [49] to close (5.2.3) with

$$\mathbf{q}_b^* = \alpha^* |\mathbf{u}^*|^\beta \left(\mathbf{u}^*/|\mathbf{u}^*| - \kappa^* \boldsymbol{\nabla}^* b^* \right), \tag{5.2.4}$$

where α^* is a proportionality factor including the bed material porosity, β a constant, and the diffusive term with $\kappa^* \boldsymbol{\nabla}^* b^*$ is a bed slope correction term accounting for the preferred downslope transport of sediment with nondimensional proportionality constant κ^*. For various slowly varying alluvial flows, it has been deduced that $1 < \beta \leq 3$. However, larger values of β may be attained when the bed is covered by dunes. Most of the empirical bed load sediment transport functions available are given in the form of (5.2.4) by taking α^* as constant [141] and with $\mathbf{q}_b^*$ depending monotonically on the flow speed.

Finally, the system (5.2.1)–(5.2.4) is considered in a bounded domain $\Omega \subset \mathbb{R}^2$. It is completed with initial conditions $h^*(\mathbf{x}^*, 0), \mathbf{u}^*(\mathbf{x}^*, 0)$, and $b^*(\mathbf{x}, 0)$, and boundary conditions such as in- and outflow, and/or slip flow along solid walls. The sediment transport equation emerges as a mixed hyperbolic and parabolic equation, and extra boundary conditions are required on b^* and the sediment flux. Relevant boundary conditions will be discussed later in the applications.

5.2.3 Scaling

It is convenient to treat the governing equations in nondimensional form for computational reasons and to clarify the coupling of the hydrodynamics to the dynamics of the bed. Sediment transport of the bed occurs on a transport time scale much longer than the flow time scale (cf. Hall [106]).

First, we consider a simple solution to the system (5.2.1) and (5.2.3). Uniform one-dimensional flow down an inclined plane along x^* with constant slope S_0 satisfies

$$\begin{aligned} \mathbf{u}^*(\mathbf{x}^*, t^*) =& (u_0^*, 0)^T, \quad \tau_b^* = (\tau_{b_0}^*, 0)^T, \quad \mathbf{q}_b^*(\mathbf{x}^*, t^*) = (q_{b0}^*, 0)^T, \\ h^*(\mathbf{x}^*, t^*) =& h_0^*, \quad u_0^* = \sqrt{g h_0^* S_0 / C_f^*}, \quad q_0^* = h_0^* \, u_0^*, \\ q_{b0}^* =& \alpha^* \, u_0^{*\beta}, \quad \tau_{b0}^* = \rho^* \, C_f^* \, u_0^{*2}, \end{aligned} \tag{5.2.5}$$

given the water discharge q_0^*, sediment flux q_{b0}^*, and constant friction coefficient C_f^*. This solution suggests the use of the following scaling

$$\begin{aligned} \mathbf{x} =& \mathbf{x}^*/l_0^*, \quad t = t^*/t_0^*, \quad h = h^*/h_0^*, \quad b = b^*/h_0^*, \quad \mathbf{u} = \mathbf{u}^*/u_0^*, \\ \mathbf{q}_b =& \mathbf{q}_b^*/(\alpha^* \, u_0^{*\beta}), \quad \text{and} \quad t_0^* = h_0^* \, l_0^*/q_{b0}^*, \end{aligned} \tag{5.2.6}$$

where l_0^*, t_0^*, h_0^* and u_0^* are characteristic length, time, depth and velocity scales, respectively. We have chosen t_0^* to be the sediment transport time scale associated with the erosion and deposition of sediment.

Substitution of the above scaling (5.2.6) into system (5.2.1)–(5.2.4) yields the nondimensional system

$$\epsilon\,\partial_t h + \boldsymbol{\nabla}\cdot(h\mathbf{u}) = 0, \tag{5.2.7a}$$

$$\epsilon\,\partial_t(h\mathbf{u}) + \boldsymbol{\nabla}\cdot(h\mathbf{u}\mathbf{u}) + \mathsf{F}^{-2}\boldsymbol{\nabla}(h^2/2) = -\mathsf{F}^{-2}h\,\boldsymbol{\nabla}b - C_f\,\mathbf{u}\,|\mathbf{u}|, \tag{5.2.7b}$$

$$\partial_t b + \boldsymbol{\nabla}\cdot\mathbf{q}_b = 0, \tag{5.2.7c}$$

with the nondimensional sediment flux

$$\mathbf{q}_b = |\mathbf{u}|^{\beta}\left(\mathbf{u}/|\mathbf{u}| - \kappa\boldsymbol{\nabla}b\right), \tag{5.2.7d}$$

where $\mathbf{q}_b = (q_{b_x}, q_{b_y})^T$ and $\boldsymbol{\nabla} = (\partial_x, \partial_y)^T$. In this system, the following parameters have emerged: the nondimensional friction coefficient $C_f = \gamma\,C_f^* = (l_0^*/h_0^*)\,C_f^*$, the ratio between the flow velocity and surface gravity-wave speed or Froude number $\mathsf{F} = u_0^*/\sqrt{g\,h_0^*}$, a scaled $\kappa = \kappa^*\,h_0^*/l_0^*$, and the ratio between sediment and hydrodynamic discharge $\epsilon = \alpha^* u_0^{*\beta}/u_0^* h_0^* = q_{b0}^*/q_0^*$.

Most rivers transport far less sediment than water, so the condition $\epsilon \ll 1$ prevails even during floods. The parameter ϵ typically attains values in the range 10^{-3}–10^{-6} [127], which at leading order in ϵ makes the hydrodynamic equations stationary and algebraic. For $\epsilon \ll 1$ the hydrodynamic equations are therefore nearly *quasi-stationary* on the sediment time scale.

5.3 Space discontinuous Galerkin discretization

5.3.1 Concise formulation

To facilitate the discretization, the scaled system (5.2.7a)–(5.2.7d) is written concisely as follows

$$A_{ir}\,\partial_t U_r + F_{ik,k} + G_{ikr}\,U_{r,k} - \big(T_i\,\delta_{ij}\,U_{j,k}\big)_{,k} = S_i, \tag{5.3.1}$$

for $i, j, r = 1, 2, 3, 4$ and $k = 1, 2$ with:

$$U = \begin{bmatrix} h \\ hu \\ hv \\ b \end{bmatrix}, \quad A = \begin{bmatrix} \epsilon & 0 & 0 & 0 \\ 0 & \epsilon & 0 & 0 \\ 0 & 0 & \epsilon & 0 \\ 0 & 0 & 0 & 1 \end{bmatrix}, \tag{5.3.2}$$

$$F(U) = \begin{bmatrix} hu & hv \\ hu^2 + \mathsf{F}^{-2}h^2/2 & huv \\ huv & hv^2 + \mathsf{F}^{-2}h^2/2 \\ |\mathbf{u}|^{\beta-1}u & |\mathbf{u}|^{\beta-1}v \end{bmatrix}, \tag{5.3.3}$$

$$G_1(U) = \begin{bmatrix} 0 & 0 & 0 & 0 \\ 0 & 0 & 0 & \mathsf{F}^{-2}h \\ 0 & 0 & 0 & 0 \\ 0 & 0 & 0 & 0 \end{bmatrix}, \qquad G_2(U) = \begin{bmatrix} 0 & 0 & 0 & 0 \\ 0 & 0 & 0 & 0 \\ 0 & 0 & 0 & \mathsf{F}^{-2}h \\ 0 & 0 & 0 & 0 \end{bmatrix}, \tag{5.3.4}$$

$T_1 = T_2 = T_3 = 0$, and $T = T_4 = \kappa\,|\mathbf{u}|^\beta$, and

$$S_1(U) = \begin{bmatrix} 0 \\ -C_f|\mathbf{u}|u \\ -C_f|\mathbf{u}|v \\ 0 \end{bmatrix}. \tag{5.3.5}$$

Derivatives in space are denoted by the comma subscript notation $(\cdot)_{,k} = \partial_{x_k}(\cdot)$ with $k = 1, 2$ and $\mathbf{x} = (x_1, x_2)^T$. The nonconservative term in (5.3.1) is caused solely by the topographic term.

The weak formulation starts with a first-order reformulation of the system (5.3.1)

$$A_{ir}\partial_t U_r + F_{ik,k} + G_{ikr}\,U_{r,k} - \delta_{i4}\Theta_{k,k} = S_i \qquad \text{for } i, r = 1, 2, 3, 4 \tag{5.3.6a}$$

$$\Theta_k = T\,U_{4,k} \quad \text{and} \quad k = 1, 2. \tag{5.3.6b}$$

5.3.2 Space elements, function space and operators

The flow domain $\Omega \in \mathbb{R}^2$ is a bounded area which in turn is partitioned into N_{el} elements K_k. It consists of segments $\partial\Omega_s$ demarcating a fixed boundary and open boundary segments $\partial\Omega_o$ such that $\partial\Omega = \partial\Omega_s \cup \partial\Omega_o$. The tessellation of the domain Ω is

$$\mathcal{T}_h = \left\{ K_\mathsf{k} | \bigcup_{\mathsf{k}=1}^{N_{el}} \bar{K}_\mathsf{k} = \bar{\Omega}_\mathsf{h} \text{ and } K_\mathsf{k} \cap K_{\mathsf{k}'} = 0 \text{ if } \mathsf{k} \neq \mathsf{k}', 1 \leq \mathsf{k}, \mathsf{k}' \leq N_{el} \right\}, \tag{5.3.7}$$

such that $\Omega_\mathsf{h} \to \Omega$ as $\mathsf{h} \to 0$ with h the smallest radius of all circles completely containing the elements $K_\mathsf{k} \in \mathcal{T}_h$. Here $\bar{K}_\mathsf{k}$ is the closure of K_k (and likewise for $\bar{\Omega}$). A reference element $\hat{K}$ is introduced with the mapping

$$F_{K_\mathsf{k}} : \hat{K} \mapsto K_\mathsf{k} : \bar{\xi} \mapsto \mathbf{x} := \sum_j \mathbf{x}_j\,\chi_j(\bar{\xi}), \tag{5.3.8}$$

where $\bar{\xi} = (\xi_1, \xi_2)$ are the reference coordinates, $\mathbf{x}_j$ are the coordinates of the local nodes of the element, with $j = 1, \ldots, N_\mathsf{k}$, $\chi_j(\bar{\xi})$ the standard shape functions used in finite elements, and N_k the number of nodes in element k. For quadrilateral elements $N_\mathsf{k} = 4$ and for triangular elements $N_\mathsf{k} = 3$. In general, the element boundary ∂K_k is connected through faces $\mathcal{S}$ either to its neighboring elements or to the boundary of the domain.

In each reference element $\hat{K}$ a set of polynomials of order p is defined represented as $P_k(\hat{K})$ with $k = 0, \ldots, n_p - 1$ for positive integers p and n_p. For the discontinuous Galerkin discretization of (5.3.6a) we define the space V_h of discontinuous test functions

$$V_h = \left\{ V \in (L^2(\Omega_h))^4 \,\middle|\, \forall K_\mathsf{k} \in \mathcal{T}_h : V|_{K_\mathsf{k}} \circ F_K \in (\mathcal{P}_{p_k}(K_\mathsf{k}))^4 \right\}, \tag{5.3.9}$$

with $\mathcal{P}_{p_k}(K_\mathsf{k})$ the usual space of polynomials on K_k of degree equal to or less than $p_k \leq p$ and $L^2(\Omega_h)$ the space of square integrable functions on Ω_h. For the discontinuous Galerkin discretization of (5.3.6b) we define the space W_h of discontinuous test vector functions

$$W_h = \left\{ W \in (L^2(\Omega_h))^{n_s \times d} \,\middle|\, \forall K_\mathsf{k} \in \mathcal{T}_h : W|_{K_\mathsf{k}} \circ F_{K_\mathsf{k}} \in (\mathcal{P}_{p_k}(K_\mathsf{k}))^{n_s \times d} \right\} \tag{5.3.10}$$

for dimension $d = 2$. These definitions are such that for $n_s = 4$ we have $\boldsymbol{\nabla} V_h \subset W_h$.

For a scalar function $V \in V_h$ and vector function $W \in W_h$ the traces on an element boundary ∂K are defined as

$$V^{\mathsf{L}} = \lim_{\varepsilon \downarrow 0} V(\mathbf{x} - \varepsilon n^{\mathsf{L}}) \quad \text{and} \quad W^{\mathsf{L}} = \lim_{\varepsilon \downarrow 0} W(\mathbf{x} - \varepsilon n^{\mathsf{L}}) \tag{5.3.11}$$

with n^{L} the unit outward normal vector of the boundary ∂K, where K_{L} and K_{R} are the elements left or right of a face $\mathcal{S}$. Faces $\mathcal{S}$ of elements are either internal faces $\mathcal{S}_I$ or boundary faces $\mathcal{S}_B$. The averages or means of a scalar function $V \in V_h$ on an internal and boundary face are

$$\{\!\{V\}\!\} = (V^{\mathsf{L}} + V^{\mathsf{R}})/2 \quad \text{on} \quad \mathcal{S}_I, \qquad \{\!\{V\}\!\} = V^{\mathsf{L}} \quad \text{on} \quad \mathcal{S}_B \tag{5.3.12}$$

such that at a boundary face we always take the interior or left value. Likewise, for a vector function $W \in W_h$ the mean values are

$$\{\!\{W\}\!\} = (W^{\mathsf{L}} + W^{\mathsf{R}})/2 \quad \text{on} \quad \mathcal{S}_I, \qquad \{\!\{W\}\!\} = W^{\mathsf{L}} \quad \text{on} \quad \mathcal{S}_B. \tag{5.3.13}$$

The jumps of a scalar function $V \in V_h$ on an internal and boundary face are

$$[\![V]\!]_k = V^{\mathsf{L}}\, n_k^{\mathsf{L}} + V^{\mathsf{R}}\, n_k^{\mathsf{R}} \quad \text{on} \quad \mathcal{S}_I, \qquad [\![V]\!]_k = V^{\mathsf{L}}\, n_k^{\mathsf{L}} \quad \text{on} \quad \mathcal{S}_B \tag{5.3.14}$$

such that at a boundary face we always take the interior left value, and where n^{L} and n^{R} are the outward normal vectors of elements K_{L} and K_{R} with $n^{\mathsf{R}} = -n^{\mathsf{L}}$. Likewise, for a vector function $W \in \mathsf{W}_h$ the jumps are

$$[\![W]\!]_k = W_k^{\mathsf{L}} n_k^{\mathsf{L}} + W_k^{\mathsf{R}} n_k^{\mathsf{R}} \quad \text{on} \quad \mathcal{S}_I, \qquad [\![W]\!]_k = W_k^{\mathsf{L}} n_k^{\mathsf{L}} \quad \text{on} \quad \mathcal{S}_B. \tag{5.3.15}$$

A useful property for $V \in V_h$ and $W \in W_h$ on internal faces is

$$[\![V_i W_k]\!]_k = \{\!\{V_i\}\!\}[\![W_k]\!]_k + [\![V_i]\!]_k \{\!\{W_k\}\!\}. \tag{5.3.16}$$

Hereafter, we will often combine the sum over internal and boundary faces by defining a suitable ghost value U^{R} at the boundary faces.

In next section, we will also use the following relation for the element boundary integrals which occur in the weak formulation

$$\sum_{K_{\mathsf{k}}} \int_{\mathcal{S}} V_i^{\mathsf{L}}\, W_k^{\mathsf{L}}\, n_k^{\mathsf{L}}\, \mathrm{d}\mathcal{S} = \sum_{\mathcal{S} \in \mathcal{S}_I} \int_{\mathcal{S}} [\![V_i\, W_k]\!]_k\, \mathrm{d}\mathcal{S} + \sum_{\mathcal{S} \in \mathcal{S}_I} \int_{\mathcal{S}} V_i^{\mathsf{L}}\, W_k^{\mathsf{L}}\, n_k^{\mathsf{L}}\, \mathrm{d}\mathcal{S}. \tag{5.3.17}$$

On internal faces, the following relations hold

$$\{\!\{\{\!\{F\}\!\}\}\!\} = \{\!\{F\}\!\} \quad \text{and} \quad [\![\{\!\{F\}\!\}]\!]_k = 0. \tag{5.3.18}$$

5.3.3 Weak formulation

A flux formulation is obtained after multiplying (5.3.6a) by an arbitrary test function $V \in \mathsf{V}_h$, using the non-conservative weak formulation in [126] (their expression (A.9)) for the hyperbolic terms, integrating the diffusive term by parts, and summing over all elements

$$\begin{aligned}&\sum_{K_\mathsf{k}}\int_{K_\mathsf{k}}\Big(V_i\,A_{ir}\,\partial_t U_r - V_{i,k}\,F_{ik} + V_i\,G_{ikr}\,U_{r,k} + V_{i,k}\,\delta_{i4}\,\Theta_k -\\ &V_i\,S_i\Big)\mathrm{d}K + \sum_{\mathcal{S}}\int_{\mathcal{S}}\Big((V_i^\mathsf{L} - V_i^\mathsf{R})\,(\{\!\{F_{ik}\}\!\}\,n_k^\mathsf{L} + \tilde{H}_i^{nc}) +\\ &\{\!\{V_i\}\!\}\int_0^1 G_{ikr}\,\big(\phi(\tau;U^\mathsf{L},U^\mathsf{R})\big)\,\frac{\partial\phi_r}{\partial\tau}(\tau;U^\mathsf{L},U^\mathsf{R})\,\mathrm{d}\tau\,n_k^\mathsf{L}\Big)\mathrm{d}\mathcal{S}\\ &-\sum_{K_\mathsf{k}}\int_{\partial K} V_i^\mathsf{L}\,\delta_{i4}\,\Theta_k^\mathsf{L}\,n_k^\mathsf{L}\,\mathrm{d}\mathcal{S} = 0,\end{aligned} \tag{5.3.19}$$

with $\mathrm{d}K$ an elemental area and $\mathrm{d}\mathcal{S}$ a line element on a face $\mathcal{S}$, $\tilde{H}_i^{nc}$ a stabilizing flux term in the non-conservative treatment, defined later. A linear path $\phi(\tau;U^\mathsf{L},U^\mathsf{R}) = U^\mathsf{L} + \tau\,(U^\mathsf{R} - U^\mathsf{L})$ connecting the left and right states across the discontinuity is adopted. The integrals containing the linear path are either evaluated analytically or with two-point Gauss quadrature. For details on the nonconservative discontinuous Galerkin formulation for the hyperbolic part, we refer to [126].

5.3.4 The auxiliary variable

Our aim is to eliminate in (5.3.19) the auxiliary variable Θ_k for the interior elements. Storage space is thus saved. Multiplication of (5.3.6b) by arbitrary test functions $W \in W_h$, integration by parts back and forth, and summation over the elements yields

$$\sum_{K_\mathsf{k}}\int_{K_\mathsf{k}} W_k\,(\Theta_k - T\,U_{4,k})\,\mathrm{d}K - \sum_{K_\mathsf{k}}\int_{\partial K} W_k^\mathsf{L}\,T^\mathsf{L}\,(\hat{U}_4 - U_4^\mathsf{L})\,n_k^\mathsf{L}\,\mathrm{d}\mathcal{S} = 0, \tag{5.3.20}$$

where we introduced a numerical flux $\hat{U}_4$ only in the forward integration by parts. The boundary term in (5.3.20) is analyzed again by changing the elemental summation to a face summation, and the use of relations (5.3.16) and (5.3.18), to obtain

$$\begin{aligned}\sum_{K_\mathsf{k}}\int_{\partial K} W_k^\mathsf{L}\,T^\mathsf{L}\,(\hat{U}_4 - U_4^\mathsf{L})\,n_k^\mathsf{L}\,\mathrm{d}\mathcal{S} = &\sum_{\mathcal{S}\in\mathcal{S}_I}\int_{\mathcal{S}} [\![W_k\,T\,(\hat{U}_4 - U_4)]\!]_k\,\mathrm{d}\mathcal{S} +\\ &\sum_{\mathcal{S}\in\mathcal{S}_B}\int_{\mathcal{S}} W_k^\mathsf{L}\,T^\mathsf{L}\,(\hat{U}_4 - U_4^\mathsf{L})\,n_k^\mathsf{L}\,\mathrm{d}\mathcal{S}.\end{aligned} \tag{5.3.21}$$

We now introduce the numerical flux

$$\hat{U}_4 = \left\{\begin{array}{cl} \{\!\{U_4\}\!\} & \text{at } \mathcal{S}_I \\ U_4^B & \text{at } \mathcal{S}_B \end{array}\right. . \tag{5.3.22}$$

With this choice for the numerical flux at the internal faces and by using relations (5.3.17) and (5.3.18), we obtain: $[\![W_k\, T\,(\hat{U}_4 - U_4)]\!]_k = -\{\!\{W_k\, T\}\!\}[\![U_4]\!]_k$. Hence, (5.3.20) becomes

$$\begin{aligned}\sum_{K_{\mathsf{k}}}\int_{K_{\mathsf{k}}} W_k\,(\Theta_k - T\,U_{4,k})\,\mathrm{d}K = &-\sum_{\mathcal{S}\in\mathcal{S}_I}\int_{\mathcal{S}}\{\!\{W_k\,T\}\!\}[\![U_4]\!]_k\,\mathrm{d}\mathcal{S}\\ &-\sum_{\mathcal{S}\in\mathcal{S}_B}\int_{\mathcal{S}} W_k^{\mathsf{L}}\,T^{\mathsf{L}}\,(U_4^{\mathsf{L}} - U_4^{B})\,n_k^{\mathsf{L}}\,\mathrm{d}\mathcal{S}.\end{aligned} \tag{5.3.23}$$

To obtain an explicit expression for the auxiliary variable, we define a *global lifting operator* $\mathcal{R}\in W_h$, which is defined in the weak sense as: find an $\mathcal{R}\in W_h$ such that for all $W\in W_h$

$$\sum_{K_{\mathsf{k}}}\int_{K_{\mathsf{k}}} W_k\,\mathcal{R}_k\mathrm{d}K = \sum_{\mathcal{S}_I}\int_{\mathcal{S}}\{\!\{T\,W_k\}\!\}\,[\![U_4]\!]_k\,\mathrm{d}\mathcal{S} + \sum_{\mathcal{S}_B}\int_{\mathcal{S}} W_k^{\mathsf{L}}\,T^{\mathsf{L}}\,(U_4^{\mathsf{L}} - U_4^{B})\,n_k^{\mathsf{L}}\,\mathrm{d}\mathcal{S}. \tag{5.3.24}$$

Details on the solvability of (5.3.24) are given in Appendix A. Finally, we apply (5.3.24) to expression (5.3.23) to obtain a weak expression for the auxiliary variable:

$$\sum_{K_{\mathsf{k}}}\int_{K_{\mathsf{k}}} W_k\,(\Theta_k - T\,U_{4,k})\,\mathrm{d}K = -\sum_{K_{\mathsf{k}}}\int_{K_{\mathsf{k}}} W_k\,\mathcal{R}_k\mathrm{d}K \tag{5.3.25}$$

As a result of the above manipulations in (5.3.25) and the arbitrariness of W_k, our aim to determine Θ_k has been reached. From (5.3.25), we find that

$$\Theta_k = T\,U_{4,k} - \mathcal{R}_k, \tag{5.3.26}$$

almost everywhere in Ω_{h}.

5.3.5 Primal formulation

The primal formulation can be obtained using the expression (5.3.25). Since $\boldsymbol{\nabla} V_h \subset W_h$, the special case $W_k = V_{4,k}$ can be considered in (5.3.25), and the auxiliary variable Θ can be replaced in the element integral of (5.3.19). Therefore,

$$\sum_{K_{\mathsf{k}}}\int_{K_{\mathsf{k}}} V_{4,k}\,\Theta_k\,\mathrm{d}K = \sum_{K_{\mathsf{k}}}\int_{K_{\mathsf{k}}} V_{4,k}\,(TU_{4,k} - \mathcal{R}_k)\,\mathrm{d}K. \tag{5.3.27}$$

The element boundary terms in (5.3.19) can be treated as follows

$$\begin{aligned}\sum_{K_{\mathsf{k}}}\int_{\partial K} V_i^{\mathsf{L}}\,\delta_{i4}\,\Theta_k^{\mathsf{L}}\,n_k^{\mathsf{L}}\,\mathrm{d}\mathcal{S} &= \sum_{\mathcal{S}\in\mathcal{S}_I}\delta_{i4}\int_{\mathcal{S}}[\![V_i\,\Theta_k]\!]_k\,\mathrm{d}\mathcal{S} + \sum_{\mathcal{S}\in\mathcal{S}_B}\delta_{i4}\int_{\mathcal{S}} V_i^{\mathsf{L}}\,\Theta_k^{\mathsf{L}}\,n_k^{\mathsf{L}}\,\mathrm{d}\mathcal{S}\\ &= \sum_{\mathcal{S}\in\mathcal{S}_I}\delta_{i4}\int_{\mathcal{S}}\{\!\{V_i\}\!\}[\![\Theta_k]\!]_k + [\![V_i]\!]_k\{\!\{\Theta_k\}\!\}\,\mathrm{d}\mathcal{S} +\\ &\quad\sum_{\mathcal{S}\in\mathcal{S}_B}\delta_{i4}\int_{\mathcal{S}} V_i^{\mathsf{L}}\,\Theta_k^{\mathsf{L}}\,n_k^{\mathsf{L}}\,\mathrm{d}\mathcal{S}\end{aligned} \tag{5.3.28}$$

$$= \sum_{\mathcal{S}\in\mathcal{S}_I}\delta_{i4}\int_{\mathcal{S}}[\![V_i]\!]_k\{\!\{\Theta_k\}\!\}\,\mathrm{d}\mathcal{S} + \sum_{\mathcal{S}\in\mathcal{S}_B}\delta_{i4}\int_{\mathcal{S}} V_i^{\mathsf{L}}\,\Theta_k^{\mathsf{L}}\,n_k^{\mathsf{L}}\,\mathrm{d}\mathcal{S}, \tag{5.3.29}$$

where we used relations (5.3.16)-(5.3.17) and invoked continuity of the flux such that $[\![\Theta_k]\!]_k = 0$ on internal faces. The average $\{\!\{\Theta_k\}\!\}$ is defined as:

$$\{\!\{\Theta_k\}\!\} = \left\{ \begin{array}{ll} \{\!\{T\, U_{4,k} - \eta\, \mathcal{R}_k^{\mathcal{S}}\}\!\} & \text{on } \mathcal{S}_I \\ T^B\, U^B_{4,k} - \eta\, \mathcal{R}_k^{\mathcal{S}} & \text{on } \mathcal{S}_B \end{array} \right. , \tag{5.3.30}$$

where, to reduce the width of the stencil, a *local lifting operator* $\mathcal{R}_k^{\mathcal{S}}$ was introduced satisfying

$$\sum_{K_{\mathsf{k}}} \int_{K_{\mathsf{k}}} W_k\, \mathcal{R}_k^{\mathcal{S}}\, \mathrm{d}K = \left\{ \begin{array}{ll} \int_{\mathcal{S}} \{\!\{T\, W_k\}\!\}\, [\![U_4]\!]_k\, \mathrm{d}\mathcal{S} & \text{on } \mathcal{S}_I \\ \int_{\mathcal{S}} W_k^{\mathsf{L}}\, T^{\mathsf{L}}\, (U_4^{\mathsf{L}} - U_4^B)\, n_k^{\mathsf{L}}\, \mathrm{d}\mathcal{S} & \text{on } \mathcal{S}_B \end{array} \right. \tag{5.3.31}$$

for all $W_k \in W_h$ with $\eta > 0$ a stabilization constant. In all simulations we use $\eta = 4$.

Substitution of (5.3.26), (5.3.29), and (5.3.30) into (5.3.19) yields the final weak formulation

$$\begin{aligned} &\sum_{K_{\mathsf{k}}} \int_{K_{\mathsf{k}}} \Big(V_i\, A_{ir}\, \partial_t U_r - V_{i,k}\, F_{ik} + V_i\, G_{ikr}\, U_{r,k} + \\ &V_{i,k}\, \delta_{i4}\, (T\, U_{4,k} - \mathcal{R}_k) - V_i\, S_i \Big)\, \mathrm{d}K + \sum_{\mathcal{S}} \int_{\mathcal{S}} \Big((V_i^{\mathsf{L}} - V_i^{\mathsf{R}})\, (\{\!\{F_{ik}\}\!\}\, n_k^{\mathsf{L}} + \tilde{H}_i^{nc}) + \\ &\{\!\{V_i\}\!\} \int_0^1 G_{ikr}\, \big(\phi(\tau; U^{\mathsf{L}}, U^{\mathsf{R}})\big)\, \frac{\partial \phi_r}{\partial \tau}(\tau; U^{\mathsf{L}}, U^{\mathsf{R}})\, \mathrm{d}\tau\, n_k^{\mathsf{L}} \Big)\, \mathrm{d}\mathcal{S} - \\ &\qquad \sum_{\mathcal{S}_I} \int_{\mathcal{S}} \delta_{i4}\, [\![V_i]\!]_k\, \{\!\{T\, U_{4,k} - \eta \mathcal{R}_k^{\mathcal{S}}\}\!\}\, \mathrm{d}\mathcal{S} \\ &\qquad - \sum_{\mathcal{S}_B} \int_{\mathcal{S}} \delta_{i4}\, V_i^{\mathsf{L}}\, (T^B\, U^B_{4,k} - \eta\, \mathcal{R}_k^{\mathcal{S}})\, n_k^{\mathsf{L}}\, \mathrm{d}\mathcal{S} = 0. \end{aligned} \tag{5.3.32}$$

For conservative systems, the flux $(\{\!\{F_{ik}\}\!\}\, n_k^{\mathsf{L}} + \tilde{H}_i^{nc})$ is usually combined into one conservative, numerical flux at the element faces, such as the HLLC flux used before in [108] for the hydrodynamic part.

The nonconservative stabilizing flux vector $\tilde{H}_i^{nc}(U^{\mathsf{L}}, U^{\mathsf{R}}, n_k^{\mathsf{L}})$ is deduced by Rhebergen *et al.* [126] to be

$$\tilde{H}_i^{nc} = \left\{ \begin{array}{l} \frac{1}{2}\, [\![F_{ik}]\!]_k + \frac{1}{2} \int_0^1 G_{ikr}\, \big(\phi(\tau; U^{\mathsf{R}}, U^{\mathsf{L}})\big)\, \frac{\partial \phi_r}{\partial \tau}(\tau; U^{\mathsf{R}}, U^{\mathsf{L}})\, \mathrm{d}\tau\, n_k^{\mathsf{L}} \\ \qquad \text{if } S_{\mathsf{L}} > 0, \\ \frac{1}{2}\, \big(S_{\mathsf{R}} \bar{U}_i^* + S_{\mathsf{L}} \bar{U}_i^* - S_{\mathsf{L}}\, U_i^{\mathsf{L}} - S_{\mathsf{R}}\, U_i^{\mathsf{R}}\big), \qquad \text{if } S_{\mathsf{L}} < 0 < S_{\mathsf{R}}, \\ -\frac{1}{2}\, [\![F_{ik}]\!]_k + \frac{1}{2} \int_0^1 G_{ikr}\, \big(\phi(\tau; U^{\mathsf{L}}, U^{\mathsf{R}})\big)\, \frac{\partial \phi_r}{\partial \tau}(\tau; U^{\mathsf{L}}, U^{\mathsf{R}})\, \mathrm{d}\tau\, n_k^{\mathsf{L}}, \\ \qquad \text{if } S_{\mathsf{R}} < 0. \end{array} \right. \tag{5.3.33}$$

The expression for the star state solution $\bar{U}_i^*$ in (5.3.33) is:

$$\begin{aligned} \bar{U}_i^* =& \frac{S_{\mathsf{R}} U_i^{\mathsf{R}} - S_{\mathsf{L}} U_i^{\mathsf{L}}}{S_{\mathsf{R}} - S_{\mathsf{L}}} - \frac{(F_{ik}^{\mathsf{R}} - F_{ik}^{\mathsf{L}})\, n_k^{\mathsf{L}}}{S_{\mathsf{R}} - S_{\mathsf{L}}} \\ & - \frac{1}{S_{\mathsf{R}} - S_{\mathsf{L}}} \int_0^1 G_{ikr}\, \big(\phi(\tau; U^{\mathsf{L}}, U^{\mathsf{R}})\big)\, \frac{\partial \phi_r}{\partial \tau}(\tau; U^{\mathsf{L}}, U^{\mathsf{R}})\, \mathrm{d}\tau\, n_k^{\mathsf{L}}. \end{aligned} \tag{5.3.34}$$

The left and right wave speeds are S_L and S_R, respectively. These are determined by taking the smallest and largest of the four real eigenvalues of the hyperbolic part of the system (5.2.7).

The eigenvalues used follow from the matrix $(\partial F_{ik}/\partial U_r + G_{ikr})\, n_k^\mathsf{L}$ for the case $\epsilon = 1$ valid in (pseudo-)time, see §5.3.6. The hyperbolic part of the corresponding system in the direction $\hat{x}$ normal to a face can be written as

$$\begin{aligned}
&\partial_t(hu) + \partial_{\hat{x}}(h\,u\,q + \mathsf{F}^{-2}\,h^2\,n_x/2) + \mathsf{F}^{-2}\,h\,n_x\,\partial_{\hat{x}} b = 0,\\
&\partial_t(hv) + \partial_{\hat{x}}(h\,v\,q + \mathsf{F}^{-2}\,h^2\,n_y/2) + \mathsf{F}^{-2}\,h\,n_y\,\partial_{\hat{x}} b = 0,\\
&\qquad \partial_t h + \partial_{\hat{x}}(h\,q) = 0, \qquad \partial_t b + \partial_{\hat{x}}(|\mathbf{u}|^{\beta-1}\,q) = 0
\end{aligned} \tag{5.3.35}$$

with $q = n_x\,u + n_y\,v$ and $n_k^\mathsf{L} = (n_x, n_y)^T$. For the eigenvalue analysis it is easier to rewrite (5.3.35) as

$$\begin{aligned}
\partial_t h + \partial_{\hat{x}}(h\,q) &= 0, \qquad \partial_t u + q\,\partial_{\hat{x}} u + \mathsf{F}^{-2}\,n_x\,\partial_{\hat{x}}(h+b) = 0,\\
\partial_t b + \partial_{\hat{x}}(|\mathbf{u}|^{\beta-1}\,q) &= 0, \qquad \partial_t v + q\,\partial_{\hat{x}} v + \mathsf{F}^{-2}\,n_y\,\partial_{\hat{x}}(h+b) = 0.
\end{aligned} \tag{5.3.36}$$

The eigenvalues λ corresponding to the system (5.3.36) follow from the (approximate) polynomial

$$\begin{aligned}
0 &= \begin{vmatrix}
q-\lambda & h\,n_x & h\,n_y & 0\\
\mathsf{F}^{-2}\,n_x & q-\lambda & 0 & \mathsf{F}^{-2}\,n_x\\
\mathsf{F}^{-2}\,n_y & 0 & q-\lambda & \mathsf{F}^{-2}\,n_y\\
0 & n_x\,d & n_y\,d & -\lambda
\end{vmatrix}\\
&= (\lambda - q)\left(\lambda^3 - 2\,q\,\lambda^2 + \lambda\left(q^2 - \mathsf{F}^{-2}\,(d+h)\right) + \mathsf{F}^{-2}\,q\,d\right)
\end{aligned} \tag{5.3.37}$$

with approximation $d = \beta\,|\mathbf{u}|^{\beta-1}$ based on the one-dimensional problem, cf. [144]. The cubic polynomial has real eigenvalues provided its determinant $D = Q^3 + R^2 < 0$, hence if $Q^3 < -R^2 < 0$, which is the case since

$$Q = -\left(q^2 + 3\,\mathsf{F}^{-2}\,(h+d)\right)/9 < 0$$

as $h > 0, d > 0$ and $\mathsf{F}^{-2} > 0$ with

$$R = \frac{-18\,q\left(-\mathsf{F}^{-2}(h+d) + q^2\right) - 27\,\mathsf{F}^{-2}\,q\,d + 16\,q^3}{54}. \tag{5.3.38}$$

The four approximate eigenvalues are

$$\begin{aligned}
\lambda &= q, \quad \lambda = 2\,\sqrt{-Q}\,\cos(\theta/3) + 2\,q/3,\\
\lambda &= 2\,\sqrt{-Q}\,\cos(\theta/3 + 2\,\pi/3) + 2\,q/3 \quad \text{and}\\
\lambda &= 2\,\sqrt{-Q}\,\cos(\theta/3 + 4\,\pi/3) + 2\,q/3,
\end{aligned} \tag{5.3.39}$$

with $\theta = \cos^{-1}(R/\sqrt{-Q^3})$. Finally, the algebraic system corresponding to the weak formulation (5.3.32) and details on the global and local lifting operators $\mathcal{R}_k$ and $\mathcal{R}_k^\mathcal{S}$ defined in (5.3.24) and (5.3.31) are given in Appendix A.

The numerical flux in the weak formulation (5.3.32)–(5.3.34) reduces to the HLL numerical flux when the topography is constant. Rest flow stays at rest even for variable bottom topography as was shown in [126].

5.3.6 Time stepping method and solver

A time discretization is required to solve the ordinary differential equations that emerge from the spatial finite element discretization. Numerical complications may arise due to the presence of a small parameter ϵ in front of the time derivatives in the depth and momentum equations. However, at leading order, in the limit $\epsilon \to 0$ a coupled differential-algebraic system emerges. We therefore use a time stepping scheme for solving the system in the limit $\epsilon \to 0$ next.

Consider therefore first the continuum system (5.2.7a)–(5.2.7c) extended with a fast, hydrodynamic time scale $\tau = t/\epsilon$ such that $\partial_t \to \partial_\tau/\epsilon + \partial_t$. Dependencies then become $h = h(\mathbf{x}, t, \tau)$ and so forth. The resulting extended system reads

$$\partial_\tau h + \epsilon\, \partial_t h + \boldsymbol{\nabla} \cdot (h\mathbf{u}) = 0, \tag{5.3.40a}$$

$$\partial_\tau (h\,\mathbf{u}) + \epsilon\, \partial_t (h\mathbf{u}) + \boldsymbol{\nabla} \cdot (h\mathbf{u}\mathbf{u}) + \mathsf{F}^{-2} \boldsymbol{\nabla}(h^2/2) = -\mathsf{F}^{-2} h\, \boldsymbol{\nabla} b - C_f\, \mathbf{u}\, |\mathbf{u}|, \tag{5.3.40b}$$

$$\partial_\tau b/\epsilon + \partial_t b + \boldsymbol{\nabla} \cdot \mathbf{q}_b = 0 \tag{5.3.40c}$$

together with (5.2.7d). This extension, albeit more complicated than the actual system of interest, is more amenable to asymptotic analysis. The variables $h, h\,\mathbf{u}$ and b as functions of $\{\mathbf{x}, t, \tau\}$ are expanded in a perturbation series in ϵ; to wit

$$\begin{aligned} h(\mathbf{x}, t, \tau) &= h^{(0)}(\mathbf{x}, t, \tau) + \epsilon\, h^{(1)}(\mathbf{x}, t, \tau) + \mathcal{O}(\epsilon^2) \\ \mathbf{u}(\mathbf{x}, t, \tau) &= \mathbf{u}^{(0)}(\mathbf{x}, t, \tau) + \epsilon\, \mathbf{u}^{(1)}(\mathbf{x}, t, \tau) + \mathcal{O}(\epsilon^2) \\ b(\mathbf{x}, t, \tau) &= b^{(0)}(\mathbf{x}, t, \tau) + \epsilon\, b^{(1)}(\mathbf{x}, t, \tau) + \mathcal{O}(\epsilon^2) \end{aligned} \tag{5.3.41}$$

with $\mathcal{O}(\epsilon^2)$ denoting terms of order ϵ^2 or higher. Next, we substitute (5.3.41) into (5.3.40) and evaluate the result at the leading order in ϵ.

At leading order, $\mathcal{O}(1/\epsilon)$ in the sediment equation (5.3.40c), we find that $\partial_\tau b^{(0)} = 0$ such that $b^{(0)} = b^{(0)}(\mathbf{x}, t)$ is independent of the fast time scale. At $\mathcal{O}(1)$, we therefore have

$$\partial_\tau h^{(0)} + \boldsymbol{\nabla} \cdot (h^{(0)} \mathbf{u}^{(0)}) = 0, \tag{5.3.42a}$$

$$\begin{aligned} \partial_\tau (h^{(0)}\, \mathbf{u}^{(0)}) + \boldsymbol{\nabla} \cdot (h^{(0)} \mathbf{u}^{(0)} \mathbf{u}^{(0)}) + \mathsf{F}^{-2} \boldsymbol{\nabla} ({h^{(0)}}^2/2) = -\mathsf{F}^{-2} h^{(0)}\, \boldsymbol{\nabla} b^{(0)} \\ -C_f\, \mathbf{u}^{(0)}\, |\mathbf{u}^{(0)}|, \end{aligned} \tag{5.3.42b}$$

$$\partial_\tau b^{(1)} + \partial_t b^{(0)} + \boldsymbol{\nabla} \cdot \left(|\mathbf{u}^{(0)}|^\beta \left(\mathbf{u}^{(0)}/|\mathbf{u}^{(0)}| - \kappa \boldsymbol{\nabla} b^{(0)} \right) \right) = 0 \tag{5.3.42c}$$

in which $h^{(0)}$ and $\mathbf{u}^{(0)}$ depend on $\mathbf{x}, t$ and τ, but $b^{(0)}$ only on $\mathbf{x}$ and t.

To avoid secular growth, the sediment transport equation (5.3.42c) is averaged over the fast time scale to obtain

$$\partial_t b^{(0)} + \boldsymbol{\nabla} \cdot \left(\langle |\mathbf{u}^{(0)}|^{\beta-1} \mathbf{u}^{(0)} \rangle - \langle |\mathbf{u}^{(0)}|^\beta \rangle \kappa \boldsymbol{\nabla} b^{(0)} \right) = 0, \tag{5.3.43}$$

where $\langle \cdot \rangle$ denotes the fast time averaging. Equations (5.3.42a) and (5.3.42b) only depend parametrically on the slow, sediment time scale t for example through $b^{(0)}(\mathbf{x}, t)$ as no slow time derivatives ∂_t appear. If we therefore solve $h^{(0)}$ and $\mathbf{u}^{(0)}$ in (5.3.42a) and (5.3.42b) first, in particular on the fast time scale, we can subsequently use it in the averaged equation (5.3.43). If the long-time fast average is constant on the fast time scale τ, the stationary fast-time solution dominates and we have actually solved the original system for the case $\epsilon = 0$. For (rapidly) oscillating boundary data, no stationary solution may exist reached, in which case the averaging is required.

A leading-order numerical approach, for the stationary hydrodynamic solutions in the limit $\Delta t \to 0$ (e.g., system (5.2.7) with $\epsilon = 0$), is therefore to solve the discrete hydrodynamic continuity and momentum equations on the fast time scale τ till stationarity is reached. The discretization of $b(\mathbf{x}, t)$ is then fixed on the fast time scale, and the discretized sediment equation is subsequently solved separately. We intertwine a fifth-order Runge-Kutta scheme for the fast or pseudo-time τ for the mass and momentum equations, designed to be a dissipative time integration scheme to efficiently reach the steady–state in pseudo–time in [138], and an accurate explicit time discretization for the sediment equation (the third order Runge-Kutta scheme used in [20, 108]). Details are relegated to Appendix B.

Besides the space DGFEM, we also applied and extended the space-time DGFEM, developed in [126] for hyperbolic systems with nonconservative products, to our morphodynamic system. In all verifications with $\kappa = 0$ the space and space-time DGFEM's have been compared, successfully. These and other verifications are reported next.

5.4 Verification

In this section, the accuracy of our numerical scheme, for (5.2.7) with $\epsilon = 0$, is demonstrated by several test cases, also in comparison with exact solutions.

5.4.1 Evolution of an isolated bedform

Consider the evolution of an initially symmetric, isolated bedform subject to steady, unidirectional flow in a domain $x \in [0, 1]$. The setup consists of a channel with a small, but finite amplitude perturbation of the bed level initially centered at x_p, with amplitude A and width $2d$:

$$b(x,0) = \begin{cases} A - A\cos\left(\frac{\pi}{d}(x - x_p + d)\right), & \text{if } |(x - x_p)| \le d, \\ 0.0, & \text{otherwise}, \end{cases} \tag{5.4.1}$$

where $A = 0.05$, $d = 0.1$ and $x_p = 0.5$. At the left boundary we set $h = h(x \downarrow 0, t)$, $hu = 1$, and $b = 0$, and at the right boundary $h = 1$, $hu = hu(x \uparrow 1, t)$, and $b = 0$. As initial condition, the water surface elevation $h(x, 0) + b(x, 0) = 1$ and flow velocity $u(x, 0) = 1$. For this test we adopt $\beta = 3$, $\mathsf{F} = 0.1$, and $C_f = 0.0$. In Figure 5.1, we show the evolution of the solution with $\kappa = 0.0$, computed from time $t = 0.0$ to $t = 0.04$. Figure 5.2 shows the initial condition and the exact and numerical solutions of the isolated bedform computed at time 0.04. Table 5.1 shows that the scheme is second order accurate by computing the L^2 and L^∞ norms of the numerical error in b with respect to the exact solution. In comparison, both space and space-time DGFEM's

N	space DG				space-time DG			
	L_2 error	p	L_∞ error	p	L_2 error	p	L_∞ error	p
40	8.7626e-04		4.2634e-03		1.0006e-03		4.1827e-03	
80	2.1120e-04	2.1	1.1714e-03	1.9	1.5085e-04	2.8	9.5121e-04	2.1
160	4.9064e-05	2.1	2.7252e-04	2.1	3.6876e-05	2.0	1.9613e-04	2.3
320	1.1558e-05	2.1	5.9797e-05	2.2	9.4587e-06	2.0	4.5131e-05	2.1

Table 5.1: The L^2 and L^∞ error norm of bottom level b and convergence rates with order p for the space and space–time DG solutions.

converge and agree with another. Figure 5.3 shows the evolution of the isolated bedform with $\kappa = 0.01$ and $\kappa = 0.1$, respectively.

This exact solution for $\kappa = 0$ is derived as follows and was used in Table 5.1. In the limit $\epsilon \to 0$ and $\kappa \to 0$ on the slow time scale and in one spatial dimension, the system (5.2.7a)–(5.2.7d) satisfies

$$\partial_x(h\,u) = 0 \tag{5.4.2a}$$

$$\partial_x(h\,u^2 + \frac{1}{2}\,\mathsf{F}^{-2}\,h^2) = -\,\mathsf{F}^{-2}\,h\,\partial_x b - C_f\,|u|u \tag{5.4.2b}$$

$$\partial_t b + \partial_x(|u|^{\beta-1}\,u) = 0. \tag{5.4.2c}$$

For $C_f = 0$ and by using upstream values u_0, b_0 and h_0 with discharge $Q = h_0\,u_0$ and Bernoulli constant $B_0 = u_0^2/2 + \mathsf{F}^{-2}\,(h_0 + b_0)$, this system reduces to

$$\frac{1}{2}\,u^3 + (\,\mathsf{F}^{-2} b - B_0)\,u + \mathsf{F}^{-2}\,Q = 0, \qquad h = Q/u, \tag{5.4.3}$$

in which we consider flows with a subcritical root $u = u(b)$ as solution. Substitution of (5.4.3) into the sediment equation in (5.4.2c) then yields a conservation law in the variable b. Further manipulation gives

$$\partial_t b + \beta\,|u(b)|^{\beta-1}\frac{\partial u(b)}{\partial b}\partial_x b = 0, \tag{5.4.4}$$

which has the following implicit solution till the time of wave breaking

$$\begin{aligned} x = x_i + \lambda(b)\,t, \qquad & b = b_i = b_i(x_i) \quad \text{or} \\ b = b_i(x - \lambda(b)\,t) \quad \text{with} \quad & \lambda(b) = \frac{\beta\,|u(b)|^{\beta-1}\,\mathsf{F}^{-2}\,u(b)}{\mathsf{F}^{-2}\,Q/u(b) - u(b)^2}. \end{aligned} \tag{5.4.5}$$

5.4.2 Graded river

In this test, the dynamics induced by a sudden overload of sediment to a base flow solution is considered in a straight channel with unitary width. The exact base state flow solution is given by $\mathbf{u}_0 = (u_0, v_0)^T = (u_0, 0)^T = (1, 0)^T$, $h_0 = 1$, $\mathbf{q}_b = (q_b^0, 0)^T = (1, 0)^T$.

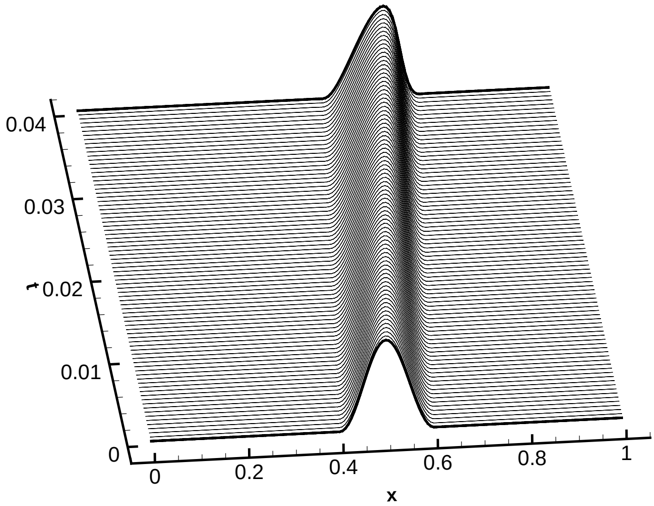

Figure 5.1: Evolution of an isolated bedform from time $t = 0.0$ to 0.04 with $\kappa = 0.0$ using a mesh of 160 elements.

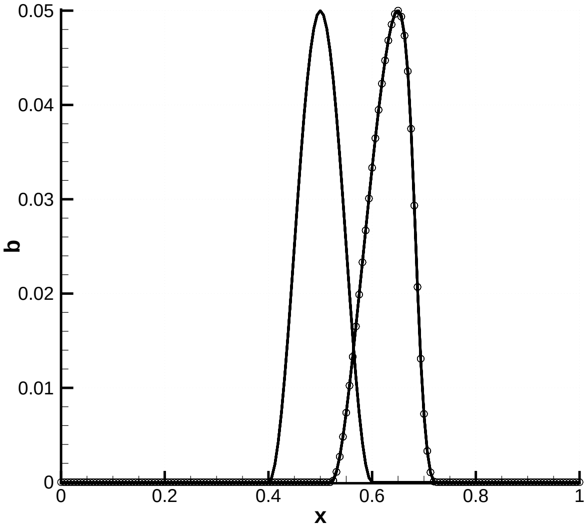

Figure 5.2: Exact (circle) and DGFEM numerical simulation (solid line) with $\kappa = 0.0$.

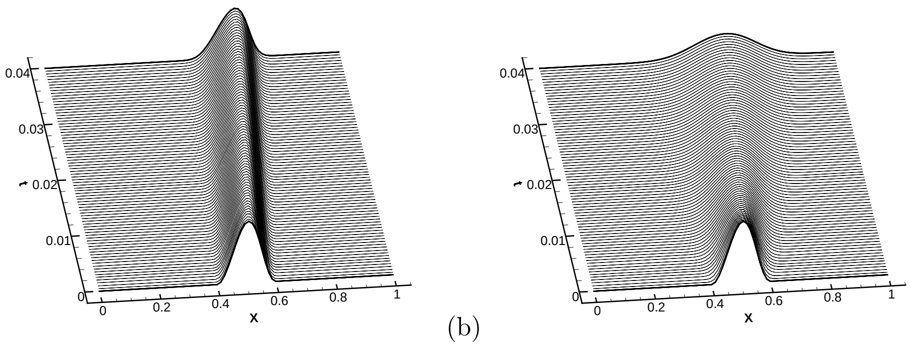

(a) (b)

Figure 5.3: Evolution of an isolated bedform from time $t = 0.0$ to 0.04 for (a) $\kappa = 0.010$ and (b) $\kappa = 0.1$, both using a mesh of 80 elements.

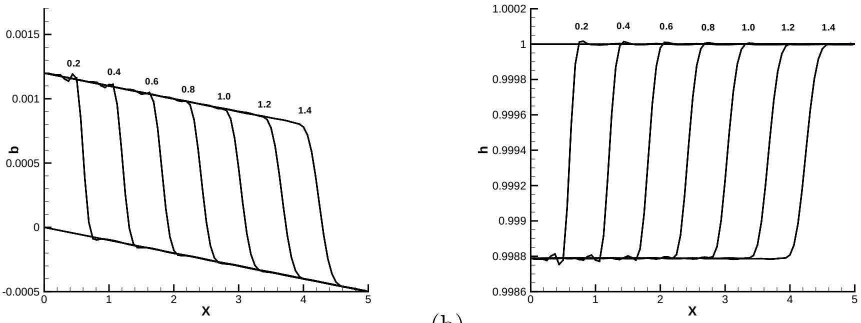

(a) (b)

Figure 5.4: Profiles of (a) bottom level $b(x)$ and (b) water depth $h(x)$ in a straight channel from time $t = 0.0$ to $t = 1.4$ with $\kappa = 0.0$.

Assuming a bed slope $S_0 = 0.0001$, Froude number $\mathsf{F} = 0.1$, and $\kappa = 0.0$, the base state leads to the relation $C_f = S_0 \, \mathsf{F}^{-2} = 0.01$. The *aggradation* of the channel starts when an increase of the bottom topography $b(0,t) = b(0,0) + \delta$ for $t > 0$ is considered at the beginning of the inlet, here with $\delta = 0.0012$. For this test we consider a domain $x \in [0, 5]$ divided into 80 cells. At the left boundary we set $h = h(x \downarrow 0, t)$, $hu = 1$, and $b = 0.0012$ and for the right boundary $h = 1$, $hu = hu(x \uparrow 5, t)$, and $b = -0.0005$. As initial condition, the water depth $h(x, 0) = 1$, the flow velocity $u(x, 0) = 1$, and the bottom elevation has a constant bed slope S_0. Figure 5.4 shows the evolution of the bottom topography and the water depth from time $t = 0.0$ to 1.4. For this test, we compute the solution with space and space–time DG discretizations, obtaining the same, good results. The evolution of the bed level from time $t = 0.0$ to $t = 1.4$ with $\kappa = 0.1$ is shown in Figure 5.5.

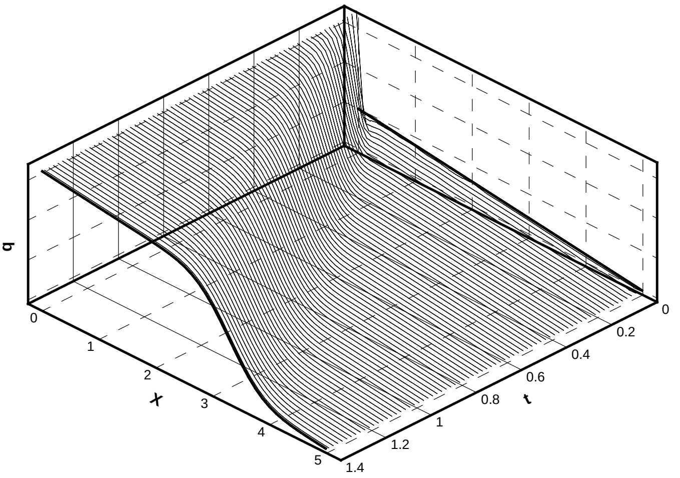

Figure 5.5: Evolution of the bottom level in a straight channel from time $t = 0.0$ to 1.4 with $\kappa = 0.1$.

5.4.3 Travelling wave solution

In this test, a travelling sediment wave is examined in detail to assess the discretization of the downslope gravitational term present in the bed evolution equation. Assuming unidirectional and one-dimensional flow, travelling wave solutions [101] can be found after substituting $b = b(\xi)$ into (5.2.7a)–(5.2.7d) for $\epsilon = 0$ and $\xi = x - ct$ to obtain

$$b' = \left(-cb + u^\beta - \mathcal{Q}\right) / \kappa u^\beta \tag{5.4.6}$$

with $b' = \partial_\xi b$, c the wave speed, $\mathcal{Q}$ the integration constant, and with as flow velocity the subcritical root $u = u(b)$ of the stationary hydrodynamic equations (5.4.3). Equation (5.4.6) is solved using a fourth–order Runge–Kutta discretization for small $\Delta\xi$. For the simulations we use $\beta = 3$, $\kappa = 1$, $c = 1$, $Q = 1$, $\mathsf{F} = 0.1$, and $\mathcal{Q} = 1$. Figure 5.6 shows the travelling wave DGFEM and the "exact" solution of (5.4.6) from time $t = 0$ to 8 in a domain $x \in [0, 5]$. Table 5.2 confirms the good, second-order accuracy of the discretization, including the primal formulation for the diffusive terms.

5.5 Validation

The applicability of our numerical schemes is probed in two test cases: the evolution of a trench in a natural channel, and the hydraulic and sediment transport through a contraction.

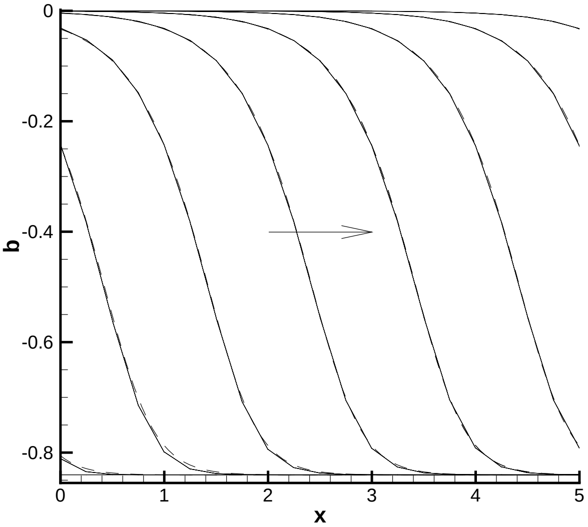

Figure 5.6: DGFEM (solid) and "exact" solution of (5.4.6) (dashed) solutions of the test with a travelling sediment wave moving from left to right from time $t = 0$ to 8 using a mesh of 20 elements.

N	space DG			
	L_2 error	p	L_∞ error	p
10	1.542e-01		1.460e-01	
20	3.840e-02	2.0	4.756e-02	1.6
40	8.278e-03	2.2	1.022e-02	2.2
80	2.151e-03	1.9	1.997e-03	2.3

Table 5.2: The L^2 and L^∞ error norms of b and convergence rates with order p for the space DG solution.

5.5.1 Evolution of a trench in the Paraná river

A sub-fluvial tunnel underneath the Paraná river links the Santa Fe and Paraná cities in Argentina. During the flood of 1983, the tail of a 7m high dune almost uncovered part of the tunnel, nearly leading to its collapse. Subsequently, as part of a study program aimed to further protect the underwater structure, a trench was dug in the main channel during the months of October to December of 1992 to analyze the bedload transport nearby the tunnel axis [127]. To test our DGFEM model, a comparison is made between observations and numerical simulation of the evolution of the trench excavated in the main channel of the Paraná river.

For the numerical model, we used $\beta = 3$ and the Froude number $\mathsf{F} = 0.07950$ was computed based on the characteristic scales $h_0^* = l_0^* = 15.30\text{m}$, and $q_0^* = u_0^* h_0^* = 14.9\text{m}^2\text{s}^{-1}$. These hydrological data were taken from [127]. We chose $t_0^* = 22.5$ days and thus derive $\alpha^* = 1.31 \times 10^{-4}\text{m}^{2-\beta}/\text{s}^{1-\beta}$ and $\epsilon = 8.1 \times 10^{-6}$, cf. §5.2.3. The latter flux ratio lies between the quoted values of 10^{-5} and 10^{-6} in [127].

In a domain $x \in [L_l, L_r]$, with $L_l = -19.6$ and $L_r = 5.18$; upstream boundary conditions are set to $h = h(x \downarrow L_l, t)$, $hu = 1$, and $b = b(L_l, t)$ given by the measured and reconstructed values of the bed topography at the beginning of the trench. Between October 30^{th} and November 11^{th}, the missing data at the left boundary were estimated as shown in Figure 5.7. Downstream boundary conditions are $h = 1$, $hu = hu(x \uparrow L_r, t)$, and $b = b(x \uparrow L_r, t)$. Initial water depth is $h(x, 0) = 1 - b(x, 0)$, and the initial velocity $u(x, 0)$ corresponds with the steady hydrodynamic results determined by the subcritical root $u(x, 0) = u\left(b(x, 0)\right)$, see Equation (5.4.3), with $b(x, 0)$ based on the topography field data measured on October 23^{rd} 1992. The value $\kappa = 0.45$ was chosen to match the measured data better. The simulation was performed for a period of 45 days and we present a comparison between measured and simulated profiles for October 23^{rd} to December 7^{th} 1992 in Figure 5.8. Comparison of simulations with field data show that the main characteristics of the profile, such as the propagation speed of the large, localized step with a planar avalanche face spanning the width of the trench and the dip flowing into the domain, are well captured by our DGFEM simulations. At the end of the trench, extrapolated boundary conditions for $b(x)$ were assigned and a discrepancy between simulations and measurements is found for time $t > 1$ likely due to the coarse reconstruction of the missing field data at the entrance boundary.

5.5.2 Hydraulic and sediment transport through a contraction

Stationary hydraulic and sedimentary flows are considered through a channel with fixed vertical walls and a localized smooth contraction in the middle of the channel. The main reason to consider the bed evolution of hydraulic flow through contraction is to explore the bed evolution in this geometry with an eye to its potential for laboratory experiments. Furthermore, we compare our simulations with the ones of Kubatko *et al.* [46]. Two–dimensional flow and sediment discharge simulations will be presented for two test cases. For the first case, we compare simulations for $\kappa = 0$ with an asymptotic solution based on cross-sectionally averaged equations solely depending on the downstream direction x and time t. The resulting variables are the mean velocity, the mean depth and the mean height of the topography. In the averaging procedure perturbations to these means

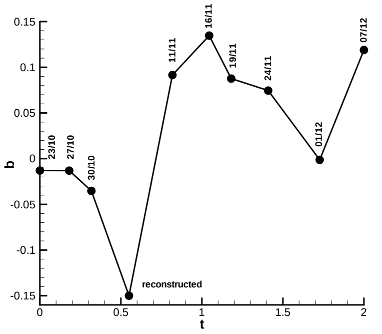

Figure 5.7: Boundary conditions at the left boundary are determined from the data at the boundary and a reconstruction using interior values. To reconstruct the missing boundary data, the velocity of a dip was estimated and the minimum value of the topography was traced back to the left boundary. The missing data point seems so far from the available data due to a propagation of a depression in the bottom level entering the domain. This can be assessed by analyzing the field data, see Figure 5.8.

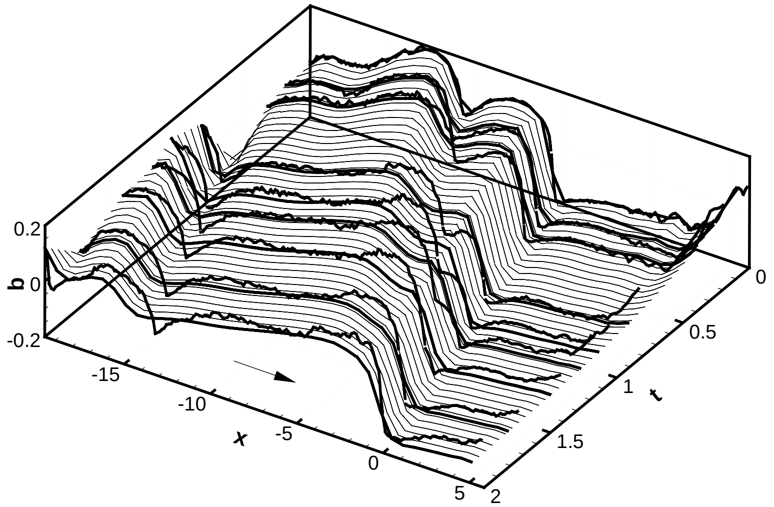

Figure 5.8: Profiles of the numerical evolution of the bottom in a trench from October 23^{rd} to December 7^{th} 1992. Measured profiles (dashed or jagged lines) correspond to October 23^{rd}, October 27^{th}, October 30^{th}, November 11^{st}, November 16^{th}, November 19^{th}, December 1^{st}, and December 7^{th}. The arrow indicates the direction of the flow.

are neglected as these will be small if the constriction is slowly varying in x and the channel sufficiently wide. The variations in flow scales across the channel are then small compared to the downstream scales of interest.

First, consider asymptotic solutions in a channel of varying width $r = r(x)$ with vertical walls. A cross-sectional average of the system (5.2.7) for $\kappa = 0$, while neglecting perturbations of mean quantities, leads to the following one-dimensional system

$$\epsilon\, \partial_t(h\, r) + \partial_x(h\, r\, u) = 0 \tag{5.5.1a}$$

$$\epsilon\, \partial_t(h\, r\, u) + \partial_x(h\, r\, u^2 + \frac{1}{2}\, \mathsf{F}^{-2}\, r\, h^2) = \frac{1}{2}\, \mathsf{F}^{-2}\, h^2\, \partial_x r - \mathsf{F}^{-2}\, hr\, \partial_x b - C_f\, r\, |u| u \tag{5.5.1b}$$

$$\partial_t(b\, r) + \partial_x(r\, |u|^{\beta-1}\, u) = 0. \tag{5.5.1c}$$

Steady-state solutions of (5.5.1) are sought. These satisfy

$$\partial_x(h\, r\, u) = 0 \tag{5.5.2a}$$

$$\partial_x(h\, r\, u^2 + \frac{1}{2}\, \mathsf{F}^{-2}\, r\, h^2) = \frac{1}{2}\, \mathsf{F}^{-2}\, h^2\, \partial_x r - \mathsf{F}^{-2}\, hr\, \partial_x b - C_f\, r\, |u| u \tag{5.5.2b}$$

$$\partial_x(r\, |u|^{\beta-1}\, u) = 0 \tag{5.5.2c}$$

with unknowns $b = b(x), h = h(x), u = u(x)$ for a given channel width $r = r(x)$. After introducing a hydrodynamic discharge $Q = u_0\, h_0\, r_0$; sediment discharge rate $S_e = r_0\, u_0^\beta$; and upstream constant values u_0, h_0, r_0, b_0; the solution of (5.5.2) becomes

$$\begin{aligned} u(x) &= \left(\frac{S_e}{r(x)}\right)^{1/\beta}, \qquad h(x) = \frac{Q}{r(x)\, u(x)}, \\ b(x) &= b_0 + h_0 - h(x) + \mathsf{F}^2\, \frac{1}{2}\, \left(u_0^2 - u(x)^2\right) - \mathsf{F}^2 \int_{x_0}^{x} \frac{C_f\, |u(\tilde{x})|\, u(\tilde{x})}{h(\tilde{x})}\, \mathrm{d}\tilde{x} \end{aligned} \tag{5.5.3}$$

with $x = x_0$ the entrance of the channel. Sample solutions for the case $\kappa = 0$ and $C_f = 0$ and $C_f > 0$ are displayed in Fig. 5.9(a,b). In the latter Fig. 5.9(b), we notice the graded river flow upstream of the contraction, as in § 5.4.2.

Now we consider the corresponding numerical test case. At the inflow boundary we set $h = h(\mathbf{x} \downarrow -5, t)$, $hu = 1$, $hv = 0$ and $b = 0$; and, for the outflow boundary $h = 1$, $hu = hu(\mathbf{x} \uparrow 5, t)$, $hv = hv(\mathbf{x} \uparrow 5, t)$, and $b = 0$. Initial conditions for $h(\mathbf{x})$ and $b(\mathbf{x})$ are given by the asymptotic solution (5.5.3). In Figure 5.10, we compare the asymptotic results against numerical simulation for the case $\kappa = 0$ and $C_f = 0$ assuming a constriction of 1% of the width of the channel. It can be seen that the numerical and asymptotic solutions are highly similar, as expected.

Converging and diverging river channels can typically be found in nature. For the second validation, we examine the morphodynamic evolution of an initially flat bed channel in a converging channel [46]. Now, the constriction is 50% of the total width of the channel. At inflow boundary, the variables are set to $h = h(\mathbf{x} \downarrow -2, t)$, $hu = 1$, $hv = 0$, and $b = 0$; and, at the outflow boundary $h = 1$, $hu = hu(\mathbf{x} \uparrow 2, t)$, $hv = hv(\mathbf{x} \uparrow 2, t)$, and $b = 0$. Initial water depth and discharge correspond with the steady hydrodynamic results obtained with a preliminary simulation in which the bed is considered fixed, with $\mathsf{F} = 0.1$. Figures 5.11, 5.12, 5.13, and 5.14 show the discharge $hu(\mathbf{x})$, $hv(\mathbf{x})$, and bed

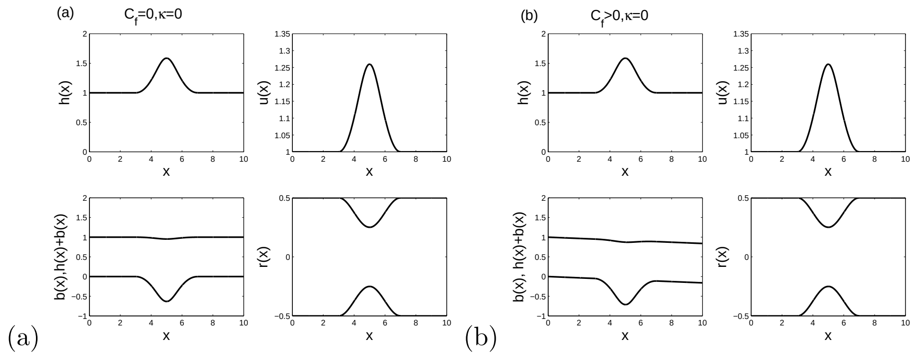

Figure 5.9: Exact steady state solutions of the equations (5.5.2) for the mean velocity $u(x)$, mean depth $h(x)$ and mean bottom $b(x)$, averaged across the channel which has fixed, specified width $r(x)$. These are asymptotic solutions of the two-dimensional equations (5.2.7a)–(5.2.7d) for $\kappa = 0$, $\epsilon = 0$, and (a) $C_f = 0$ and (b) $C_f = 0.1$.

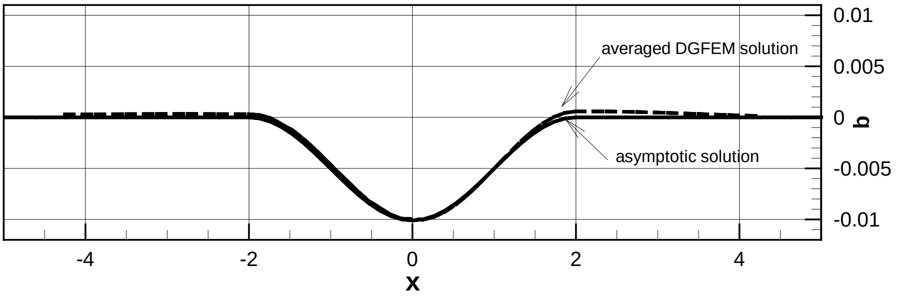

Figure 5.10: Comparison between asymptotic (solid) and numerical simulation (dashed) for the bottom $b(x)$ averaged along channel width for $\epsilon = 0$, $C_f = 0$, and $\kappa = 0$. We used (5.5.3) with $Q = 1$, $\mathsf{F} = 0.1$, and $S_e = 1$.

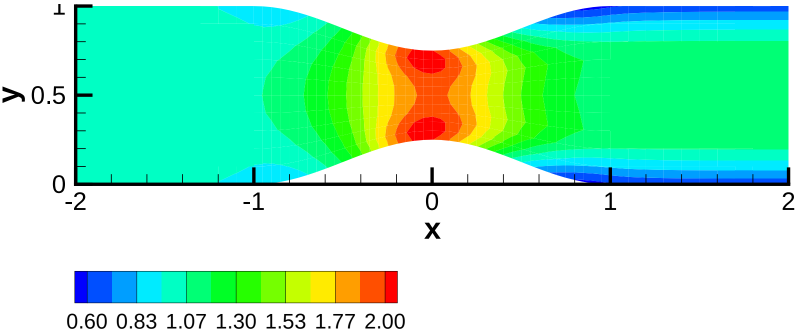

Figure 5.11: Flow and sediment transport in a contraction channel: streamwise unit discharge $hu(\mathbf{x})$.

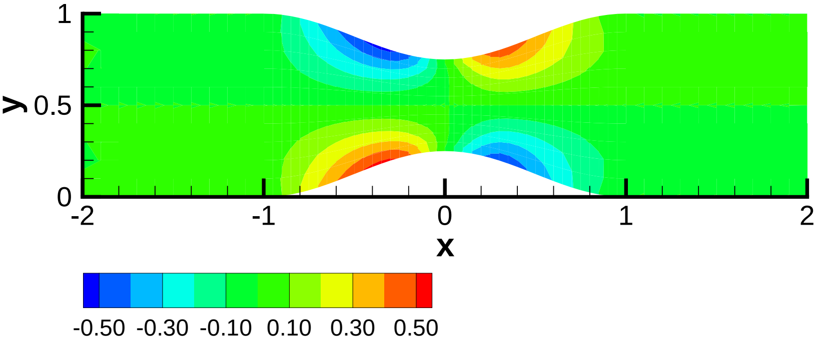

Figure 5.12: Flow and sediment transport in a contraction channel: crosswise unit discharge $hv(\mathbf{x})$.

elevation $b(\mathbf{x})$ at time $t = 0.005$, respectively. As observed in [46], the bed experiences erosion in the converging part of the channel due to an increase in the flow velocity and the development of a mound in the diverging part of the channel, see Figures 5.13 and 5.14; it is a product of a decreasing velocity, see Figures 5.11 and 5.12. In the simulation, the water surface remains rather flat $h(\mathbf{x}) + b(\mathbf{x}) \approx 1$ as expected for low Froude numbers. Our results compare qualitatively well with those presented in [46], and are in good agreement with alternative simulations using the space-time DGFEM, cf. [109]. Laboratory experiments based on the proposed geometry are of further interest to validate these numerical results.

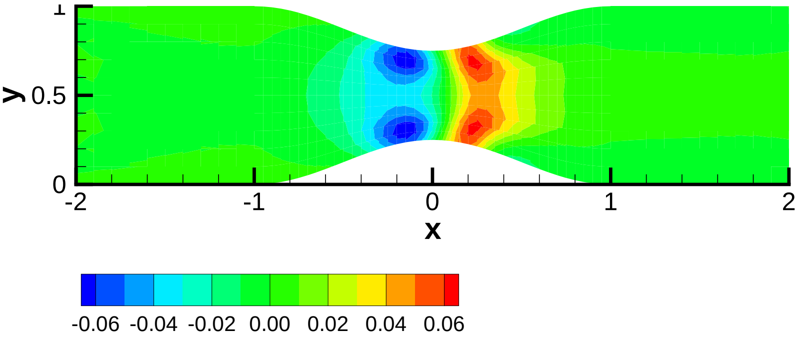

Figure 5.13: Flow and sediment transport in a contraction channel: bottom profile $b(\mathbf{x})$.

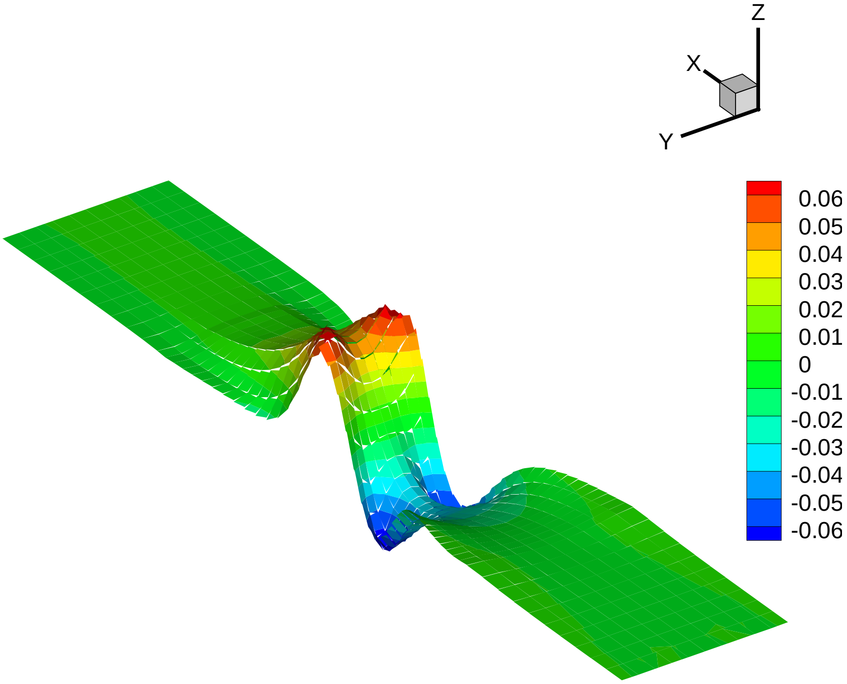

Figure 5.14: Flow and sediment transport in a contraction channel: bottom profile $b(\mathbf{x})$.

5.6 Conclusions

In this chapter, we applied the discontinuous Galerkin finite element discretization of [126] for hyperbolic systems with non-conservative products to a morphodynamic model for shallow flows over varying bottom topography. This is a system of coupled hyperbolic-parabolic equations. The presented extension included an economization of the non-conservative term into conservative and non-conservative parts. Consequently, the computation time greatly reduces. The non-conservative term concerns here only the topographic term in the hydrodynamic momentum equations. The sole diffusive term, in the sediment equation, was treated using a primal formulation. Further extensions including (diffusive) turbulent closure terms in the momentum equations are in progress. In addition, a variety of numerical solutions of shallow water flows over a movable bed have been presented and illustrated in an extensive suite of verification and validation tests. The discontinuous Galerkin scheme used showed very good agreement between model simulations versus (semi–)analytical solutions. Moreover, its ability to capture travelling discontinuities without generating spurious oscillations has been demonstrated. The method also allowed the computation of realistic bed profiles, such as the evolution of a trench dredged in a section of the Paraná river. For this validation test, our model was able to capture timescales of sediment transport over a dredged river section refilled by an advancing sediment wave front. Our DGFEM method also suitably approximated the flow and sediment transport through a contraction in channel width, a situation present in many natural channels. Finally, a laboratory experiment would be timely in validating both the mathematical and numerical modelling for the latter contraction experiment.

Acknowledgments: The author gratefully acknowledges a two-year scholarship of the EU Alβan program. Financial assistance from the Institute of Mechanics, Processes and Control Twente (IMPACT) is also gratefully acknowledged. Silvina Serra is thanked for providing the data set of the trench evolution in the Paraná river. It is a pleasure to thanks Willem Ottevanger for his comments and suggestions.

Appendices

A Algebraic system

A.1 Basis functions and approximations

For each element $K \in \mathcal{T}_h$, polynomial approximations of the trial function U and the test functions V are defined as:

$$U(t, \mathbf{x})|_K := \hat{U}_m(t)\, \psi_m(\mathbf{x}) \quad \text{and} \quad V(\mathbf{x})|_K := \hat{V}_l\, \psi_l(\mathbf{x}), \quad m, l = 0, ..., N_p \tag{A.1}$$

with $\hat{(\cdot)}$ the expansion coefficients, ψ the polynomial basis functions and N_p the appropriate polynomial degree. We have split the approximations of the test and trial functions in the space element K into mean and fluctuating parts. The basis functions are defined as

$$\psi_m(\mathbf{x}, t) = \begin{cases} 1 & \text{if} \quad m = 0 \\ \phi_m(\mathbf{x}) - c_m & \text{otherwise} \end{cases} \tag{A.2}$$

with

$$c_m = \frac{1}{|K_{\mathsf{k}}|} \int_{K_{\mathsf{k}}} \phi_m(\mathbf{x})\, \mathrm{d}\mathbf{x}, \tag{A.3}$$

and basis functions $\phi_m = 1, \zeta_1, \zeta_2, \zeta_1\, \zeta_2$ of polynomial order one in terms of the reference coordinates ζ_1, ζ_2 for quadrilateral elements or only the first three functions for triangular elements, and $|K_{\mathsf{k}}| = \int_{K_{\mathsf{k}}} \mathrm{d}K$ is the area of the element K_{k}.

A.2 Lifting operators

By (5.3.24) and the fact that $\boldsymbol{\nabla} V_h \subset W_h$, the global lifting operator is defined by [18, 28]

$$\sum_{K_{\mathsf{k}}} \int_{K_{\mathsf{k}}} W_k\, \mathcal{R}_k \mathrm{d}K = \sum_{\mathcal{S}_I} \int_{\mathcal{S}} \{\!\{T\, W_k\}\!\}\, [\![U_4]\!]_k\, \mathrm{d}\mathcal{S} + \sum_{\mathcal{S}_B} \int_{\mathcal{S}} W_k^{\mathsf{L}}\, T^{\mathsf{L}}\, (U_4^{\mathsf{L}} - \hat{U}_4^B)\, n_k^{\mathsf{L}}\, \mathrm{d}\mathcal{S}. \tag{A.4}$$

The local lifting operator $\mathcal{R}^{\mathcal{S}}$ can be approximated by polynomial approximations as follows:

$$\mathcal{R}^{\mathcal{S}}(\mathbf{x}) = \hat{R}_j\, \psi_j(\mathbf{x}) \tag{A.5}$$

with $\hat{R}_j$ the expansion coefficients of the approximation. By definition, see (5.3.31), we find that the local lifting operator is only non-zero on the two elements K^{L} and K^{R} directly connected to a face $\mathcal{S} \in \mathcal{S}_I$, hence:

$$\int_{K_{\mathsf{k}}^{\mathsf{L}}} W_k\, \mathcal{R}_k^{\mathcal{S}}\, \mathrm{d}K + \int_{K_{\mathsf{k}}^{\mathsf{R}}} W_k\, \mathcal{R}_k^{\mathcal{S}}\, \mathrm{d}K = \int_{\mathcal{S}} \{\!\{T\, W_k\}\!\}\, [\![U_4]\!]_k\, \mathrm{d}\mathcal{S}. \tag{A.6}$$

Since W is an arbitrary test function, equation (A.6) is equivalent to [18, 28]

$$\int_{K_{\mathsf{k}}^{\mathsf{m}}} W_k\, \mathcal{R}_k^{\mathcal{S}}\, \mathrm{d}K = \frac{1}{2} \int_{\mathcal{S}} W_k^{\mathsf{m}}\, T^{\mathsf{m}}\, [\![U_4]\!]_k\, \mathrm{d}\mathcal{S}, \tag{A.7}$$

where $\mathsf{m} = \mathsf{L}, \mathsf{R}$ is the index of the left and right elements connected to the face $\mathcal{S}$, respectively. Replacing $\mathcal{R}^{\mathcal{S}}$ by its polynomial expansion, we obtain the following expression:

$$\hat{R}^{\mathsf{m}}_{kj} \int_{K^{\mathsf{m}}_{\mathsf{k}}} \psi_l \, \psi_j \, \mathrm{d}K = \frac{1}{2} \int_{\mathcal{S}} \psi^{\mathsf{m}}_l \, T^{\mathsf{m}} \, [\![U_4]\!]_k \, \mathrm{d}\mathcal{S}. \tag{A.8}$$

The coefficients of the polynomial expansion are then computed as:

$$\hat{R}^{\mathsf{m}}_{kj} = \frac{1}{2} \left(M^{-1}_{jl} \right)^{\mathsf{m}} \int_{\mathcal{S}} \psi^{\mathsf{m}}_l \, T^{\mathsf{m}} \, [\![U_4]\!]_k \, \mathrm{d}\mathcal{S}. \tag{A.9}$$

Similarly, at boundary faces the polynomial expansion of the local lifting operator can be computed as:

$$\hat{R}^{\mathsf{L}}_{kj} = \left(M^{-1}_{jl} \right)^{\mathsf{L}} \int_{\mathcal{S}} \psi^{\mathsf{L}}_l \, T^{\mathsf{L}} \left(U^{\mathsf{L}}_4 - U^{B}_4 \right) \, n^{\mathsf{L}}_k \, \mathrm{d}\mathcal{S}. \tag{A.10}$$

The element mass matrices denoted by $M_{jl} = \int_{K_{\mathsf{k}}} \psi_l \psi_j \, \mathrm{d}K$ are readily inverted.

A.3 Discretized algebraic system

After discretizing in space, replacing the trial function U and the test function V by their polynomial approximation and inverting the mass matrix in (5.3.32), we arrive at the following system of ordinary differential equations for the expansion coefficients $\hat{U}$ of the variables U:

$$M \, \frac{\mathrm{d}\hat{U}}{\mathrm{d}t} = \mathcal{L}(\hat{U}), \tag{A.11}$$

with M the mass matrix defined in §A.2 and the operator $\mathcal{L}(\hat{U})$ defined as

$$\mathcal{L}_{il}(\hat{U}) = \sum_{K \in \mathcal{T}_h} \left(-\mathcal{A}_{il} + \mathcal{B}_{il} + \mathcal{E}_{il} - \mathcal{F}_{il} \right) - \sum_{\mathcal{S} \in \mathcal{S}_{I,B}} \left(\mathcal{C}_{il} + \mathcal{D}_{il} - \mathcal{G}_{il} - \mathcal{H}_{il} + \mathcal{I}_{il} \right), \tag{A.12}$$

where the terms $\mathcal{A}$, $\mathcal{B}$, $\mathcal{C}$, $\mathcal{D}$, and $\mathcal{E}$ are defined as:

$$\begin{aligned}
\mathcal{A}_{il} &= \int_K \psi_l \, G_{ikr} \, U_{r,k} \, \mathrm{d}K, \\
\mathcal{B}_{il} &= \int_K \psi_l \, S_i \, \mathrm{d}K, \\
\mathcal{C}_{il} &= \begin{cases} \displaystyle\int_{\mathcal{S}} (\psi^{\mathsf{L}}_l - \psi^{\mathsf{R}}_l) \, (\{\!\{F_{ik}\}\!\} \, n^{\mathsf{L}}_k + \tilde{H}^{nc}_i) \, \mathrm{d}\mathcal{S}, & \text{at } \mathcal{S} \in \mathcal{S}_I \\ \displaystyle\int_{\mathcal{S}} \psi^{\mathsf{L}}_l \, (F^B_{ik} \, n^{\mathsf{L}}_k + \tilde{H}^{nc^B}_i) \, \mathrm{d}\mathcal{S}, & \text{at } \mathcal{S} \in \mathcal{S}_B \end{cases} \\
\mathcal{D}_{il} &= \begin{cases} \displaystyle\int_{\mathcal{S}} \{\!\{\psi_l\}\!\} \left(\int_0^1 G_{ikr} \, (U^{\mathsf{R}}_r - U^{\mathsf{L}}_r) \, \mathrm{d}\tau \, n^{\mathsf{L}}_k \right) \mathrm{d}\mathcal{S}, & \text{at } \mathcal{S} \in \mathcal{S}_I \\ \displaystyle\int_{\mathcal{S}} \psi^{\mathsf{L}}_l \left(\int_0^1 G_{ikr} \, (U^B_r - U^{\mathsf{L}}_r) \, \mathrm{d}\tau n^{\mathsf{L}}_k \right) \mathrm{d}\mathcal{S}, & \text{at } \mathcal{S} \in \mathcal{S}_B, \end{cases} \\
\mathcal{E}_{il} &= \int_K \psi_{l,k} \, F_{ik} \, \mathrm{d}K,
\end{aligned} \tag{A.13}$$

and the terms $\mathcal{F}$, $\mathcal{G}$, $\mathcal{H}$, and $\mathcal{I}$ are defined as:

$$\begin{aligned}
\mathcal{F}_{il} &= \int_K \psi_{l,k}\,\delta_{i4}\,T\,U_{4,k}\,\mathrm{d}K \\
\mathcal{G}_{il} &= \begin{cases} \displaystyle\int_{\mathcal{S}} \delta_{i4}\,\{\!\{T\psi_{l,k}\}\!\}\,(U_4^{\mathsf{L}} - U_4^{\mathsf{R}})\,n_k^{\mathsf{L}}\,\mathrm{d}\mathcal{S}, & \text{at } \mathcal{S}\in\mathcal{S}_I \\ \displaystyle\int_{\mathcal{S}} \delta_{i4}\,\psi_{l,k}^{\mathsf{L}}\,T^{\mathsf{L}}\,\left(U_4^{\mathsf{L}} - U_4^{B}\right)\,n_k^{\mathsf{L}}\,\mathrm{d}\mathcal{S}, & \text{at } \mathcal{S}\in\mathcal{S}_B \end{cases} \\
\mathcal{H}_{il} &= \begin{cases} \displaystyle\int_{\mathcal{S}} \delta_{i4}\,[\![\psi_l]\!]_k\,\{\!\{TU_{4,k}\}\!\}\,\mathrm{d}\mathcal{S}, & \text{at } \mathcal{S}\in\mathcal{S}_I \\ \displaystyle\int_{\mathcal{S}} \delta_{i4}\,\psi_l^{\mathsf{L}}\,T^{\mathsf{L}}\,U_{4,k}^{\mathsf{L}}\,n_k^{\mathsf{L}}\,\mathrm{d}\mathcal{S}, & \text{at } \mathcal{S}\in\mathcal{S}_B \end{cases} \\
\mathcal{I}_{il} &= \begin{cases} \displaystyle\eta\int_{\mathcal{S}} \delta_{i4}\,(\psi_l^{\mathsf{L}} - \psi_l^{\mathsf{R}})\,\{\!\{\mathcal{R}_k^{\mathcal{S}}\}\!\}\,n_k^{\mathsf{L}}\,\mathrm{d}\mathcal{S}, & \text{at } \mathcal{S}\in\mathcal{S}_I \\ \displaystyle\eta\int_{\mathcal{S}} \delta_{i4}\,\psi_l^{\mathsf{L}}\,\mathcal{R}_k^{\mathcal{S}} n_k^{\mathsf{L}}\,\mathrm{d}\mathcal{S}, & \text{at } \mathcal{S}\in\mathcal{S}_B \end{cases} .
\end{aligned} \tag{A.14}$$

B Time stepping scheme

To march in time, in the limit $\epsilon \to 0$, the full system of governing equations (5.2.7a)–(5.2.7c) obtains a special coupling in time as in (5.3.42a)–(5.3.42b) and (5.3.43). Therefore, we distinguish a slow, sediment time scale t and a fast, hydrodynamic time scale τ; then, (A.11) can be split as follows

$$M\,\frac{\mathrm{d}\hat{U}_h}{\mathrm{d}\tau} = \mathcal{L}_1(\hat{U}_h(\tau;t), b(t)) \quad \text{and} \tag{B.1}$$

$$M\,\frac{\mathrm{d}\hat{b}}{\mathrm{d}t} = \mathcal{L}_2(\langle\hat{U}_h\rangle, b), \tag{B.2}$$

where $\hat{U}_h$ concerns the hydrodynamic part. We aim to march (B.1) to steady state in τ and solve (B.2) in t. Consequently, a suitable time discretization is proposed in Algorithm 1. Figure 5.15 shows results obtained with the proposed a first-order time stepping algorithm and the third-order time integration procedure for the graded river test. No appreciable differences between both time integration procedures were found.

```
Input: Given initial conditions $\mathbf{u}(\mathbf{x},0)$, $h(\mathbf{x},0)$ and $b(\mathbf{x},0)$
Output: Compute $\mathbf{u}(\mathbf{x},T_n)$, $h(\mathbf{x},T_n)$ and $b(\mathbf{x},T_n)$
Set $n = 0$;
while $t_n < T_n;\ t_n \in [0;T_n]$ do
    Set $\hat{U}_h^n$;
    Solve $\hat{U}_h^{(k+1)} = \tilde{\alpha}\hat{U}_h^k + \tilde{\beta}\mathcal{L}_1(\hat{U}_h^k, \hat{b}^n)$ till steady state according to $(*)$;
    Hence $\hat{U}_h^n = \langle \hat{U}_h^n \rangle$;
    Solve $\hat{b}^{(1)} = \hat{b}^n + \Delta t\, \mathcal{L}_2(\langle \hat{U}_h \rangle^n, \hat{b}^n)$ according to $(**)$;
    Solve $\hat{U}_h^{(k+1)} = \tilde{\alpha}\hat{U}_h^k + \tilde{\beta}\mathcal{L}_1(\hat{U}_h^k, \hat{b}^{(1)})$ till steady state according to $(*)$;
    Hence $\hat{U}_h^{(1)} = \langle \hat{U}_h^{(1)} \rangle$;
    Solve $\hat{b}^{(2)} = \frac{3}{4}\hat{b}^n + \frac{1}{4}\hat{b}^{(1)} + \frac{1}{4}\Delta t\, \mathcal{L}_2(\langle \hat{U}_h \rangle^{(1)}, \hat{b}^{(1)})$ according to $(**)$;
    Solve $\hat{U}_h^{(k+1)} = \tilde{\alpha}\hat{U}_h^k + \tilde{\beta}\mathcal{L}_1(\hat{U}_h^k, \hat{b}^{(2)})$ till steady state according to $(*)$;
    Hence $\hat{U}_h^{(2)} = \langle \hat{U}_h^{(2)} \rangle$;
    Solve $\hat{b}^{n+1} = \frac{1}{3}\hat{b}^n + \frac{2}{3}\hat{b}^{(2)} + \frac{2}{3}\Delta t\, \mathcal{L}_2(\langle \hat{U}_h \rangle^{(2)}, \hat{b}^{(2)})$ according to $(**)$;
    $t_n \leftarrow t_n + \Delta t$ ; $n \leftarrow n + 1$;
end
```

Algorithm 1: Time stepping algorithm for the morphodynamic model. $(*)$: time stepping algorithm for the flow component (a five-stage explicit Runge-Kutta scheme with appropriate coefficients $\tilde{\alpha}, \tilde{\beta}$, see [138]); $(**)$: stage of a classical three-stage TVD explicit Runge-Kutta scheme [20, 108] for the bed component.

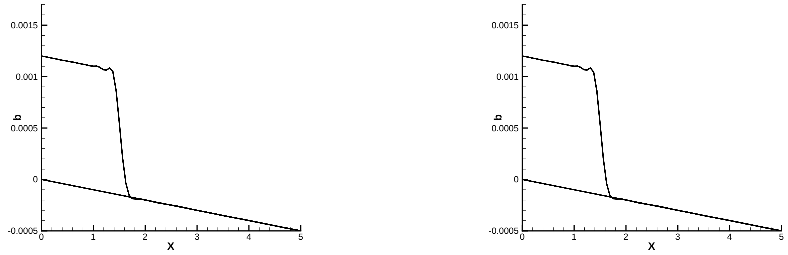

(a) (b)

Figure 5.15: Profiles of bottom level $b(x,t)$ in a straight channel at time $t = 0.5$ for (a) an effectively first-order time stepping scheme and (b) a third-order time stepping scheme.

Chapter 6

Conclusions and recommendations

Throughout this thesis we focused our efforts on two main activities associated with the application of numerical methods to solve particular river hydraulics problems:

(i) The use of numerical simulations for the solution of river engineering problems (Chapters 2 and 3).

(ii) The derivation, design, and implementation of a discontinuous Galerkin method for the solution of the shallow water, sediment transport, and bed evolution equations (Chapters 4 and 5).

In the following, we draw the conclusions of the thesis and give some recommendations for future research.

6.1 Conclusions

In the first part of the thesis, we perform numerical simulations based on the solution of the shallow water equations (SWE) to predict flow resistance and eddy viscosity for vegetated floodplains and compared the values obtained with data of flume experiments and a 1D approximation to the SWE based upon the so–called Lateral Distribution Method (LDM). We established that as more physical mechanisms are included in the mathematical model adopted to describe the flow in compound channel systems, the ratio between the floodplain and the main-channel flow resistance coefficients increases. Nevertheless, whenever water depth and mean velocity distribution data for a given cross-section of a compound system are available, the LDM allows a quick determination of the values of flow resistance and eddy viscosity coefficients for both in-channel and floodplain areas that are highly consistent with a 2D numerical simulation. This finding could mean considerable savings in the burdensome task of specifying flow resistance and turbulence dissipation values for 2D modelling of large compound systems. Additionally, we presented a numerical reconstruction of the catastrophic fooding of Santa Fe City, Argentina

(Figure 6.1 shows the water level of the Salado river before and after the flood). The simulation shows that the flood occurred in two stages: a wave front propagation stage, and a reservoir-filling stage. Consequently, numerical techniques could have been used during the design stage of the flood-protection works to assess the risk associated with the failure of a levee. In Chapters 2 and 3, numerical difficulties associated with wave propagation and advection processes are solved by using the so-called grid enriched velocity solutions and fractional step methods, respectively. Although these techniques have made progress towards solving the fully nonlinear form of the SWE, accuracy, robustness and artificial damping problems remain, especially when coupling flow and transport. These difficulties motivated the development and implementation of numerical schemes based on the discontinuous Galerkin formulation, developed in the second part of this thesis.

In the second part of the thesis, a discontinuous Galerkin finite element discretization has been presented for shallow water flows over varying bathymetry. This discretization had the following novel aspects. First, two accurate numerical fluxes were presented and compared, the HLLC numerical flux and a kinetic flux. While the HLLC flux is a direct approximation to the Riemann problem in a Godunov-type approach at second order in the absence of bathymetry, the kinetic approach directly and more consistently includes the bathymetric terms. The kinetic approach yields a spatial discretization of the relevant Vlasov equation, which is subsequently transformed to the discretized hydrodynamic equations using the transformation between the partial differential equations of the kinetic equation and SWE. The resulting weak formulations differ only with respect to the numerical flux, and both approaches can be extended to higher order. Second, the bathymetry was projected on the quadrilateral elements with the usual second-order finite element basis functions such that the resulting discretized bathymetry was continuous. In addition, the flow variables were also projected using these four basis functions. Consequently, the rest flow state can be preserved exactly in the discretization and to machine precision in the implementation. The verification of numerical and exact solutions showed the methods to be second order in spatial accuracy using equal-order polynomials for the approximation of the flow variables. The shallow water equations globally and locally preserve mass, energy, and mass weighted functions of the potential vorticity (PV) for smooth flows and appropriate boundary conditions. The PV is also a materially conserved quantity consisting of the total vertical vorticity divided by the depth. In the presence of non-uniform bores, a PV anomaly can be generated. By construction, our numerical method only conserves momentum (for constant bottom) and mass exactly. We therefore validated simulations of bore-vortex interactions against a qualitative and asymptotic analysis of the generation of PV anomalies. Consequently, we could correctly predict the signs of the emerging vortices and shear flows. The latter validation is important because numerical schemes may generate vortices of incorrect shape and sign. We considered, in particular, bore-vortex interactions of breaking waves in a channel and the flow of a bore over conical and Gaussian topography. The emerging vortices simulated in the flow over the conical and Gaussian hump compared favorably with simulations performed with a finite volume scheme and with laboratory experiments [56]. Final simulations compared the numerical fluxes for oblique hydraulic jumps in a contraction, also with a laboratory experiment. The kinetic flux turned out to be more robust when shocks are involved. In Chapter 5, we applied and extended the

Figure 6.1: Salado river, Santa Fe, Argentina. Left: Landsat 5 TM satellite image (25-01-00). Right: Spot satellite image (03-05-03). Source: http://www.conae.gov.ar/.

discontinuous Galerkin finite element discretization of [126] for hyperbolic systems with non-conservative products to a morphodynamic model for shallow flows over varying bottom topography. This is a system of coupled hyperbolic-parabolic equations. The presented extension included an economization of the non-conservative term into conservative and non-conservative parts. The latter concerns here only the topographic term in the hydrodynamic momentum equations. Additionally, we do not need any special tricks to deal with discontinuities in the topography. The sole diffusive term, in the sediment equation, was treated using a primal formulation. Furthermore, a variety of numerical solutions of shallow water flows over a movable bed have been presented and illustrated in an extensive suite of verification and validation tests. The discontinuous Galerkin scheme used showed very good agreement between model simulations versus (semi–)analytical solutions. Additionally, its ability to capture travelling discontinuities without generating spurious oscillations has been demonstrated. The method also allowed the computation of realistic bed profiles, such as the evolution of a trench dredged in a section of the Paraná river. For this validation test, our model was able to capture timescales of sediment transport over a dredged river section refilled by an advancing sediment wave front. Finally, our DGFEM method suitably approximated the flow and sediment transport through a contraction in channel width, a situation present in many natural channels.

6.2 Recommendations

The research field of discontinuous Galerkin methods for the solution of physical mechanisms that drives geomorphological changes in alluvial rivers can be expanded to incor-

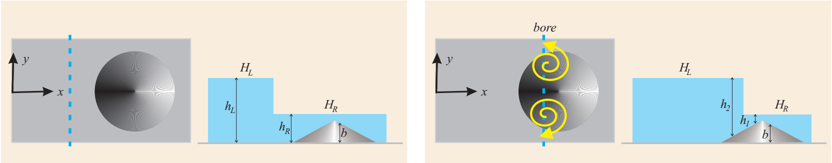

Figure 6.2: Left: At time $t = 0$, a discontinuity in the water surface and fluid initially at rest is given. Right: After the collapse of the dam, a bore is formed and propagates downstream over the conical hump

porate the following additional mechanisms:

(i) A diffusive turbulent closure term in the momentum equations: the implementation of a second-order turbulence closure term in the momentum equations can be done following the discretization techniques presented in Chapter 5 to deal with the presence of the diffusive operator.

(ii) A coupling of an accurate and efficient flooding and drying scheme: improvements in the development of algorithms to capture shoreline movements while conserving mass and momentum have been presented in [135] for space–time DGFEM methods. Their ideas can be extended to our DGFEM method.

(iii) More elaborated friction parametrizations, as presented in Chapter 2, can be easily incorporated in our DGFEM algorithms.

Additionally, refined comparisons between the numerical simulations presented in Chapters 4 and 5, and laboratory data could be achieved by new experiments: (i) a setup consisting of a reservoir with two different water levels separated by a panel, see Figure 6.2, can be constructed to study the generation of vorticity by bores in shallow water layers to validate our PV simulations; and (ii) an erodible channel with vertical walls and a localized contraction to test our sediment transport simulations.

As a final remark, we have developed a mathematical-numerical tool that enables us to reproduce, and eventually, to predict morphological changes produced in alluvial systems, in response to specific flow regimes.

Bibliography

[1] Carrasco A. and Vionnet C.A., *Separation of scales on a broad, shallow turbulent flow*, J. Hydraulic Research **42** (2004), no. 6, 630–638.

[2] Harten A., Lax P.D., and van Leer B., *On upstream differencing and Godunov-type schemes for hyperbolic conservation laws*, SIAM Rev. (1983), no. 25, 35–61.

[3] Kassem A. and Chaudhry M.H., *Comparison of coupled and semicoupled numerical models for alluvial channels*, Journal of Hydraulic Engineering **124** (1998), no. 8, 794–802.

[4] Brooks A.N. and Hughes T.J.R., *Streamline Upwind/Petrov-Galerkin formulations for convective dominated flows with particular emphasis on the incompressible Navier-Stokes equations*, Computer Methods in Applied Mechanics and Engineering **32** (1982), 199–259.

[5] Vreman A.W., Al-Tarazi M., Kuipers J.A.M., Van Sint Annaland M., and Bokhove O., *Supercritical shallow granular flow through a contraction: experiment, theory and simulation.*, Journal of Fluid Mechanics **578** (2007), 233–269.

[6] Akers B., *Shallow water flow through a contraction.*, Tech. report, Woods Hole Oceanographic Institution, Woods Hole, MA 02543 USA, 2005, http://gfd.whoi.edu/proceedings/2005/PDFvol2005.html.

[7] Cockburn B., *Discontinuous Galerkin methods for convection-dominated problems*, High-Order Methods for Computational Physics (Barth T. and Deconinck H., eds.), vol. 9, Springer Verlag, 1999, pp. 69–224.

[8] Cockburn B. and Shu C.-W., *The Runge-Kutta discontinuous Galerkin finite element method for conservation laws V: Multidimensional systems*, J. Comput. Phys. **141** (1997), 199–224.

[9] ———, *The local discontinuous Galerkin method for time-dependent convection-diffusion systems*, SIAM J. Numer. Anal. **35** (1998), no. 6, 2440–2463 (electronic). MR MR1655854 (99j:65163)

[10] ______, *Runge-Kutta discontinuous Galerkin methods for convection-dominated problems*, SIAM J. Sci. Comput. **16** (2001), 173–261.

[11] Cockburn B., Karniadakis G.E., and Shu C.-W., *The development of discontinuous Galerkin methods*, Discontinuous Galerkin methods; Theory, Computation and Applications. (C.-W. Shu B. Cockburn, G.E. Karniadakis, ed.), Lecture Notes in Computational Science and Engineering, vol. 11, Springer, New York, Heidelberg, 2000.

[12] Gardiner B., *Extreme weather on the rise*, Tech. report, Associated Press, London, February 2003.

[13] Hunt B., *Water waves generated by distant landslides*, J. Hydraulic Research (1988), no. 26, 307–322.

[14] Perthame B., *An introduction to kinetic schemes for gas dynamics*, An introduction to recent developments in theory and numerics for conservation laws (Rohde C. Kröner D., Ohlberger M., ed.), Springer Verlag, 1999, pp. 1–27.

[15] Perthame B. and Simeoni C., *A kinetic scheme for the Saint-Venant scheme with a source term*, Calcolo **38** (2001), 201–231.

[16] Brigham Young University, Environmental Modeling Research Laboratory, USA, *SMS Surfacewater Modelling System User's Manual*, 1999.

[17] Johnson C., *Numerical solution of partial differential equations by the finite element method*, 1990.

[18] Klaij C., *Space–time discontinuous Galerkin method for compressible flow*, Ph.D. thesis, University of Twente, 2006.

[19] Vionnet C. and García M., *Catastrophic flooding in Santa Fe, Argentina*, Tech. Report 4, IAHR Newsletter, 2003.

[20] Shu C.-W., *TVD time discretizations*, SIAM J. Sci. Stat. Comput. **9** (1988), 1073–1084.

[21] Vionnet C.A., Tassi P.A., and Martín Vide J.P., *Estimates of flow resistance and eddy viscosity coefficients for 2D modelling on vegetated floodplains*, Hydrological Processes **18** (2004), no. 15, 2907–2926.

[22] Vionnet C.A., Tassi P.A., Rodriguez L.B., and Ferreira C.G., *Numerical modelling of the catastrophic flooding of Santa Fe city, Argentina*, Int. Journal of River Basin Management **4** (2006), no. 4.

[23] Wilson C.A.M.E., Bates P.D., and Hervouet J.-M., *Comparison of turbulence models for stage-discharge rating curve prediction in reach-scale compound channel flows using two-dimensional finite element methods*, Journal of Hydrology (2002), no. 257, 42–58.

[24] Wilson C.A.M.E., Stoesser T., Bates P.D., and Batemann Pinzen A., *Open channel flow through different forms of submerged flexible vegetation*, ASCE Journal of Hydraulic Engineering (2003), no. 129, 847–853.

[25] Vreugdenhil C.B., *Numerical methods for shallow water flow*, 2nd ed., Kluwer Academic Publishers: Dordrecht, Netherlands, 1994.

[26] CEPAL, *Impact evaluation of the Salado river flood in the Santa Fe state, Argentina (in spanish)*, Tech. report, United Nations - Economic Council for Latin American and the Caribbean (CEPAL), Rep. LC/BUE/R.246.

[27] Ferreira C.G., *Hydrology of the Salado river lower basin during January-May 2003 (in Spanish)*, Tech. report, Ministry of Public Works (MOSPyV), Santa Fe State, Argentina, Annexo I Report Dept. Water Res.(Memo. 40/2003).

[28] Klaij C.M., van der Vegt J.J.W., and van der Ven H., *Space-time discontinuous Galerkin method for the compresible Navier-Stokes equations*, J. Comput. Phys. **217** (2006), 589–611.

[29] ASCE Task Committee, *Final report on the ASCE Task Committee on hydraulics, bank mechanics and river width adjusment.I: Processes and mechanisms*, J.Hydr.Engrg. **124** (1998), no. 124, 881–902.

[30] Houghton D. D. and Kasahara A., *Nonlinear Shallow Fluid Flow Over an Isolated Ridge*, Communications on Pure and Applied Mathematics **21** (1968), 1–23.

[31] Schwanenberg D. and Köngeter J., *A discontinuous Galerkin method for the shallow water equations with source terms*, Discontinuous Galerkin methods (B. Cockburn, G. E. Karniadakis, and C.-W. Shu, eds.), LNCSE, Springer, Berlin, 2000, pp. 419–424.

[32] Schwanenberg D. and Harms M., *Discontinuous Galerkin finite-element method for transcritical two-dimensional shallow water flows*, J. Hydr. Engrg. **130** (2003), no. 5, 412–421.

[33] Ervine D.A., Babaeyan-Koopaei K., and Sellin R.H.J., *Two-dimensional solution for straight and meandering overbank flows*, ASCE Journal of Hydraulic Engineering (2000), no. 126, 653–669.

[34] de Vriend H.J., *2DH mathematical modelling of morphological evolutions in shallow water*, Coastal Engineering (1987), no. 11, 1–27.

[35] Peregrine D.H., *Surf zone currents*, Theor. Comput. Fluid Dyn. **10** (1998), 295–310.

[36] ———, *Large-scale vorticity generation in breakers in shallow and deep water.*, J. Mech. B/Fluids (1999), no. 18, 403–408.

[37] Krohling D.M and Iriondo M., *Upper quaternary palaeoclimates of the Mar Chiquita area, North Pampa, Argentina*, Quaternary Int. (1999), no. 57/58, 149–163.

[38] Arnold D.N., Brezzi F., Cockburn B., and Marini D.L., *Unified analysis of discontinuous Galerkin methods for elliptic problems*, SIAM Journal on Numerical Analysis **39** (2002), no. 5, 1749–1779.

[39] Kelly D.W., Nakazawa S., Zienkiewicz O.C., and Heinrich J.C., *A note on upwinding and anisotropic balancing dissipation in finite element approximations to convective diffusion problems.*, International Journal of Numerical Methods in Engineering (1980), no. 15, 1705–1711.

[40] Knight D.W. and April J.B., *Refined calibration of a depth-averaged model for turbulent flow in a compound channel*, Proceedings of the Institution of Civil Engineers Water, Maritime & Energy, no. 118, pp. 151–159.

[41] Knight D.W. and Shiono K., *Turbulence measurements in a shear layer region of a compound channel*, Journal of Hydraulic Research (1990).

[42] Audusse E., Bouchut F., Bristeau M.O., Klein R., and Perthame B., *A fast and stable well-balanced scheme with hydrostatic reconstruction for shallow water flows*, SIAM J. of Sc. Comp. **25** (2004), no. 6, 2050–2065.

[43] Marchi E., *On the free overfall*, Journal of Hydraulic Research (1993), no. 31, 777–790.

[44] Toro E.F., *Shock-capturing methods for free-surface shallow flows*, Wiley & Sons: Chichester, UK, 2001.

[45] Kubatko E.J., Westerink J.J, and Dawnson C., *hp Discontinuous Galerkin methods for advection dominated problems in shallow water flows*, Comput. Methods Appl. Mech. Engrg. **196** (2006), 437–451.

[46] Kubatko E.J., Westerink J.J., and Dawson C., *An unstructured grid morphodynamic model with a discontinuous Galerkin method for bed evolution*, Ocean Modelling (2006), no. 15, 71–89.

[47] Electricité de France, Départment Laboratorie National d'Hydraulic, *Telemac Modelling System – Hydrodynamics TELEMAC-2D Software v.4.0. User's Manual*, 1998.

[48] Engelund F., *Flow and bed topography in channel bends*, Journal of the Hydraulics Division, no. 100, 1631–1648.

[49] Engelund F. and Skovgaard O., *On the origin of meandering and braiding in alluvial streams*, J. Fluid Mech. **57** (1973), 289–302.

[50] L. Fraccarollo and H. Capart, *Riemann wave description of erosional dam-break flows*, J. Fluid Mech. **461** (2002), 183–228.

[51] Hu G., *Note on numerical simulation of shallow water.*, Tech. Report AM-02-01, Bristol University, School. of Mathematics., 2002, 17 pp.

[52] Parker G., *1D sediment transport morphodynamics with applications to rivers and turbidity currents*, e-book downloadable from http://cee.uiuc.edu/people/parkerg/.

[53] Seminara G., *Stability and morphodynamics*, Meccanica (1998), no. 33, 59–99.

[54] Whitham G.B., *Linear and nonlinear waves*, John Wiley, London., 1974.

[55] Kiely G.K. and McKeogh E.J., *Experimental comparison of velocity and turbulence in compound channels of varying sinuosity.*, Channel Flow Resistance: Centennial of Manning's Formula, Water Resources Publications: Littleton, Colorado, USA, pp. 393–408.

[56] Matsutomi H. and Mochizula A., *Behaviour of a bore over a conical shoal.*, Tohoku Journal of Natural Disaster Science (2001), In Japanese.

[57] Fischer H.B., List J.E., Koh R.C.Y., Imberger J., and Brooks N.H., *Mixing in Inland and Coastal Waters*, Academic Press, San Diego, 1979.

[58] Nezu I. and Nakagawa H., *Turbulence in open-channel flows*, IAHR Monograph: Balkema, Rotterdam, Netherlands, 1993.

[59] INA, *Hydraulic redesign of the Santa Fe – Rosario freeway bridge (in Spanish)*, Tech. report, National Institute for the Water and the Environment - INA, local division CRL, Santa Fe, Argentina.

[60] INCOCIV, *Hydraulic study for flood-control structures of Santa Fe city (in Spanish), Final Report*, Tech. report, Consulting Co. on Civil Engineering - INCOCIV, State of Entre Ríos, Argentina., 2003.

[61] Jaffre J., Johnson C., and Szepessy A., *Convergence of the discontinuous Galerkin finite element method for hyperbolic conservation laws*, Mathematical Models and Methods in Applied Sciences **5** (1995), no. 3, 367–386.

[62] Lamb J., *Hydrodynamics*, Cambridge University Press., 1993.

[63] Lewin J., Macklin M.G., and Newson M.D., *Regime theory and environmental change - irreconcilable concepts?*, International Conference on River Regime (Wiley, Chichester) (White W.R., ed.), 1988, pp. 431–445.

[64] Pedlosky J., *Geophysical fluid dynamics*, 2nd ed., Springer, 1987.

[65] Shi J., Thomas T.G., and Williams J.J.R., *Free-surface effects in open channel flow at moderate Froude and Reynold's numbers*, Journal of Hydraulic Research (2000), no. 38, 465–474.

[66] Hervouet J.-M., *A high resolution 2-d dam-break model using parallelization.*, Hydrological Processes (2000), no. 14, 2211–2230.

[67] ———, *On spurious oscillation in primitive shallow water equations.*, Proceedings of the XIII Int. Conf. on Computational Methods in Water Resources, vol. II, Balkema Publishers, Rotterdam, 2000, pp. 929–936.

[68] Hervouet J.-M. and Van Haren L., *Recent Advances in Numerical Methods for Fluid Flows*, Floodplain Processes (Bates PD Anderson MG, Walling DE, ed.), John Wiley and Sons: Chichester, pp. 183–214.

[69] Cunge J.A., Holly F.M., and Verwey A., *Practical aspects of computational river hydraulics*, London: Pitman, 1981.

[70] Wark J.B., Samuels P.G., and Ervine D.A., *A practical method of estimating velocity and discharge in a compound channel*, River Flood Hydraulics (White WR, ed.), Wiley: Chichester, 1990, pp. 163–172.

[71] Acuña J.C., *Emergency program for the recuperation of flood affected zones (in spanish)*, Tech. report, Ministry of Public Works (MOSPyV), Santa Fe State, September 2003.

[72] Galland J.C., Goutal N., and Hervouet J.M-., *TELEMAC: a new numerical model for solving shallow water equations*, Adv. Water Resour. **14** (1991), 138–148.

[73] Flaherty J.E., R.M. Loy, M.S. Shepard, and J.D. Teresco, *Software for the parallel adaptive solution of conservation laws by Discontinuous Galerkin Methods*, Discontinuous Galerkin Methods; Theory, Computation and Applications. (C.-W. Shu B. Cockburn, G.E. Karniadakis, ed.), Lecture Notes in Computational Science and Engineering, vol. 11, Springer, New York, Heidelberg, 2000.

[74] Stoker J.J., *Water waves. The mathematical theory with applications*, 1958.

[75] Lee J.K., Froehlich D.C., and Gilbert J.J. Wiche G.J., *A two–dimensional finite element model study of backwater and flow distribution at the I–10 crossing of the Pearl River near S lidell, Lousiana*, Tech. report, USGS, 1983, Water Res. Inv. Report 82-4119, 66 p.

[76] López J.L., García-Martínez R., and Pérez-Hernández D., *The torrential landslides of December 1999 in Venezuela (in Spanish)*, Proceedings XIX Latin-American Hydraulic Conf. (Córdoba, Argentina), 2000, pp. 417–426.

[77] Hervouet J.M. and Petitjean A., *Malpasset dam-break revisited with two-dimensional computation*, J. Hydraulic Research (1999), no. 37, 777–788.

[78] Hervouet J.M., Samie R., and Moreau B., *Modelling urban areas in dam-break flood-wave numerical simulations.*

[79] Martín Vide J.P., *Restoration of an urban river in Barcelona, Spain.*, Environmental Engineering Policy (2001), no. 2, 113–119.

[80] Shiono K. and Knight D.W., *Turbulent open-channel flows with variable depth across the channel*, Journal of Fluid Mechanics (1991), no. 222, 617–646.

[81] Shiono K. and Muto Y., *Complex flow mechanisms in compound meandering channels with overbank flows*, Journal of Fluid Mechanics (1998), no. 376, 221–261.

[82] Han K-Y., Lee J-T, and Park J-H., *Flood inundation analysis resulting from levee-break*, J. Hydraulic Research (1998), no. 36, 747–759.

[83] Erduran K.S. and Kutija V., *Quasi-three-dimensional numerical model for flow through flexible, rigid, submerged and non-submerged vegetation*, Journal of Hydroinformatics (2003), no. 05.3, 189–202.

[84] Krivodonova L., Xin J., Remacle J.-F., and Chevaugeon N., *Shock detection and limiting with discontinuous Galerkin methods for hyperbolic conservation laws*, Applied Num. Math. **48** (2004), 323–338.

[85] Leopold L.B. and Wolman M.G., *River channel patterns – braided, meandering, and straight*, US Geological Survey Professional Paper 282-B (1957).

[86] Van Rijn L.C., *Sediment transport III: Bed forms and alluvial roughness*, ASCE Journal of Hydraulic Engineering (1984), no. 110, 1733–1754.

[87] Pratt L.J., *On inertial flow over topography. Part 1. Semigeostrophic adjustment to an obstacle*, J. Fluid Mech. **131** (1983), 195–218.

[88] Castro M., Gallardo J.M., and Pares C., *High order finite volume schemes based on reconstruction of states for solving hyperbolic systems with nonconservative products. applications to shallow-water systems.*, Math. Comp., to appear.

[89] Church M., *Bed material transport and the morphology of alluvial river channels*, Annu. Rev. Earth Planet. Sci. **34** (2006), 325–354.

[90] Gaddi M., Sexton T., Muste M., Patel V.C., and Alvarez P.J.J., *International perspectives in water resources management: the Paraná river watershed*, World Transactions on Engineering and Technology Education, no. 2, pp. 435–439.

[91] Castignani M.I., Cursack A.M., D'Angelo C., Tosolini R., and Travadero M., *Soil and productivity aspects; evolution in land used (in Spanish)*, Tech. report, UNL Sec. Extensión, 2003.

[92] Ghidahoui M.S. and Kolyshkin A.A., *Linear stability analysis of lateral motions in compound open channels*, ASCE Journal of Hydraulic Engineering (1999), no. 125, 871–880.

[93] Horrit M.S. and Bates P.D., *Predicting floodplain inundation: raster-based modelling versus the finite-element approach*, Hydrological Processes (2001), no. 15, 825–842.

[94] Arnel N., *Global warming, river flows and water resources*, Wiley, Chichester, 1996.

[95] Garcia N. and Vargas W., *The temporal climatic variability in the Río de la Plata basin displayed by the river discharges*, Climatic Change (1998), no. 38, 359–379.

[96] Kouwen N., *Modern approach to design of grassed-channels*, Journal of Irrigation and Drainage Engineering (1992), no. 118, 733–743.

[97] Kouwen N. and Li R.M., *Biomechanics of vegetative channel linings*, Journal of the Hydraulics Division, no. 106, 1085–1103.

[98] Katopodes N.D., *A dissipative Galerkin scheme for open-channel flows*, J. Hydraul. Eng. ASCE **110** (1984), 450–466.

[99] Bokhove O., *Flooding and drying in finite-element Galerkin discretizations of shallow-water equations. Part I: One dimension.*, J. Sci. Comput. **22** (2005), 47–82.

[100] ______, *Hamiltonian restriction of Vlasov equations into two-layer isopycnic and isentropic equations.*, Appl. Math. Lett. (2005), no. 18, 47–82.

[101] Bokhove O., Woods A.W., and Boer de A., *Magma Flow through Elastic-Walled Dikes*, Theor. Comput. Fluid Dyn. **19** (2005), 261–286.

[102] Bühler O., *On the vorticity transport due to dissipating or breaking waves in shallow-water flow*, J. Fluid Mech. **407** (2000), 235–263.

[103] Zienkiewics O.C. and Ortiz P., *A split-characteristic based finite element model for the shallow water equations*, Int. J. Numer. Methods Fluids **20** (1995), no. 2, 1061–1080.

[104] Ackers P., *Hydraulic design of two-stage channels*, Proceedings of the Institution of Civil Engineers Water, Maritime & Energy, vol. 96, 1992, pp. 247–257.

[105] Batten P., Clarke N., Lambert C., and Causon D.M., *On the Choice of Wavespeeds for the HLLC Riemann Solver*, SIAM J. Sci. Comput. **18** (1997), no. 6, 1552–1570.

[106] Hall P., *Alternating bar instabilities in unsteady channel flows over erodible beds*, J. Fluid Mech. (2004), no. 499, 49–73.

[107] Tassi P., Vionnet C., and Rodríguez L., *Integrating technologies for 2d numerical modelling of the Paraná river*, Proceedings of Hydroinformatics 2000 Conference (Iowa City, Iowa, USA), 23-37 July 2000.

[108] Tassi P., Bokhove O., and Vionnet C., *Space discontinuous Galerkin method for shallow water flows —kinetic and HLLC flux, and potential vorticity generation*, Advances in Water Resources **30** (2007), no. 4.

[109] Tassi P., Rhebergen S., Vionnet C., and Bokhove O., *A discontinuous Galerkin finite element model for morphological evolution under shallow flows: Additional appendices*, (2007), http://eprints.eemcs.utwente.nl/9962/.

[110] Tassi P.A., Rhebergen S., Vionnet C.A., and Bokhove O., *A discontinuous Galerkin finite element model for morphological evolution under shallow flows*, Computer Methods in Applied Mech. and Eng. (2007), Submitted.

[111] Bates P.D., Steward M.D., Siggers G.B., Smith C.N., Hervouet J.-M., and Sellin R.H.J., *Internal and external validation of a two dimensional finite element model for river flood simulation*, Proceedings of the Institution of Civil Engineers Water, Maritime & Energy.

[112] Bates P.D. and Anderson M.G., *A two-dimensional finite-element model for river flow inundation.*, Proceedings of the Royal Society of London Series A, vol. 440, 1993, pp. 481–491.

[113] Bates P.D., Horritt M.S., Smith C.N., and Mason D., *Integrating remote sensing observations of flood hydrology and hydraulic modelling*, Hydrological Processes (1997), no. 11, 1777–1795.

[114] Atkinson P.H., Westerink J.J., and Hervouet J.-M., *Similarities between the quasi–bubble and the generalized wave continuity equation solutions to the shallow water equations*, Int. J. Num. Meth. in Fluids (2004), no. 45, 689–714.

[115] Morrison P.J., *The Maxwell-Vlasov equations as a continuous hamiltonian system*, Phys. Lett. **80** (1980), 383–386.

[116] Lloyd P.M. and Stansby P.K., *Shallow-water flow around model conical islands of small side slope. I: Surface piercing*, ASCE Journal of Hydraulic Engineering (1997), no. 123, 1057–1067.

[117] Wormleaton P.R., *Floodplain secondary circulation as a mechanism for flow and shear stress redistribution in straight compound channel*, Coherent Flow Structures in Open Channels (Ashworth P.J., Bennett S.J., Best J.L., and M^c Lelland S.T., eds.), John Wiley and Sons: Chichester, 1996, pp. 581–608.

[118] Guo Q.-C. and Jin Y.-C., *Modeling nonuniform suspended sediment transport in alluvial rivers*, J. Hydraul. Eng. **128** (2002), no. 9, 839–847.

[119] LeVeque R., *Numerical methods for conservation laws*, Lectures in mathematics ETH Zurich, pub-Birkhauser, 1990.

[120] Walters R.A. and Carey G.F., *Analysis of spurious oscillations modes for the shallow-water and Navier–Stokes equations*, Computers and Fluids **11** (1983), no. 2, 51–68.

[121] Myers R.C. and Lyness J.F., *Discharge ratios in smooth and rough compound channels*, Journal of Hydraulic Engineering (1997).

[122] Research System Inc., Illinois, USA, *The environment for visualizing images, v.4.0, exploring ENVI, training course manual.*

[123] Sellin R.H.J., Bryant T.B., and Loveless J.H., *An improved method for roughening floodplains on physical river models*, Journal of Hydraulic Research (2003), no. 41, 3–14.

[124] Chippada S., Dawson C.N., Martinez M.L., and Wheeler M.F., *A Godunov-type finite volume method for the system of shallow water equations.*, Comp. Meth. Appl. Mech. and Eng. **151** (1998), 105–129.

[125] Haider S., Paquier A., Morel R., and J-Y. Champagne, *Urban flood modelling using computational fluid dynamics*, Proc. Institution of Civil Engineering, Water & Maritime Engs (2002), 1–8.

[126] Rhebergen S., Bokhove O., and van der Vegt J.J.W., *Discontinuous Galerkin finite element methods for hyperbolic nonconservative partial differential equations*, J. Comp. Phys. (2007), submitted, http://eprints.eemcs.utwente.nl/8629/.

[127] Serra S., *Flow and bed-load transport over an erodible bed covered with dunes*, Master's thesis, Universidad Nacional del Litoral, FICH, 2007.

[128] Chapra S.C., *Surface water quality modeling*, McGraw Hill, 1997.

[129] Darby S.E., *Effect of riparian vegetation on flow resistance and flood potential*, ASCE Journal of Hydraulic Engineering (1999), no. 125, 443–454.

[130] Telemac Modelling System, *2D Hydrodynamics TELEMAC-2D software, v.4.0, User's Manual*, EDF. Electricité de France, Département Laboratoire National d'Hydraulique, 1998.

[131] Fischer-Antze T., Stoesser T., Bates P., and Olsen N.R.B., *3D numerical modelling of open-channel flow with submerged vegetation*, Journal of Hydraulic Research (2001), no. 39, 303–310.

[132] Stoesser T., Wilson C.A.M.E., Bates P.D., and Dittrich A., *Application of a 3D numerical model to a river with vegetated floodplains*, Journal of Hydroinformatics (2003), no. 05.2, 99–112.

[133] Wahl T., *Predicting embankment dam break parameters - a needs assessment*, Proc. XXVII IAHR Conf. (San Francisco, CA, USA), Aug. 10-15 1997.

[134] E. F. Toro, *Riemann solvers and numerical methods for fluid dynamics : a practical introduction*, Springer, 1997.

[135] Ambati V., *Flooding and drying in discontinuous Galerkin discretizations of shallow water equations*, European Conference on Computational Fluid Dynamics ECCOMAS CFD 2006 (TU Delft, The Netherlands) (Wesseling P., Oñate E., and Pèriaux J., eds.).

[136] Casulli V., *Semi-implicit finite difference methods for two-dimensional shallow water equations*, J. Comput. Physics (1990), no. 86, 56–74.

[137] Kutija V. and Hong H.T.M., *A numerical model for assessing the additional resistance to flow introduced by flexible vegetation*, Journal of Hydraulic Research (1996).

[138] van der Vegt J.J.W. and van der Ven H., *Space-Time Discontinuous Galerkin Finite Element Method with Dynamic Grid Motion for Inviscid Compressible Flows: I. General Formulation,*, J. Comp. Phys. **182** (2002), 546–585.

[139] van Leer B., *Towards the ultimate conservative difference scheme V : a second-order sequel to Godunov's method*, J. Comp. Phys. **32** (1979), 361–370.

[140] van Rijn L.C., *Mathematical modeling of morphological processes in case suspended sediment transport*, Tech. Report 382, Delft Hydraulics Communication.

[141] ______, *Principles of Sediment Transport in Rivers, Estuaries and Coastal Seas*, Aqua Publications, ISBN 90-800356-2-9, 1993.

[142] Ambati V.R. and Bokhove O., *Space-time discontinuous Galerkin finite element modeling of rotating shallow water flows*, J. Comp. Phys. **225** (2007), no. 2, 1233–1261.

[143] Chow V.T., *Open channel flow*, McGraw–Hill: New York, 1959.

[144] Ottevanger W., *Discontinuous finite element modeling of river hydraulics and morphology, with application to the Paraná river*, Master's thesis, Department of Applied Mathematics, University of Twente, Enschede, The Netherlands, 2005.

[145] Wu W., Rodi W., and Wenka T., *3D numerical modeling of flow and sediment transport in open channels*, Journal of Hydraulics Engineering (2000), no. 126, 4–15.

[146] Graf W.H., *Hydraulics of Sediment Transport*, McGraw-Hill, Inc., 1971.

[147] Trush W.J., McBain S.M., and Leopold L.B., *Attributes of an alluvial river and their relation to water policy and management*, PNAS **97** (2000), no. 22, 11858–11863.

[148] Uijttewaal W.S.J. and Jirka G.H., *Grid turbulence in shallow flows*, Journal of Fluid Mechanics (2003), no. 489, 325–344.

[149] Cao Z., Day R., and Egashira S., *Coupled and decoupled numerical modelling of flow and morphological evolution in alluvial rivers*, Journal of Hydraulic Engineering **128** (2002), no. 3.

Acknowledgments

I would like to express my sincere gratitude to my promotor prof.dr. Jaap van der Vegt for giving me the opportunity to work in his group, and to my daily supervisors dr. Onno Bokhove and prof.dr. Carlos Vionnet for their assistance, motivation and encouragement in my work.

The financial support from the European Union High Level Scholarship Programme for Latin America (Programme Alβan), the Institute of Mechanics, Processes and Control Twente (IMPACT), the Federal Agency for Promoting Science and Technology (ANPCyT, Argentina), and the National Scientific and Technical Research Council of Argentina (Consejo Nacional de Investigaciones Científicas y Técnicas, CONICET) is gratefully acknowledged.

No thesis book is ever the product of one person's efforts, and certainly this one was no different. It would never have become reality without the help and suggestions of many supportive friends and colleagues. In particular, I am very grateful to Vijaya Ambati, Sander Rhebergen and Willem Ottevanger. Many important parts of this thesis are result of cooperative work, discussions and fruitful comments with them. I also would like to thanks Sander R. for the translation into Dutch of the summary of this thesis.

A special word of thanks goes to the secretaries Mariëlle Slotboom-Plekenpol and Diana Dalenoord for their assistance and contribution to the pleasant working atmosphere.

I would like also to thank to the members of the NACM group and to my former officemates and colleagues: Davit, Jaqueline, Monika, Domokos, Lie, Alyona, Remco, Bert, Henry, Bob and Ivan, as well as Enno Oosterhuis and Ewout Bakker for their computational support from NACM facilities.

Many people outside UT campus directly or indirectly contributed to the development of this work. My gratitude and thanks goes to the administrative and academic staff and researchers of the FICH-CENEHA-Universidad Nacional del Litoral (Santa Fe, Argentina), specially to prof.dr. Leticia R., Andrea G., Romina C., Leandro V., Silvina S., Aylen C., and Romina G.

I would like to express my deepest thanks to my family in Argentina: my parents José and Norma, my brother and sister Guille and Ana and the always present memory of my late grandparents. My gratitude goes also to my family in Venezuela: Santina, Antonio, Vally, Lina and Claudio for their constant support and love.

I wish to express my deep appreciation to Jessica Lammers. Through her infinite help and support, she has contributed to make this work possible. Jessica, I will always be in debt with you.

I am convinced that the person who is besides you always contributes greatly to our own creative development. I would like to dedicate this dissertation to my beloved Antonella. She has travelled a long and winding road by my side and without her love and presence, this study would not have been possible.

Summary

The morphology of alluvial river channels is a consequence of complex interaction among a number of constituent physical processes, such as flow, sediment transport and river bed deformation. This is, an alluvial river channel is formed from its own sediment.

From time to time, alluvial river channels are subject to disturbances in their immediate environment caused by natural or artificial effects, namely variable inflow, sediment supply, and various human activities such as channel regulation or reservoir construction.

Flows are primary driving forces governing the behaviour of alluvial river morphology. An increase in flow magnitude may initiate bed surface movements and bank erosion, once the force exerted by the flood event has passed some threshold for movement or erosion. The timing and frequency of flood may also have profound effects on a population; a flood can cause catastrophic damage to civil infrastructure located on or nearby the river.

The wish to improve the safety situation and to foresee the impact of the ever growing human interference with the environment, has created a need for reliable predictions of complex situations found in nature. The socio-economical and political importance of alluvial systems has also increased this need. In early time, research methodologies of river processes were primarily based on field observation and laboratory scale modelling. Laboratory scale models and field measurements have been and are still essential for the understanding of complex river processes, and are used as design and verification tools, despite their high cost of construction, maintenance and operation.

An alternative that has been growing in popularity and acceptance is river modelling. River modelling is the analysis and simulation of flow conditions based on the formulation and solution of mathematical relationships expressing hydraulic principles.

In this thesis, we focused our efforts on two main activities associated with the application of river modelling to solve particular river hydraulics problems:

(i) In Chapters 2 and 3, we perform numerical simulations based on the solution of the shallow water equations to predict flow resistance and eddy viscosity for vegetated

floodplains, and we present a numerical reconstruction of the catastrophic flooding of Santa Fe City, Argentina.

(ii) In Chapters 4 and 5, the derivation, design, and implementation of a discontinuous Galerkin method for the solution of the shallow water, sediment transport, and bed evolution equations is presented. Our numerical scheme shows ability to handle advection dominated flows, including problems with hydraulic and sediment jumps or bores. Additionally, its inherent mass and momentum conservation properties make it suitable for coupling flow and sediment transport.

We have developed a mathematical-numerical tool that enables us to reproduce, and eventually, to predict morphological changes produced in alluvial systems, in response to highly varying flow regimes.

Samenvatting

De morfologie van alluviale rivierstroombedden is een gevolg van een complexe interactie tussen een aantal natuurlijke processen zoals stroming, sediment transport en veranderingen in het rivierbed. Zodanig wordt een alluviaal rivierstroombed gevormd door zijn eigen sediment.

Regelmatig worden alluviale rivieren blootgesteld aan veranderingen in hun directe omgeving. Deze verandering kunnen veroorzaakt worden door natuurlijke of menselijke activiteiten, namelijk een variabele instroom, sediment toevoer en verscheidene menselijke ingrepen zoals stroombed regularisatie of het aanleggen van reservoirs.

Stromingen zijn primaire krachten die het gedrag van alluviale rivieren bepalen. Een toename in de grootte van de stroming kan aanzetten tot het bewegen van het stroombed en kan de oorzaak zijn van erosie aan de rivieroevers als eenmaal de door de stroming uitgeoefende kracht groter is geworden dan de drempelwaarde voor het bewegen of de erosie. Wanneer en hoe vaak een overstroming plaatsvindt kan ook grote gevolgen hebben voor de bevolking; een overstroming kan rampzalige schade veroorzaken aan de civiele infrastructuur gelegen aan of dichtbij de rivier.

De wens om de veiligheid te verbeteren en om te voorspellen wat het effect is van de groeiende invloed van de mens op zijn omgeving, heeft de behoefte aan betrouwbare voorspellingen van complexe natuurlijke situaties gecreëerd. Het sociaal-economische en politieke belang van alluviale systemen heeft deze behoefte ook vergroot. Van oudsher baseerde men het onderzoek van rivierprocessen vooral op veldobservatie of schaalmodellen in een laboratorium. Schaalmodellen en veldmetingen waren en zijn nog steeds essentieel voor het begrijpen van complexe rivierprocessen en worden gebruikt als ontwerp en verificatie hulpmiddelen ondanks de hoge kosten die deze met zich meebrengen, zoals de bouw ervan, het onderhoud en de exploitatie.

Een alternatief dat in populariteit en acceptatie toeneemt is het modelleren van rivieren. Het modelleren van rivieren is de analyse en simulatie van stromingsomstandigheden gebaseerd op het formuleren en het oplossen van wiskundige relaties die hydraulische principes beschrijven.

In dit proefschrift concentreren we ons op twee hoofdaktiviteiten die gerelateerd zijn aan het gebruik van het modelleren van rivieren om afzonderlijke rivier hydraulische problemen op te lossen:

(i) In hoofdstuk 2 en 3 hebben we een aantal numerieke simulaties uitgevoerd gebaseerd op de oplossing van de ondiep water vergelijkingen om stromingsweerstand en eddy viscositeit voor begroeide overstromingszones te voorspellen. Ook hebben we een numerieke reconstructie gemaakt van de catastrofale overstromingen in Santa Fe City, Argentinië.

(ii) In hoofdstuk 4 en 5 worden de afleiding, het ontwerp en de toepassing van een discontinue Galerkin methode voor het oplossen van de ondiep water vergelijkingen, het sediment transport en de bewegingsvergelijkingen voor de rivierbodem gepresenteerd. Onze numerieke methode toont aan dat het van toepassing is op advectie gedomineerde stromingen waaronder problemen met hydraulische en sediment “jumps”. Daar komt bij dat massa en impuls behouden blijven zodat deze geschikt is voor het koppelen van stroming en sedimenttransport.

Wij hebben een wiskundig-numeriek gereedschap ontwikkeld dat in staat kan zijn om morfologische veranderingen, die veroorzaakt woren in alluviale systemen als reactie op hoge varierende stromingsregimes, te reproduceren en uiteindelijk deze ook te voorspellen.